E.O. Paton Electric Welding Institute of the National Academy of Science of Ukraine
International Association «Welding»

The Paton Welding Journal

12
2022

International Scientific-Technical and Production Journal ◊ Founded in January 2000 (12 Issues Per Year)

Address of Editorial Board
E.O. Paton Electric Welding Institute, 11 Kazymyr Malevych Str. (former Bozhenko), 03150, Kyiv, Ukraine
Tel./Fax: (38044) 205 23 90, E-mail: journal@paton.kiev.ua
https://patonpublishinghouse.com/eng/journals/tpwj

State Registration Certificate 24933-14873 ПР from 13.08.2021
ISSN 0957-798X, DOI: http://dx.doi.org/10.37434/tpwj

Subscriptions, 12 issues per year:
$384 — annual subscription for the printed (hard copy) version, air postage and packaging included;
$312 — annual subscription for the electronic version (sending issues in pdf format or providing access to IP addresses).

Representative Office of «The Paton Welding Journal» in China:
China-Ukraine Institute of Welding, Guangdong Academy of Sciences
Address: Room 210, No. 363 Changxing Road, Tianhe, Guangzhou, 510650, China.
Zhang Yupeng, Tel: +86-20-61086791, E-mail: patonjournal@gwi.gd.cn

The content of the journal includes articles received from authors from around the world in the field of welding, metallurgy, material science and selectively includes translations into English of articles from the following journals, published by PWI in Ukrainian:
- Automatic Welding (https://patonpublishinghouse.com/eng/journals/as);
- Technical Diagnostics & Nondestructive Testing (https://patonpublishinghouse.com/eng/journals/tdnk);
- Electrometallurgy Today (https://patonpublishinghouse.com/eng/journals/sem).

CONTENTS

ORIGINAL ARTICLES

*Translated Article(s) from «Automatic Welding», No. 12, 2022.

**Translated Article(s) from «Electrometallurgy Today», No. 4, 2022.

***Translated Article(s) from «Technical Diagnostics & Nondestructive Testing», No. 4, 2022.

DOI: https://doi.org/10.37434/tpwj2022.12.01

STRENGTHENING OF WELDED STRUCTURES OF 25KhGNMT STEEL BY PULSED BARRIER DISCHARGE TREATMENT

L.M. Lobanov[1], **O.M. Berdnikova**[1], **M.O. Pashchyn**[1], **O.L. Mikhodui**[1], **O.S. Kushnaryova**[1], **T.G. Solomiychuk**[1], **V.I. Kryvyi**[2]

[1]E.O. Paton Electric Welding Institute of the NASU
11 Kazymyr Malevych Str., 03150, Kyiv, Ukraine
[2]Scientific and Production Association Praktika
15 Metalistiv Str., 03057, Kyiv, Ukraine

ABSTRACT

The development of high-tech industries stimulates the growth of requirements for the metal of welded structures and the complex of their basic and special properties. The use of pulsed electric currents, plasma currents, pulsed electromagnetic fields and their combined effects to improve the mechanical characteristics of metals and alloys is relevant in connection with the need in replacing traditional energy-intensive technologies for treatment of welded structures with more progressive ones. The use of a pulsed barrier discharge (PBD) in the metal treatment, which generates a low-temperature plasma on the surface of the treated metal is a new approach to optimizing mechanical properties of high-strength steels for welded structures, which is based on electrophysical processes. In the work, strengthening of 25KhGNMT steel as a result of PBD action on its surface was investigated. The PBD treatment of steel took place in a discharge device at an increment rate of voltage $\approx 3 \cdot 10^{11}$ V/s. The effect of PBD treatment period on Vickers hardness value (*HV*) of test specimens was investigated. Examinations of the structure of 25KhGNMT steel were carried out by the method of transmission electron microscopy to reveal its changes as a result of PBD action. It was found that values of *HV* after PBD treatment increase from 420 to 505 kg/mm^2, which is accompanied by a general increase in the dislocation density and dispersion of the microstructure, which can positively affect the mechanical characteristics of 25KhGNMT steel for welded structures operating under dynamic loads.

KEYWORDS: pulsed barrier discharge, surface treatment, low-temperature plasma, structural steel, Vickers hardness, electron microscopy, microstructure, substructure, dislocation density, strengthening, mechanical characteristics

INTRODUCTION

The development of high-tech industries stimulates an increase in requirements for steel welded structures operating in dynamic loads at high temperatures. The reserve of increasing the life of such products is the development of metal treatment technologies with the use of electrophysical effects. The use of pulsed electric currents (PEC), plasma currents, pulsed electromagnetic fields (PEMF) and their combined effects to improve the mechanical characteristics of metals, alloys and welded joints is relevant in connection with the need in replacement of traditional energy-intensive technologies of treating elements of welded structures with more progressive ones. The results of studies of electrophysical processes occurring in metal materials under the effect of PEC and EMF give reason to consider them challenging for engineering practice from the standpoint of energy efficiency and manufacturability [1–6].

The use of a pulsed barrier discharge (PBD) in the metal treatment, which generates a low-temperature plasma on the surface of the metal being treated, is a new approach to optimizing mechanical properties of metal materials for welded structures based on electric physical processes. The criterion of a rational practical use of technologies for strengthening metals and alloys using PBD is their energy efficiency *Y*, which is determined by much lower energy consumption as compared to heat treatment. The value *Y* is called energy yield and depends on such PBD parameters as voltage, its growth rate and pulse repetition frequency [7].

This is especially true for structural steels used in special purpose products operating at a short-term action of high temperatures in the conditions of dynamic loads. Special requirements are applied to the hardness of such steels, which is one of the characteristics of their protective properties at dynamic contact interactions at rates of about 1000 m/s. An example of such material is 25KhGNMT steel, which is used in critical special purpose structures. The traditional method to increase hardness of such steel is quenching, which is carried out at a temperature $T = 860$ °C in oil with the subsequent tempering at $T = 190$ °C in air [8]. This is a quite energy-consuming technology that requires large-sized metal-consuming equipment. The use of PBD to treat the surface of 25KhGNMT steel in order to improve its mechanical characteristics opens new prospects for the use of electrophysical processes in the metal treatment. Taking into account the abovementioned, it is necessary to consider it ap-

Table 1. Results of analysis of chemical composition of the test specimens of 25KhGNMT steel, wt.%

Metal	C	Si	Mn	S	P	Cr	Ni	Cu	Mo	V	Al	Ti	W
25KhGNMT steel, sheet δ = 4 mm	0.27	0.24	0.84	0.004	0.018	0.50	0.95	0.23	0.40	0.03	0.04	0.007	≤0.02

propriate to study the impact of PBD on the mechanical characteristics of 25KhGNMT steel.

The aim of this work is to study the effect of PBD on the hardness of specimens of structural 25KhGNMT steel.

TEST SPECIMENS, EQUIPMENT FOR PBD TREATMENT AND RESEARCH PROCEDURE

As a subject of investigations, plane metal specimens of 40×40×4 mm were used, which were subjected to PBD treatment. Chemical analysis of specimens was carried out in accordance with DSTU ISO 10012:2005 standard, which confirmed the correspondence of the material to be treated to the chemical composition of 25KhGNMT steel according to DSTU 7806:2015 (Table 1).

ELECTRODE SYSTEM FOR STUDYING THE EFFECT OF PBD ACTION ON THE SURFACE OF 25KhGNMT STEEL AND DISCHARGE CHARACTERISTICS

The PBD treatment of the specimen surface was carried out with the use of the electrode system (ES), whose design scheme is shown in Figure 1.

The ES consisted of the test specimen *1* of 25KhGNMT steel, the high-voltage electrode *2* and the glass (quartz glass) dielectric barrier *3* (100×100×1 mm^3). To reduce the marginal effect, the electrode *2* had rounded edges. The diameter of a plane part of this electrode was 36 mm. The treatment was carried out at a gas gap δ of 1 mm thick between the plate *1* and the barrier *3*. A high voltage (*HV*) on the electrode *2* was supplied from the pulse generator (PG), which provided unipolar pulses of voltage with an amplitude of up to 30 kV with a rate of their growth ≈ 3·10^{11} W/s and a duration of about 150 ns. PG also included a magnetic key that contributed to discharging the dielectric barrier after passing a direct current pulse through the electrode system. The pulse amplitude was regulated by changing the constant voltage U_0 supplied to the input of PG. The voltage and current oscillograms through the electrode system were registered by means of the TDS1012 oscilloscope and respectively by the sensors P6015 and P6021. All studies were performed at a pulse repetition frequency of 300 Hz. The appearance of a discharge shown in Figure 2 (exposure time is 0.1 s) indicates a homogeneous character in the gap δ rather than a thread-like one.

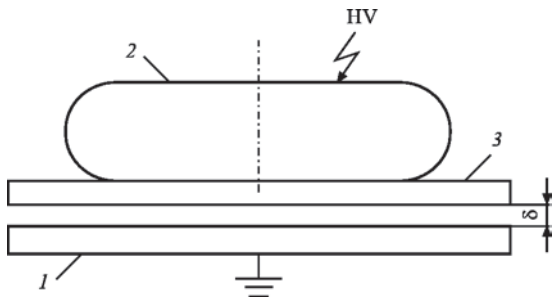

Figure 1. Scheme of electrode system (ES) for PBD treatment of 25KhGNMT steel specimens: *1* — tested specimen of 25KhGNMT steel; *2* — high-voltage electrode; *3* — dielectric barrier; δ — gas gap

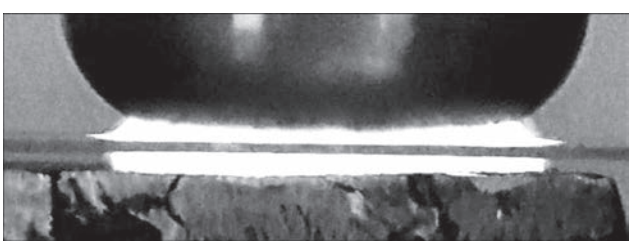

Figure 2. PBD appearance

A typical appearance of oscillograms of current $i(t)$ and voltage $u(t)$ in PBD mode, used for treatment of specimens of 25KhGNMT steel, is shown in Figure 3 respectively by the curves *1* and *2*. As is seen from Figure, during the action of the voltage pulse, whose amplitude U_m reaches 26 kV, the PBD current consists of two main parts: direct current with the amplitude I_{m1} = 80 A and reversed one with the amplitude I_{m2} = 65 A, which is predetermined by discharging a dielectric barrier through the magnetic key. The calculations show that during a direct current pulse, the amplitude value of the average current density through the plate is close to 0.9 A/cm^2.

The effect of the treatment time period on the value of hardness of steel was studied. The specimens

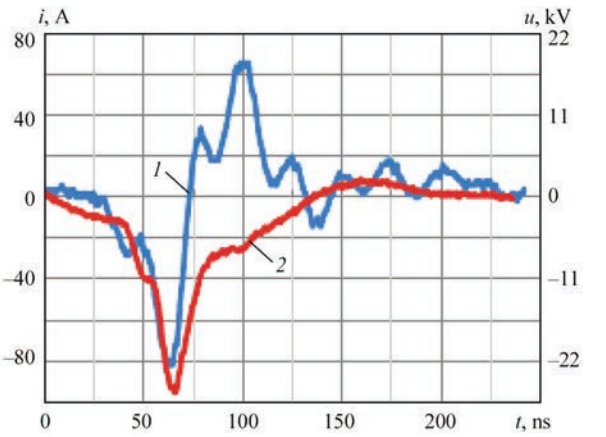

Figure 3. Typical appearance of oscillograms of current $i(t)$ — curve *1* and voltage $u(t)$ — curve *2* of PBD mode, on which the specimens of 25KhGNMT steel were treated

were subjected to PBD on the mode in Figure 3 at a variation of time of respectively 5, 10, 15 and 20 min.

Macrosections were prepared from the metal of specimens according to the standard procedure, on which structure examinations and measurements of the Vickers microhardness of treated surfaces (*HV*) according to ISO 6507-1:2005 standard were conducted. The evaluation of the *HV* values was performed with the use of M-400 LECO hardness tester at the specimen loading P = 100 g.

Transmission examinations of the structure were carried out by the method of transmission electron microscopy (TEM) in the JEM-200CX device (JEOL Company) at an accelerating voltage of 200 kV in order to find how the structure and phase composition of the metal of 25KhGNMT steel changes as a result of PBD action on its surface. The examinations by the TEM method allowed obtaining a reliable experimental information at the dislocation level about such structural and phase components as lower or upper bainite, tempered and quenching martensite, parameters of their fine structure and distribution and dislocation density in steel before and after treatment. Namely these structural components have a significant impact on the properties of strength and crack resistance of the metal of high-strength steels used in special purpose products [9, 10].

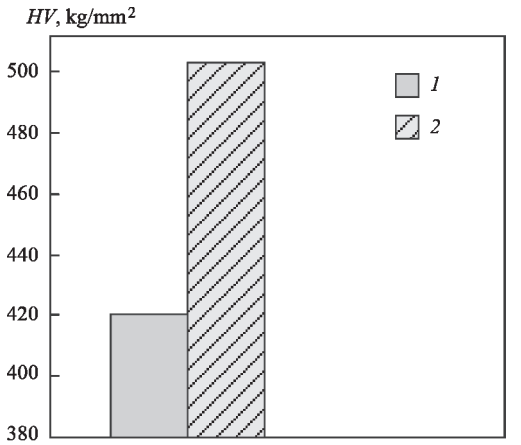

Figure 4. Hardness of 25KhGNMT steel before (*1*) and after (*2*) treatment

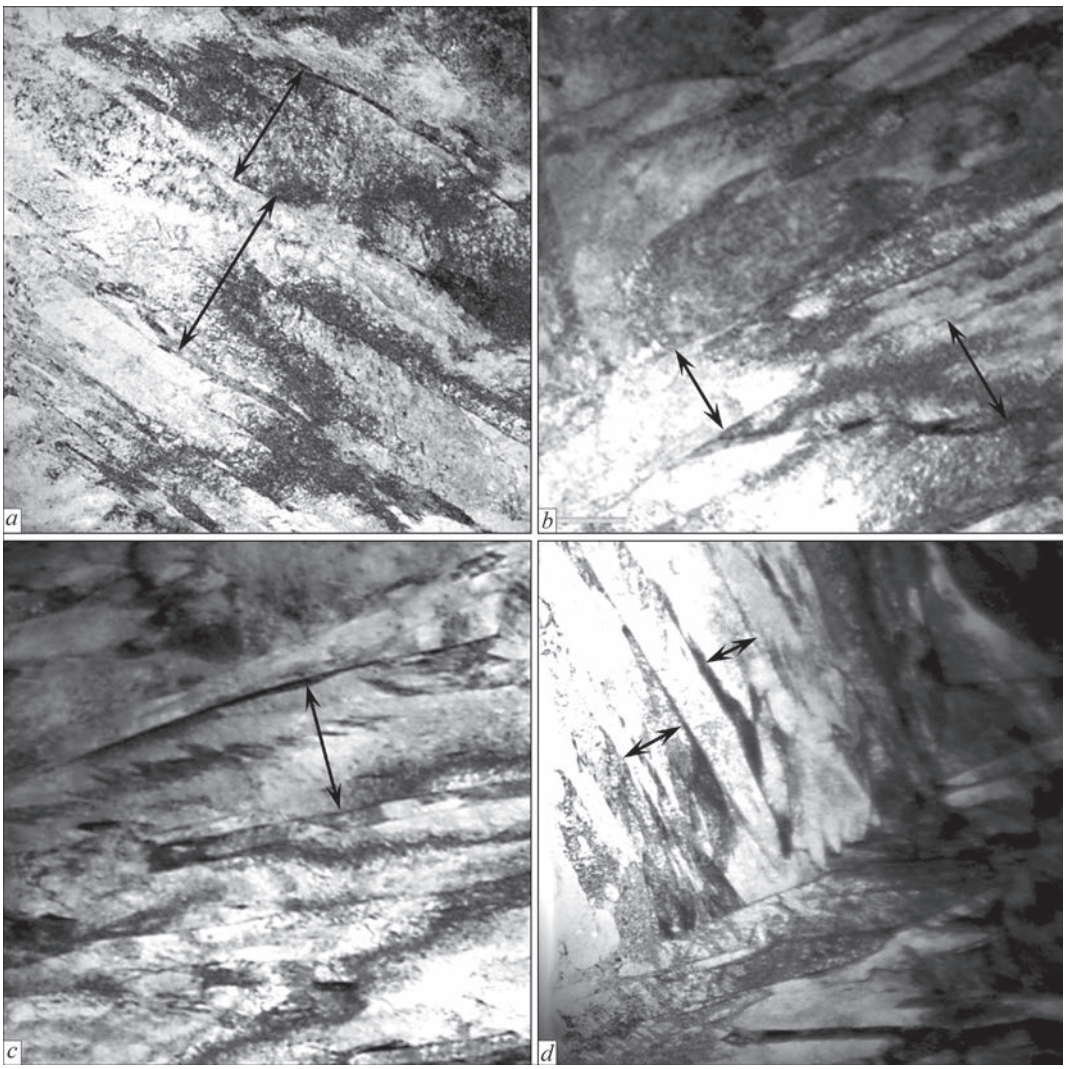

Figure 5. Fine structure of the base metal of 25KhGNMT steel: *a* — tempered martensite (M_{temp}), ×22000; *b* — lower bainite (B_l), ×22000; quenching martensite (M_{quench}), ×18000; upper bainite (B_u), ×22000). Arrows mark the width of the laths

Table 2. Dislocation density ρ in the volume of structural components of lower (B_l) and upper bainite (B_u), tempered martensite (M_{temp}) and quenching martensite (M_{quench}) over the depth from the treated surface and in the base metal (BM)

ρ, cm^{-2}	Distance from the surface, μm					BM
	0–100	150–300	300–1000	1400–1900	2000–2200	
ρ (B_l)	$(2–4)\cdot10^{10}$	$(1–3)\cdot10^{10}$	$(1–3)\cdot10^{10}$	$9\cdot10^{9}–2\cdot10^{10}$	$8\cdot10^{9}–2\cdot10^{10}$	$8\cdot10^{9}–2\cdot10^{10}$
ρ (B_u)	–	–	$(3–5)\cdot10^{10}$	$(2–4)\cdot10^{10}$	$(1–3)\cdot10^{10}$	$(1–3)\cdot10^{10}$
ρ (M_{temp})	$(5–8)\cdot10^{10}$	$(4–6)\cdot10^{10}$	$(4–6)\cdot10^{10}$	$(3–6)\cdot10^{10}$	$(2–6)\cdot10^{10}$	$(2–6)\cdot10^{10}$
ρ (M_{quench})	–	–	–	$(4–7)\cdot10^{10}$	$(4–7)\cdot10^{10}$	$(5–7)\cdot10^{10}$

RESEARCH RESULTS AND DISCUSSION

It was found that the maximum effect of PBD on hardness of 25KhGNMT steel is achieved at the duration of specimen treatment of 15 min (in this mode). At the same time, the values of *HV* after treatment increase by 20 % from 420 to 505 kg/mm^2 (Figure 4). This can contribute to an increase in dynamic strength of welded structures from the mentioned steel during their contact interactions.

As a result of the carried out transmission examinations of the structure by the TEM method, the following was revealed. The structure of the base metal of armoured 25KhGNMT steel is martensitic-bainitic, predominantly (up to 60 %) tempered martensite (M_{temp}) and lower baininite (B_l ~ 30 %) at a uniform distribution of dislocation density in the volume of structural components with a small fraction of quenching martensite (M_{quench}, to 5 %) and upper bain-

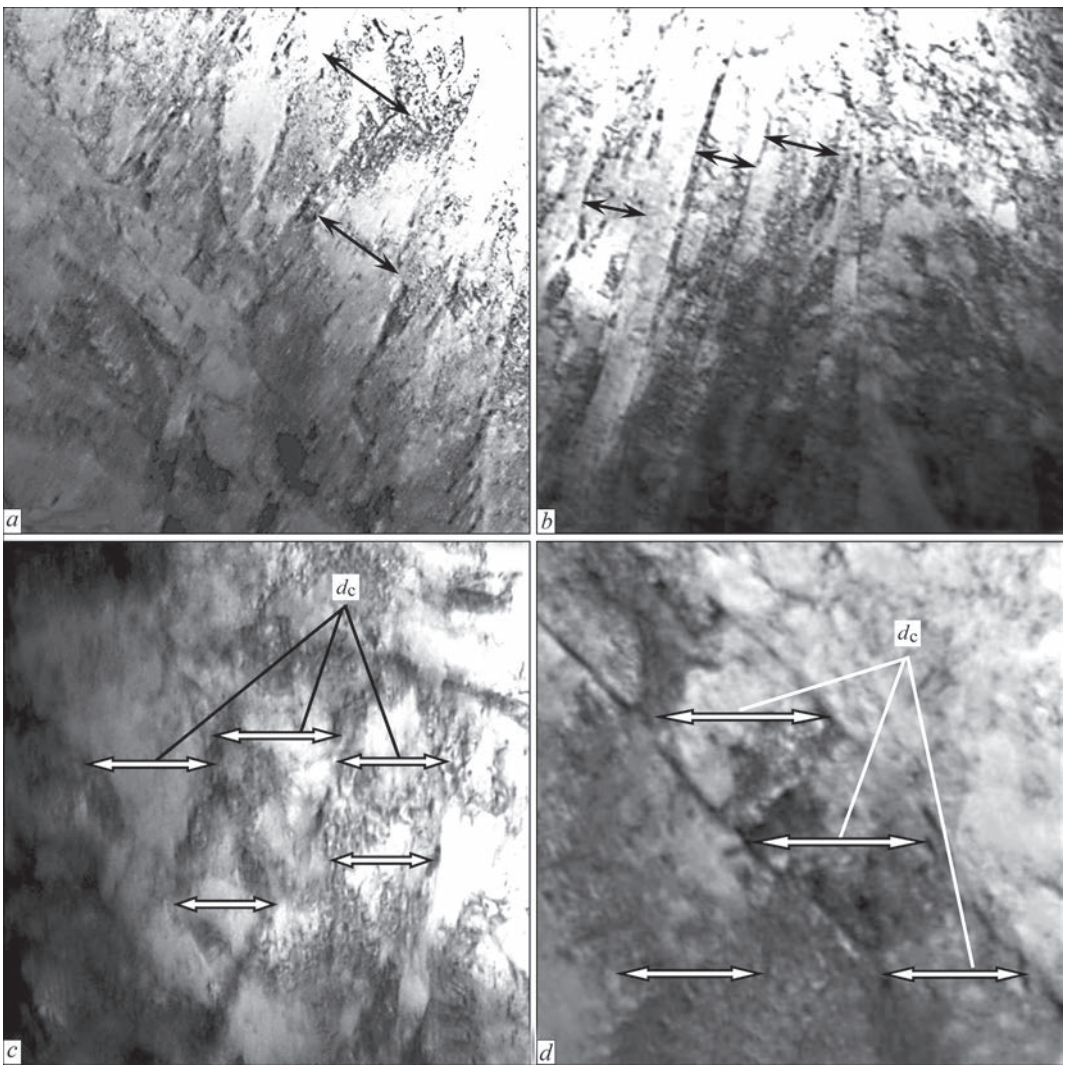

Figure 6. Fine structure of metal of the treated surface of 25KhGNMT steel: *a* — tempered martensite (M_{temp}), ×25000; *b–d* — lower bainite (B_l), respectively ×22000, ×25000, ×55000. Arrows indicate the width of the laths h_l (*a*, *b*), cellular (*c*) and fragmented substructure (d_c) (*e*)

ite (B_u ~ 5 %). The total level of dislocation density amounts to ρ = (1–6)·10^{10} cm^{-2}. When detailing the structural components of the base metal, it was found that the width of the lath structures (h_l) is: 0.3–2.0 μm (M_{temp}, Figure 5, *a*); 0.2–1.0 μm (B_l, Figure 5, *b*); 0.35–1.5 μm (M_{quench}, Figure 5, *c*); 0.3–0.8 μm (B_u, Figure 5, *d*).

Over the depth from the treated surface (from 0 to 2200 μm) in the cross-section of the specimen, a change in structural and phase composition, parameters of the fine structure and dislocation density was revealed (Table 2). Over the depth from the treated surface to 300 μm, exclusively the structure of tempered martensite and lower bainite is formed during its refinement and a uniform distribution of dislocation density (ρ = (2–8)·10 cm^{-2}) (Figure 6). As compared to the base metal, the volume fraction of lower bainite is increasing (up to 50 %). The width of the lath structures (h_l) is: 0.2–1.3 μm (M_{temp}, Figure 6, *a*); 0.15–0.65 μm (B_l, Figure 6, *b*). On the depth of 300 μm from the treated surface, a small amount of upper bainite ($B_u \leq 3$ %) is observed, and at 1400 μm, quenching martensite is fixed ($M_{quench} \leq 5$ %).

Analysis of the formed substructure showed that as a result of a pulsed effect in the area of the treated surface of 25KhGNMT steel, the inner structure of dislocation cellular structures changes with a tendency to smooth disorientations (Figure 6, *c*), which indicates a redistribution of defects in the crystalline lattice. Also, the elements of a fragmented structure of the size d_c(*h*×*1*, width×length) = 0.2–0.6×0.3–1.4 μm (M_{temp}) and 0.1–0.4×0.25–1.0 μm (B_l) appear (Figure 6, *d*).

The average values of the dislocation density in the volume and the sizes of the laths for each of the structural components in the surface layers and the base metal (BM) are shown in Figure 7.

From Figure 7, it is seen that as compared to the base metal, in the surface layers over the metal depth up to 2200 μm, a general increase (by 1.5 times, Figure 7, *a*) of the dislocation density and refinement (by 1.4 times) of the lath structures as B_l, as well as M_{temp} (Figure 7, *b*) are observed.

As a result of the examinations by the TEM method, it was found that the inner structure of the metal (as compared to BM) is characterized by a general increase in the dislocation density both in the volume as well as on the boundaries of the structural components (up to ρ = 7·10^{10}–1.2·10^{11} cm^{-2}), the formation of spectrum of dislocation substructures: cellular; cellular with a smooth disorientation and with a multidimensional discrete disorientation; with signs of fragmentation. Such structural and phase changes contribute to an increase in the overall level of surface strengthening of the metal by increasing the dislocation strengthening caused by an interdislocation interaction (according to the theories of Taylor, Zeger, Motta, etc. [11]) and a substructural strengthening due to dispersion of the structure (in accordance with the Hall–Petch dependence [12]).

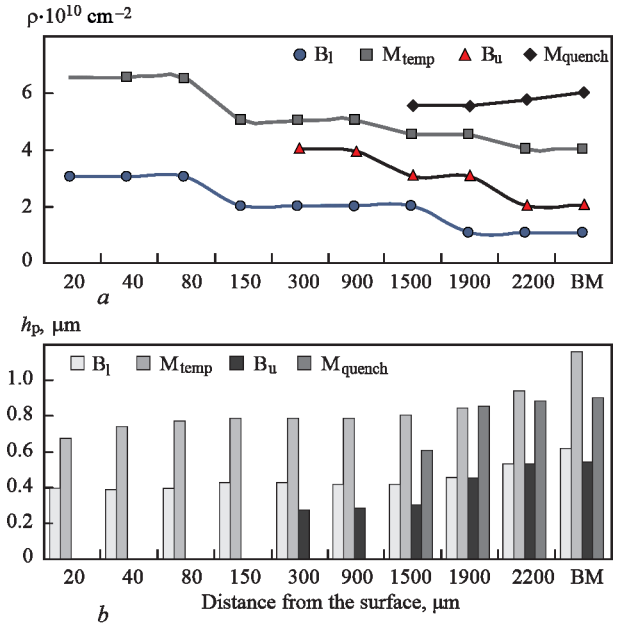

Figure 7. Changing the average parameters of the fine structure of lower bainite (B_l), tempered martensite (M_{temp}), upper bainite (B_u), quenching martensite (M_{quench}) over the depth of the treated surface and in BM: *a* — dislocation density (ρ) in the volume of structural components; *b* — width of the laths (h_l)

Thus, in the metal of the treated surface (as compared to the base metal), an overall increase in the dislocation density, as well as the structure dispersion will foster an increase in the overall level of metal strengthening. At the same time, the absence of quenching martensite and upper bainite in the surface layers of armoured steel indicates an increase in the crack resistance of metal in this area [11].

Based on the abovementioned data, the specimen of 25KhGNMT steel, whose surface was treated during 15 min, an overall strengthening of the metal due to an increase in the dislocation density and dispersion of the structure was observed as compared to the metal without treatment. As a result of PBD treatment under the action of a pulsed current in non-equilibrium conditions, it is possible to obtain a metastable state in the surface layers of the metal [13]. The action of a direct current pulse probably initiates periodic fluctuations of atoms, which results in a redistribution of defects in the crystalline lattice. The result is a deformation strengthening of the metal with a general increase in the dislocation density, refinement of the structure and the substructure formation. This will help to strengthen 25KhGNMT steel as well as to increase its crack resistance [9, 10].

Analyzing the abovementioned results, it should be noted that a local PBD treatment of 25KhGNMT

steel in the future can become the basis for developing a number of surface engineering technologies that will be aimed at extending the life of metal materials for welded structures, operating in special conditions.

CONCLUSIONS

1. It is shown that the use of a pulsed barrier discharge (PBD) for treatment of 25KhGNMT steel is the basis for developing surface engineering technologies aimed at extension of life of metal materials for welded structures operating in special conditions.

2. It was found that as a result of 15 min PBD treatment of 25KhGNMT steel, an increase in its Vickers hardness (*HV*) by 20 % to a depth of 2 mm occurs, which is predetermined by the refinement of a martensite-bainite structure at an increase in the fraction of lower bainite and the formation of dislocation substructures with the features of fragmentation that promotes an increase in the overall level of surface strengthening of the metal by increasing dislocation and substructure strengthening.

3. The mechanism of strengthening steel as a result of PBD treatment, which is based on obtaining the metastable state in the surface layers of the metal in the non-equilibrium conditions is proposed. The action of a direct current pulse initiates periodic fluctuations of atoms, which results in a redistribution of defects in the crystalline lattice. The result is deformation strengthening of the metal and refinement of the lath structure of martensite.

REFERENCES

1. Dubodelov, V.I., Goryuk, M.S. (2018) *Application of electromagnetic fields and magnetohydrodynamic phenomena for intensification of effect on metallic systems: World and Ukrainian experience*. In: Science of Materials. Achivements and Prospects. In: 2 Vol., Vol. 2, 24–50, Kyiv, Akademperiodyka [in Ukrainian].
2. Sydorenko, Y.M., Pashchin M.O., Mykhodui, O.L. et al. (2020) Effect of pulse current on residual stresses in AMg6 aluminum alloy in electrodynamic treatment. *Strength of Materials*, 52(**5**), 731–737. DOI: https://doi.org/10.1007/s11223–020–00226–2
3. Lobanov, L.M., Pashchyn, M.O., Mikhodui, O.L. et al. (2021) Modeling of stress–strain states of AMg6 alloy due to impact action of electrode-indenter in electrodynamic treatment. *The Paton Welding J.*, **6**, 2–11. DOI: https://doi.org/10.37434/tpwj2021.06.01
4. Zhang, Jun, Liu, Ji-De, Zhang, Xin-Fang et al. (2021) Effect of high density current pulses on microstructure and mechanical properties of dual-phase wrought superalloy. *Acta Metallurgica Sinica*, 34(**12**), 1635–1644. DOI: https://doi.org/10.1007/s40195–021–01211–7
5. Diao, Aimin, Wang, Jingpen, Yang, Yuqiu et al. (2022) Fatigue damage recovery of 20 carbon steel under pulsed current. *Tezhong Zhuzao Ji Youse Hejin/Special Casting and Nonferrous Alloys*, 42(**3**), 318–322. DOI: https://doi.org/10.15980/j.tzzz.2022.03.009
6. Guo, J.D., Wang, X.L., Dai, W.B. (2015) Microstructure evolution in metals induced by high density electric current pulses. *Materials Sci. and Technology (United Kingdom)*, 31(**13a**), 1545–1554. http://www.maneyonline.com/doi/pdfplus/10.1179/1743284715Y.0000000001doi: 10.1179/1743284715Y.0000000001
7. *Fangmin* Huang, Li Chen, HonglinWang, Zongcheng Yan. (2010) Analysis of the degradation mechanism of methylene blue by atmospheric pressure dielectric barrier discharge plasma. *Chemical Eng. J.*, **162**, 250–256.
8. https://s-metall.com.ua
9. Kostin, V.A., Poznyakov, V.D., Berdnikova, O.M. et al. (2021) Influence of structural transformations on the mechanical properties of welded joints of armor steels. *Materials Sci.*, 56(**4**), 472–480. https://doi.org/10.1007/s11003–021–00453–1
10. Berdnikova, O.M., Kostin, V.A., Poznyakov, V.D. et al. (2020) Structure and crack resistance of special steels with 0.25–0.31 % carbon under the conditions of simulation of thermal cycles of welding. *The Paton Welding J.*, **5**, 2–8. DOI: https://doi.org/10.37434/tpwj2020.05.01
11. Goldshtejn, M.I., Litvinov, V.S., Bronfin, B. M. (1986) *Physics of metals of high-strength alloys*. Moscow, Metallurgiya [in Russian].
12. Farber, V.M., Belenkij, B.Z., Goldshtejn, M.I. (1975) Evaluation of strength of low-carbon low-alloy steels by structural data. *Fizika Metallov i Metallovedenie*, 3(**2**), 403–409 [in Russian].
13. Gridnev, V.N., Trefilov, V.I. (1988) *Phase and structural transformations and metastable states in metals*. Kyiv, Naukova Dumka [in Russian].

ORCID

L.M. Lobanov: 0000-0001-9296-2335,
O.M. Berdnikova: 0000-0001-9754-9478,
M.O. Pashchyn: 0000-0002-2201-5137,
O.L. Mikhodui: 0000-0001-6660-7540,
O.S. Kushnaryova: 0000-0002-2125-1795,
V.I. Kryvyi: 0000-0003-2611-528X

CONFLICT OF INTEREST

The Authors declare no conflict of interest

CORRESPONDING AUTHOR

M.O. Pashchyn
E.O. Paton Electric Welding Institute of the NASU
11 Kazymyr Malevych Str., 03150, Kyiv, Ukraine.
E-mail: svarka2000@ukr.net

SUGGESTED CITATION

L.M. Lobanov, O.M. Berdnikova, M.O. Pashchyn, O.L. Mikhodui, O.S. Kushnaryova, T.G. Solomiychuk, V.I. Kryvyi (2022) Strengthening of welded structures of 25KhGNMT steel by pulsed barrier discharge treatment. *The Paton Welding J.*, **12**, 3–8.

JOURNAL HOME PAGE

https://patonpublishinghouse.com/eng/journals/tpwj

Received: 02.08.2022
Accepted: 30.01.2023

DOI: https://doi.org/10.37434/tpwj2022.12.02

FEATURES OF WELDING HIGH-STRENGTH ALLOYS BASED ON ALUMINIUM AND BERYLLIUM USING HIGHLY-CONCENTRATED HEAT SOURCES (REVIEW)

S.I. Peleshenko[3], V.Yu. Khaskin[1,2], V.M. Korzhyk[1,2], V.V. Kvasnytskyi[2,3], A.A. Grynyuk[2,3], I.M. Klochkov[2], D. Chunling[1], A.O. Alyoshin[1,2]

[1]China-Ukraine Institute of Welding, Guangdong Academy of Sciences,
Guangdong Provincial Key Laboratory of Advanced Welding Technology
510650, Guangzhou, China
[2]E.O. Paton Electric Welding Institute of the NAS of Ukraine
11 Kazymyr Malevych Str., 03150, Kyiv, Ukraine
[3]NTUU «Igor Sikorskyi Kyiv Polytechnic Institute»
37 Peremohy Prosp., 03056, Kyiv

ABSTRACT

Results of welding a wide range of light alloys by highly-concentrated heat sources have been analyzed. It is shown that the characteristic defects are hot cracks, internal pores, HAZ softening, weld sagging, undercuts and irregular reinforcement bead formation. It was found that in order to produce sound joints, it is necessary to thoroughly select welding mode parameters, remove the oxide film from blank edges before welding, ensure reliable protection of the weld pool, and in some cases and it is rational to apply preheating or concurrent heating. One of the advanced methods to minimize the susceptibility to formation of the above-mentioned defects is application of hybrid laser-arc and laser-plasma welding processes. The welds produced by electron beam and laser (CO_2- and fiber-optic lasers) welding processes are quite similar visually, by their macrostructure, as well as the main characteristics. The weld strength parameters and heat input required for full penetration of the metal are somewhat different for different welding methods (for fiberoptic laser it is usually 30 % less).

KEYWORDS: welding, laser, electron beam, laser-arc, laser-plasma, light alloys, aluminium, beryllium, defects, mode parameters, mechanical properties

INTRODUCTION

Aluminium, magnesium, beryllium as well as their alloys are widely used in modern equipment manufacture in particular in aircraft and rocket construction that is caused by unique combination of the next properties, namely low density at high values of specific strength, corrosion resistance and thermal conductivity. Variety of structures from these materials as well as tendency of welded joints to defect formation requires searching the new methods of welding of indicated alloys. High thermal conductivity complicates development of classical arc welding technologies of these alloys. One of the radical methods of decrease of thermal conductivity effect on residual stress-strain state of welded structures is application of highly-concentrated heat sources, in particular, laser, laser-arc, laser-plasma and electron beam. Welding with such highly-concentrated heat sources allows reaching high indices of efficiency, quality of produced joints, has high stability and good repeatability of results. Nevertheless, the literature has got the information about effect of parameters of modes and conditions of welding process on formation of welded joints, their tendency to defect formation doesn't always match, therefore investigations of peculiarities of production of joints of light alloys based on aluminium and beryllium using highly-concentrated energy sources is relevant.

PROBLEM STATEMENT

One of the main problems of laser welding of light alloys is high reflectivity of the material being joined or its low absorption coefficient of laser radiation, which makes up to 10 % for wave length 1.06 μm [1]. This promotes decrease of efficiency of the process of laser welding. Moreover, the processes of welding using highly-concentrated heat sources are complicated due to high values of thermal conductivity of these alloys: 236 W/(m·K) for aluminium and 201 W/(m·K) for beryllium under normal conditions [2]. One more problem is a presence of thermodynamically stable oxide film (Al_2O_3 or BeO) on welded surfaces, coming of which into a cast weld metal results in its mechanical weakening [3]. On their own light alloys are very sensitive to effect of environment, susceptible to formation in welds of oxide inclusions and pores at interaction with air atmosphere [4].

Metallurgical processes of welding using highly-concentrated energy sources of light alloys differ with presence of keyhole, intensity of evaporation of alloying elements as well as peculiarities of solidification under conditions of effect of welding thermal cycle. Laser and hybrid processes additionally require

consideration of base metal interaction with environment gases. Practical realization of the processes of welding of light alloys using highly-concentrated heat sources is related with a series of peculiarities that reflect on technology, selection of method and modes as well as properties of produced welded joints.

An aim of this work is review of the modern achievements in the field of welding with highly-concentrated heat sources of light alloys based on aluminium and beryllium, which are used in aircraft, rocket and space engineering, determination of the main peculiarities of welding processes and ways of removal of the typical disadvantages.

In order to reach the aim we have analyzed the peculiarities of the processes of welding using highly-concentrated heat sources of light alloys based on aluminium and beryllium; outlined the main general peculiarities of welding and physical modeling of a process of welding using highly-concentrated heat sources of light alloys that are characterized with unsatisfactory technological ability to welding.

ANALYSIS OF PECULIARITIES OF WELDING USING HIGHLY-CONCENTRATED HEAT SOURCES OF LIGHT ALLOYS BASED ON ALUMINIUM AND BERYLLIUM

Due to high mechanical properties an issue of welding of high-strength aluminium alloys of Al–Mg–Si (series 6xxx) [5], Al–Zn–Mg–Cu (series 7xxx) as well as aluminium alloys doped with lithium (Al–Mg–Li system) and scandium (Al–Cu–Li–Sc) [7] is of high interest in modern industry. First of all, three component Lockalloys of Al–Be–Mg system of Lx-59-3 grades (59Be, 3Mg), Lx-40-3 (40Be, 3Mg) [8] are referred to widely used high-strength beryllium alloys. The main mechanical properties of the most widespread light alloys are given in Table 1. It is noted that welding of such alloys is complicated due to their susceptibility to formation of hot cracks and pores.

In contrast to electron beam welding [9] development of welding technology with laser radiation requires thorough weld shielding from environment [10]. In case of welding of light alloys such gases as helium, argon as well as their mixtures are used. From point of view of shieldinging the gases with high ionizing potential are relevant for usage in a zone of action of laser radiation. The following scheme of gas shielding of weld in laser welding is recommended [11]: shielding of weld pool and weld surface by helium with 8–10 l/min consumption and weld root by argon with 5–8 l/min consumption. A peculiarity of such gas shielding is abrupt increase of penetration depth after overcoming primary boundary values of radiation energy. At hybrid consumable electrode laser-arc welding for minimizing pore formation and increase of penetration depth it is recommended to add 50 % of helium to argon shieldinging gas [12].

In addition to gas shielding, for laser [13] and laser-arc [14] welding it is possible to use a flux protection of a surface and weld root. Before welding the surface of joint and its root part is covered with specially developed fluxes. Application of flux protection allows reducing the requirements to preliminary joint assembly increasing the possible gap between welding edges by 2–3 times [15]. The fluxes may contain graphite, metal powders, fluorides of alkali and alkaline earth metals. Such materials promote increase of an absorption coefficient of laser radiation, improve surface activity of melt, provide high coefficient of surface tension of flux melt. Application of fluxes for laser and hybrid welding of light alloys results in redistribution of energy balance that is related with increase of absorption of radiation energy and removal of oxide film. At that efficiency of the process rises, limit of critical density of power typical for laser welding of light alloys is reduced.

Flux protection in contrast to gas one provides smooth increase of penetration depth at rise of energy input.

As a rule, weldability of light alloys with highly-concentrated heat sources is similar to their weldability using traditional arc sources. Table 2 gives the data on aluminium alloy weldability.

One of the most important aspects of the specifics of aluminium and beryllium alloy welding is the difference in melting temperatures and absorption coefficients of the metals proper and their oxide films. Aluminium and beryllium are susceptible to intensive oxidation at temperatures exceeding melting temperature. Oxide film has high melting temperature (> 2000–2500 °C) and does not melt in the process of welding, however can partially burn out due to intensive absorption of laser radiation. This film is characterized with high adsorption capacity

Table 1. Main physicomechanical characteristics of some aluminium and beryllium–aluminium alloys (at normal temperature) [5, 6, 8]

Alloy grade	Yield limit, MPa	Strength limit, MPa	Relative elongation, %	Young modulus, GPa	Density, kg/m^3	Hardness *HB*, MPa
5083	130–160	200–280	15	69	2720	70
6061	145–276	240–310	9–14	69–70	2700	65–95
7005	245–290	355–400	8–12	72	2770	90–95
7075	450–500	510–570	3–11	71,7	2810	150–160
Lx-59-3	280–480	220–490	1–9	175–200	2100	250
Lx-40-3	350–490	250–530	1–9	180–200	2100	250

Table 2. Weldability of aluminium alloys [16]

Alloy series	Application	Weldability	Exceptions	Filler alloy
1xxx	Commercially pure aluminium (A1 > 99 %). Electric current conductors, products with high corrosion resistance etc.	Easy to weld	No	Mostly 1100
2xxx	High-strength aerospace aluminium alloys (“durals”) are mostly used in form of plates and sheets	Mostly not weldable due to high tendency to hot cracking	Alloys 2219 and 2519 are welded	2319 or 4043
3xxx	Medium strength aluminium alloys can be easily subjected to forming. Used for heat exchangers and air conditioning	Easy to weld	No	4043 or 5356
4xxx	Used for structures and as alloys for welding and brazing	–»–	–»–	4043
5xxx	Mainly for high-strength sheets and plates	–»–	5183 or 5556 are used for welding of 5083	5356
6xxx	For pressed profiles, sheets and plates etc.	Good weldability at corresponding technology	Susceptible to hot cracking	4034, 5356
7xxx	High-strength aerospace alloys	Mostly unweldable due to tendency to hot cracking and corrosion under mechanical stress effect	Welded are alloys 7003 and 7005 for pressed profiles and alloy 7039 for sheets	5356

to gases and water vapor that results in appearance gases, pores and various inhomogeneities in the weld pool [3]. The film particles can enter into the weld pool forming oxide inclusions in the welds that decreases mechanical properties of the welded joints. Therefore, special methods are used in laser and hybrid welding. They promote destruction and removal of the oxide film and metal protection from reoxidation — from preliminary mechanical removal to laser burning [17].

The main difference of laser welding of light alloys is a threshold nature of penetration which starts only after reaching a specific level of power density (about 10^6 W/cm^2) [15]. It is explained by combination of the coefficients of reflection, thermal conductivity and heat capacity of aluminium and beryllium alloys. At introduction of sufficient amount of energy after the start of melting process the coefficient of reflection rapidly decreases and intensive penetration of metal with formation of a keyhole takes place. Power density threshold depends on radiation wave length, focusing parameters, welding rate, thickness and condition of plate surface as well as material composition. It can be significantly reduced at hybrid welding as a result of effect of arc or plasma constituent of the process [18].

Presence of threshold level of laser radiation power, which provides penetration in welding, makes accurate selection of mode parameters very relevant. Thus, authors of work [15] determined that for alloy 1560 (analog 5083) power of CO_2 laser at 2.0–2.2 kW level provides penetration depth about 1.5–2.0 mm. Penetration radiation is virtually absent at lower power due to the reason of high reflection coefficient mentioned above. Further increase of radiation power results in virtually linear increase of penetration depth.

Today fiber lasers [19] are recognized as the most perspective ones. Nevertheless, their application can result in such problems of weld root formation quality as nonstable penetration, melt splashing and nonuniformity [20]. This is related with the rise of pressure on pool bottom (keyhole effect) when using fiber laser instead of CO_2 laser. Therefore, it is necessary to carry out the investigations on welding of light alloys with fiber laser.

For investigations on welding with fiber laser in work [15] there was used a complex based on fiber ytterbium laser of IPE-Polyus Company LZ-3.5 of 3.5 kW power. The investigations showed that the level of power density, necessary for start of penetration when using fiber laser is approximately 2 times lower than for CO_2 laser (Figure 1). It can be seen from Table 3, which provides the modes of welding of aluminium alloy 01570 (AlMg6Mn0.5Sc3) of Al–Mg–Sc system with fiber and CO_2 lasers, that power of laser radiation necessary for 2.0 mm thick sheet welding using fiber laser is 30 % lower than in welding with CO_2 laser. It should be noted that similar alloy is sufficiently well welded using electron beam method [21].

The structures of welded aluminium alloys, produced by laser and electron beam methods, are close enough [22]. The same relates to the joints produced with CO_2 and fiber laser radiation. Small weld width and volume

Table 3. Relationship of rate of butt welding modes of plates from alloy 01570 of 2 mm thickness using various type lasers [15]

Welding rate, m/min	Laser radiation power, kW	
	CO_2- laser	Fiber laser
2.0	1.6	1.1
3.0	2.6	1.4
4.0	4.0	1.9

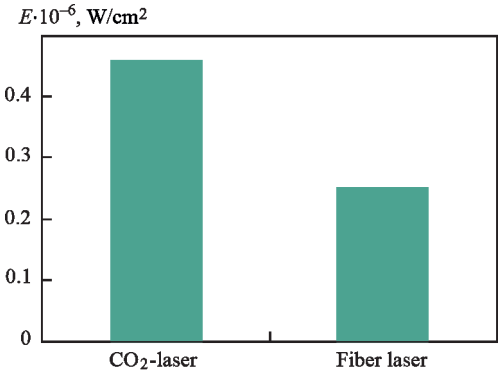

Figure 1. Dependence of threshold density of penetration power of alloy 01570 on type of laser radiation source [15]

of weld pool were observed in most of the cases of examined welded joints of aluminium alloys. Penetration with virtually parallel edges, weld shape coefficient $K < 1$ is achieved in welding of relatively thin materials (Figure 2, *a*) [23] or at certain increase of energy input (Figure 2, *b*) [24]. At that concavity and sagging of the weld are in allowable measures. Weld sagging (Figure 2, *c*) [25] can appear in case of welding with insufficient rate. In order to remove this defect it is relevant to use filler (and in case of hybrid welding — electrode) wire. In comparison with traditional consumable electrode welding (MIG, GMAW) the volume of molten metal in laser or electron beam welding is 2–3 time smaller (Figure 2, *d*) [26]. Close results are observed in comparison of highly-concentrated methods of welding with non-consumable electrode welding (TIG) [15, 20].

However, it is not always possible to get the certain weld shape by means of correction of welding mode. Thus, in welding of such high-strength alloys as 7075 to minimize such typical defects as pores and

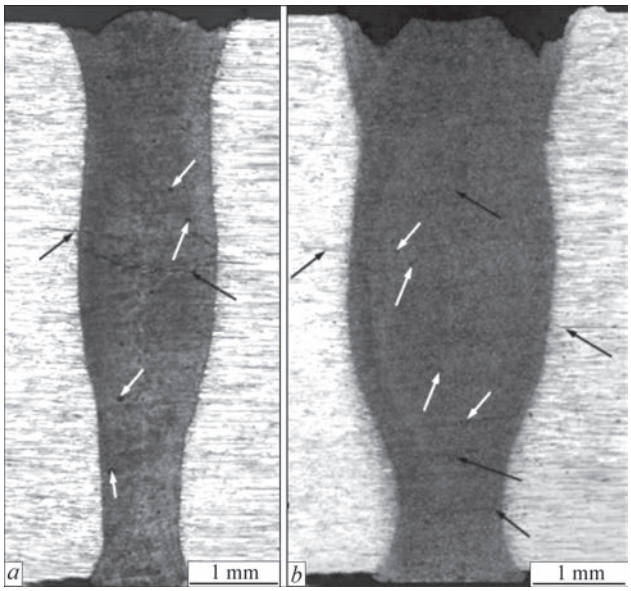

Figure 3. Microstructures of cross-sections of 7075 alloy joints (thickness 6.0 mm) produced by laser welding at different values of heat input [27]: *a* — 90; *b* — 180 kJ/m; black arrows indicate microcracks, white ones — microporosity

cracks it is relevant to reduce heat input (Figure 3) [27]. Concurrent local heating with simultaneous introduction of filler material, i.e. hybrid laser-arc process (Figure 4) [28], can be used in order to remove the defects mentioned above. Dosing of electric arc energy in hybrid process provides 30–60 % decrease of a volume of molten metal [29]. Thus, high-strength alloys (Figure 5) [30] are also used in welding of automobile structures (so called TWB — tailored welded blanks). Heat treatment is used after welding (annealing at temperatures about 450 °C) to get the possibility of their mechanical deformation (stamping).

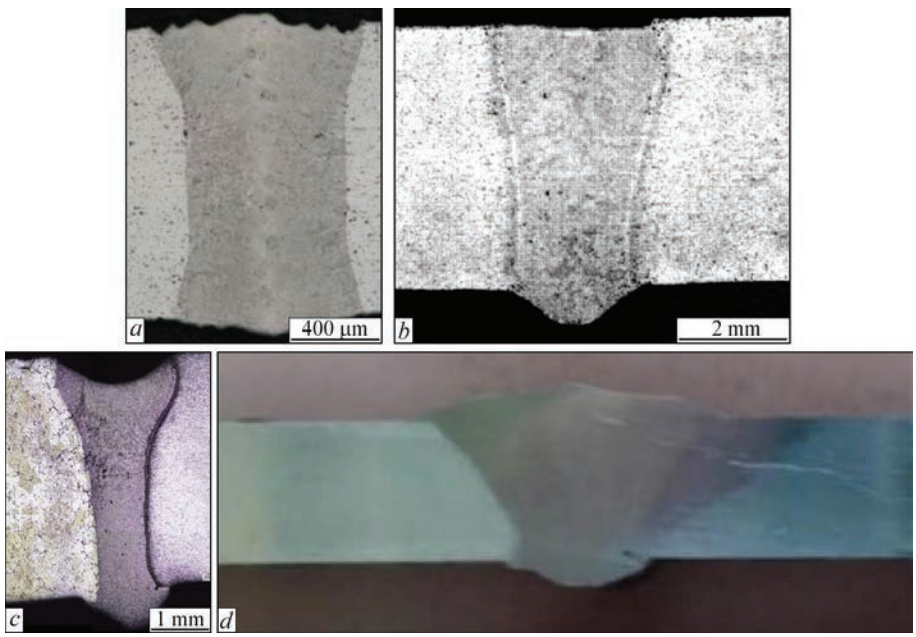

Figure 2. Results of welding of aluminium alloys using different methods: *a* — laser (alloy 6013, thickness 1.25 mm) [23]; *b* — electron beam (alloy 6061, thickness 5.0 mm) [24]; *c* — electron beam (alloys 2219 and 5083, thickness 5.0 mm) [25]; *d* — consumable electrode (alloy 6013, thickness 5.0 mm) [26]

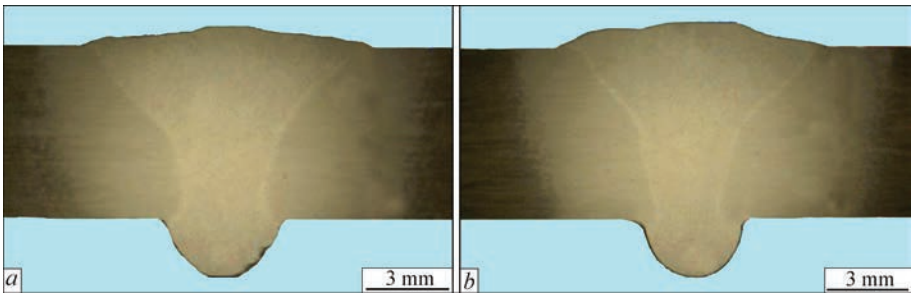

Figure 4. Microstructures of cross-sections of joints [28] produced by hybrid laser-arc welding of alloy 6082 (thickness 6.0 mm) using pulsed-arc consumable electrode welding (*a*) and CMT (cold metal transfer) process (*b*)

Laser welding with filler wire [31] or hydrid laser-arc welding [32] are relevant to use in order to remove weld concavity and achievement of stable formation of upper reinforcement bead. This allows reducing the requirement to butt joint assembly and obtaining the quality welded joints at gaps between the blank edges in 0.1–1.0 mm range. Diameter and rate of wire feed are selected based on thickness of material being welded and welding rate. Usually diameter of wire in laser welding makes 0.6–1.2 and in hybrid 0.8–1.6 mm. The optimum wire feed angle lies in 15–30° range from the joint area. The wire can be fed in front of the source of laser radiation or behind it during welding that can influence the efficiency and stability of the process.

One of the typical defects of welding of light alloys using highly-concentrated energy sources is a tendency to pore formation due to instability of penetration (pulsation due to keyhole effect) [20] as well as under effect of hydrogen, which is well solved in aluminium and beryllium at melting temperature [33, 34]. Increased susceptibility to porosity is typical for welding of aluminium–magnesium alloys, since magnesium rises hydrogen solubility in aluminium [35]. Treatment of surface before welding is used for porosity reduction for the purpose of removal of moisture absorbed by metal surface and oxide film, which contains hydrated oxides. The most effective for this is application of mechanical or chemical (etching) removal of the oxide film on 25–30 mm width from blank edges along the whole length of the joint [36].

Another typical defect of welding of light alloys using highly-concentrated energy sources is a susceptibility to hot cracking. The cracks can even be formed when using pulsed welding processes, which in comparison with continuous processes allow decreasing energy input in the material being welded. The most effective method for removal of this defect is weld alloying by means of introduction of filler material of corresponding composition. Thus, pulsed laser welding of heat treated aluminium alloy Al–4.7Mg–0.32Mn–0.21Sc–0.1Zr without filler metal and with filler metal of Al–5Mg alloy provoked formation of duplex (columnar and fine-grain) cast structures and gas porosity in form of defects in weld zone [37].

Application for welding of Al–5Ti–1B type filler metal provided formation of the fine-grain structure with an average grain size 4 ± 0.2 μm without weld defects. The average concentration of alloying elements in the weld made 2.8Mg0.2Mn0.1Zr0, 15Sc2.1Ti. Tensile strength of the weld made 260 MPa that corresponded to the values typical for the base metal in cast state. After annealing at 370 °C during 6 h this index rises by 60 MPa that made 85 % of base metal strength in as-rolled condition.

In addition to defects mentioned above, it is necessary to note the toxicity of welding aerosols being emitted [38]. Since beryllium content in the air should not exceed 0.001–0.003 mg/m^3, therefore it welding is usually carried out in closed chambers with controlled atmosphere that is provided by suction and filtering of formed harmful chemical compounds.

Investigations of weldability of beryllium and its alloys show that cast alloys on its base can be successfully welded using TIG, electron beam and laser methods [39]. Nevertheless, today for manufacture of critical structures of beryllium alloys the advantage is given to vacuum technologies such as electron beam welding and vacuum brazing [40].

The main obstacles for welding of beryllium are hot cracking, formation of cracks due to weld defects and low ductility [40]. Hot cracking can be reduced by means of control of chemical composition of beryllium being welded. Work [39] proposes to control Fe:Al relationship in such a way as it reaches less than 2.4 at his con-

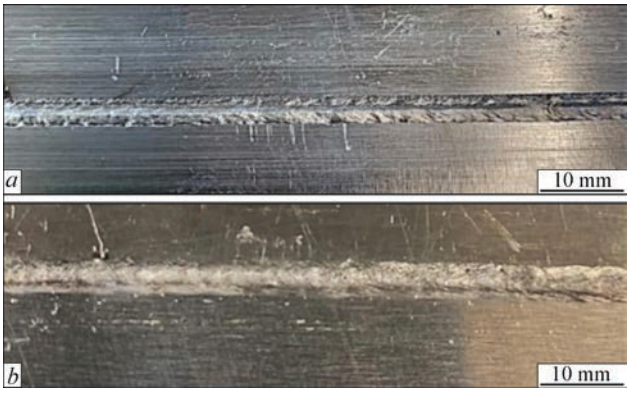

Figure 5. Appearance of welded joints of alloys 5251 with 6082 [30] (thickness 1.5 mm) in the TWB (tailored welded blanks) products produced by electron beam (*a*) and laser (*b*) methods

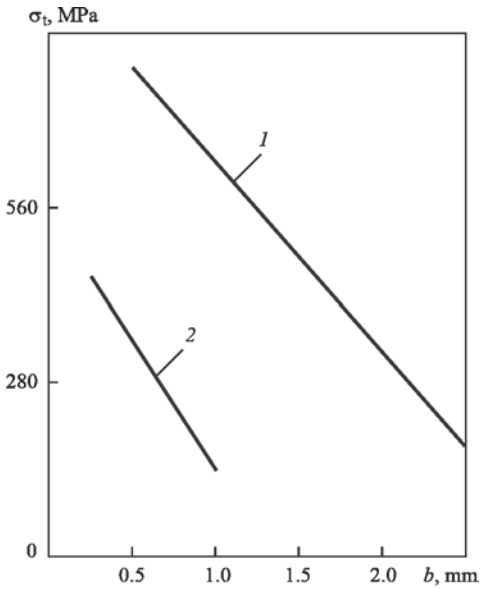

Figure 6. Dependence of ultimate strength σ_t of beryllium and its welds on grain size b [41]: *1* — base metal; *2* — weld metal

tent of iron and aluminium shall be minimum. Cracking related with the presence of defects and limited metal ductility can be reduced by decrease of BeO oxide and grain size of initial material. In addition, weldability of beryllium can also be improved due to decrease of welding rate, moderate heat input, minimizing fixing load of parts being welded as well as using corresponding pre- or concurrent heating. In some cases crack formation in the welds can be successfully removed by means of introduction of aluminium alloy filler into the weld pool. In this case it is necessary to take into account that usage of filler metal can reduce the operating temperature and yield limit of the welded joint.

Technological investigations of the peculiarities of the processes of beryllium welding using highly-concentrated energy sources showed its susceptibility to hot crack formation. The most effective way of their removal is decrease of temperature of local overheating of welded sample that is reached by reduction of the welding heat input, for example, as a result of increase of radiation power density through focusing using short-focus optics with simultaneous rise of welding process rate. Beryllium welding also leads to such defects as splashing of metal and irregularity of weld formation. They can be removed at proper selection of the welding modes, in particular the welding rate.

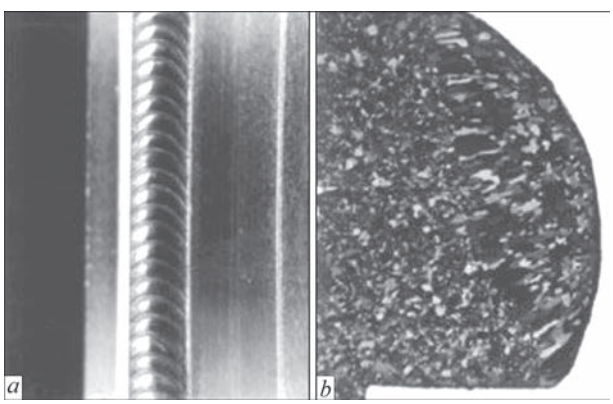

Figure 7. Laser welding of commercial structural beryllium [42]: *a* — appearance of weld of 25.4 mm diameter (ripple is formed by pulsed welding with points overlap); *b* — structure of cross-section of fusion zone, ×100

Application of special alloyed filler materials with aluminium in welding of beryllium and its alloy allows rising the joint strength from 0.5–0.6 to 0.7–0.8 of the base metal strength at simultaneous rise of ductility. Introduction into the weld of additional alloying elements permits rising strength with the help of post weld heat treatment, however themselves the alloys of Al–Be–Mg system are not heat treated. Such heat treatment provides production of full-strength welds compared to base metal [41].

Strength of the welds in welding of beryllium alloys significantly depends on size of crystallites of the weld metal (Figure 6). Refinement of weld structure is one of the way of production of the welded joints that on strength approach to the base metal: at 3–4 times (from 1.0 to 0.25 mm) decrease of the crystallite size the weld metal yield strength rises 3 times (from 137 to 412 MPa) [41].

In manufacture of the special beryllium parts for space satellites, for example, cylinder bodies of the power elements working at more than 600 °C temperature it is not permitted that foreign chemical elements come into the welded joints, therefore it is not allowed to use welding filler materials or replace welding by brazing [42]. Pulsed laser welding was used in this case. For welding of the body of energy source element its cylindrical part with a lid of 25.4 mm diameter being welded with girth weld was placed in a air-tight chamber with inert gas under required pressure and Nd:YAG-laser beam was passed through a transparent glass of this chamber. Cracking was eliminated using the pulsed radiation mode for welding (Figure 7).

An issue of laser welding of beryllium and its alloys in a controlled atmosphere as well as laser and electron beam welding in vacuum was studied in different works [43–45]. For example, work [45] describes the electron beam welding of beryllium alloys: A — 99.58 % Be + admixtures; B — 99.63 % Be + admixtures; C — 99.87 % Be + admixtures. The susceptibility of welded joints to formation of hot cracks across the weld was noted. At that, the direction of dendrite growth in solidification of weld pool metal resulted in weakening of longitudinal axial area of the weld (Figure 8).

The investigations of the values of residual stresses in Be–AlSi welded parts showed that welds strength to a significant extent depend on geometry of the structure, penetration depth and presence of defects, but much less on a level of residual stresses [46]. For analysis of the stressed state of cylinder shells from beryllium in work [47] there was carried out a modeling

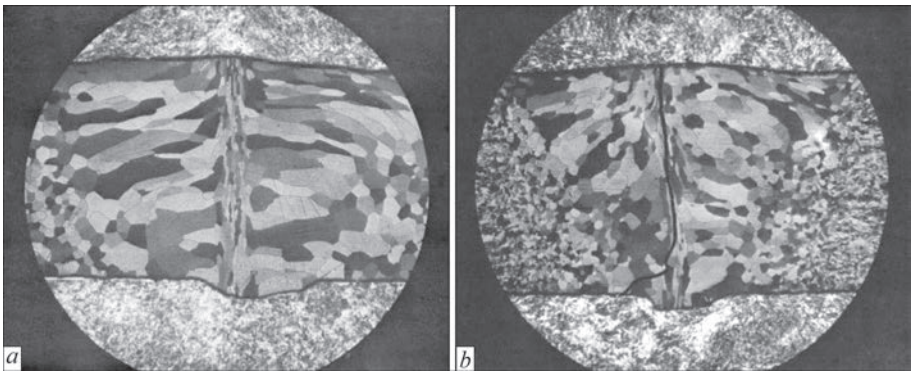

Figure 8. Microstructures (25) of welded joint produced by electron beam welding of beryllium alloys [45]: *a* — alloy C (δ = 1.5 mm), welded with preheating 400 °C, *U* = 100 kV; *I* = 7 mA; *v* = 8.5 mm/s; *b* — typical failure of welded joint of alloy A (δ = 2.5 mm) after tensile test

of temperature distribution in the process of their laser welding. Effect of laser power, radius of focusing spot and its displacement on temperature distribution in cylinder shells from beryllium was determined using a numerical modeling and multi-factor regression analysis.

The experiments carried in work [48] determined that the beryllium welded joints produced without filler material are characterized with very low ductility with strength about 50 % of base metal strength. Strength of the beryllium welded joints produced with aluminium filler materials made 70 % of base metal. Produced joints are characterized with high ductility.

THE MAIN GENERAL PECULIARITIES OF WELDING OF LIGHT ALLOYS USING HIGHLY-CONCENTRATED ENERGY SOURCES

The values of microhardness in the weld and heat-affected zone (HAZ) in laser and electron beam welding of light alloys are dramatically by 20–25 % higher than in TIG. A weakening zone in virtually absent in laser and electron beam welding whereas in TIG or MIG welding it spreads at a distance up to 1.0–1.2 mm and more from a fusion zone. Decrease of microhardness of HAZ metal relatively to the base metal makes about 13–14 %. Hardness of the areas of a near-weld zone in welding of hardened material decreases in relation with the base metal. An area of weakening by distance in laser and electron beam welding is 3–4 times less than in arc one.

The main disadvantages of welding of light alloys using highly-concentrated energy sources are the susceptibility to formation of inner pore and hot cracks. The most effective way for pores elimination are removal of oxide film before welding and quality protection of weld pool from atmospheric air. It is reasonable to decrease welding heat input and weld width, use filler materials for cracking elimination. One more variant of crack elimination can be pre- or concurrent heating of the parts being welded. From this point of view hybrid laser-arc and laser-plasma processes [49] are of high interest.

Application of the optimum modes of welding of light alloys using highly-concentrated energy sources, in particular in a range of rates more than 1.5–2.5 m/min, allows significantly reducing part deformation [50]. The investigations showed that the values of transverse shrinkage of the joints made by laser welding is 5–6 times less than in TIG welding [31, 51].

Unsatisfactory technological capacity to welding of 7xxx series alloys is caused by their high susceptibility to crack formation, high heat expansion coefficient and low temperature of evaporation of alloying elements such as zinc and magnesium that promotes appearance of cracks and porosity in welds. Work [25] demonstrates that the welds made by laser welding have higher tensile strength than in arc TIG welding. Work [35] shows that electron beam welding method is also reasonable for application with 7xxx series alloys. It was determined that hardness of a fusion zone is not improved after aging treatment and properties of HAZ are deteriorated independent on the welding method that indicates limitation of the possibility of increase of joint strength when using any welding process.

THE MAIN RESULTS OF ANALYSIS OF WELDING OF ALUMINIUM AND BERYLLIUM-BASED ALLOYS

It is advisable to perform welding of beryllium and high-strength aluminium alloys in vacuum (electron beam) or in a chamber with controlled atmosphere (for example, with agron under 100–101 Pa pressure) using fiber laser radiation. For welding of the part with small (δ = 1–3 mm) wall thickness the process rate shall be taken from 120 m/h and more (fore example, 150–200 m/h). At that radiation power lies in up to 1.0 kW limits. The expected peculiarities of weld structure formation are growth of grains and dendrites to the sides as for vertical axis of weld cross-section. This results in joint strength decrease. One more peculiarity of beryllium welding is high susceptibility to crack formation. In order to eliminate a danger of crack formation it is reasonable to reduce welding heat input and use pre- or concurrent heating (for example up to 150–200 °C).

The strength limit of light alloy joints made by welding using highly-concentrated energy sources depends on composition and can make 0.8–0.9 of base metal strength for aluminium alloys with satisfactory technological capacity to welding as well as about 0.5–0.7 for difficult-to-weld beryllium alloys. Failure of the joints welded without filler takes place mainly on a weld and ones welded with filler on a transition zone. The mechanical properties of welded joins are affected by weld composition which is changed due to evaporation of the alloying elements from a weld pool, particularly, such as magnesium, lithium, zinc etc. Decrease of content of these elements in the weld after welding can reach to 1.0–1.5 %.

In a series of cases after welding it is reasonable to carry out additional treatment of the produced joints in order to increase their mechanical properties. It can be heat treatment (annealing type), mechanical (for example, ultrasonic peening of welds) or any other.

One of the innovative methods of increase of welded joint quality is laser shock peening (LSP) [54], which was used for treatment of parts of aluminium alloy 7075 preliminary welded by laser radiation. The produced samples were subjected to corrosion strength examination under effect of mechanical tensile stresses using electron scanning microscopy (SEM) and slow strain rate testing (SSRT). The results showed that LSP treatment allows significantly rising corrosion resistance of the joints. Mechanical SSRT tests showed that the samples with LSP treatment have increased failure time and static toughness in comparison with untreated samples by 11, 20 and 100 % relatively to time and intensity of treatment. LSP also effects the change of nature and location of a fracture — type of crack propagation changes from inter to intracrystalline one. Such improvement of the joint properties is related, first of all, with microstructure refinement and decrease of the level of residual stresses.

CONCLUSIONS

1. Welding using highly-concentrated heat sources of wide range of light alloys can provoke such typical defects as hot cracks, inner pores, weakening of near-weld zone, weld sagging, undercuts and irregular nature of formation of reinforcement bead. To minimize the tendency to formation of indicated defects and production of quality joints it is relevant thoroughly select the welding mode parameters, remove oxide film from the blank surface before welding, provide reliable protection of the weld pool from effect of air, in separate cases use filler materials and pre- or concurrent heating. One of the advanced methods of elimination of indicated defects is application of hybrid laser-arc and laser-plasma welding methods.

2. The welds made by electron beam and laser (CO_2 and fiber laser) welding methods are quite similar by appearance as well as microstructure state and main geometry characteristics. Parameters of weld strength and heat input necessary for full metal penetration are somewhat different for various welding methods. Usually the heat input is approximately by 30 % lower for fiber laser than in CO_2-laser application.

3. Volume of molten metal in electron beam and laser methods is significantly smaller than in arc welding. In comparison with TIG and MIG welding there are significant decrease of weld width, 3–4 times drop of area of HAZ weakening and 5–6 times of level of residual deformations of the parts, whereas microhardness of the weld and HAZ rises by 20–25 %. The alloyed filler materials based on aluminium are good to be used for elimination of concavity of weld, increase of allowable assembly gap, increase of mechanical properties and decrease of metal susceptibility to crack formation.

4. Electron beam and laser welding of aluminium alloys provide welded joint strength at a level close to 80–90 % of base metal strength. In case of welding of beryllium alloys without filler material the joint strength is close to 50 % of base metal and at use of filler material based on aluminium it makes about 70 %.

5. The main peculiarity of gas-shielded laser welding of light alloys is the presence of a threshold values of penetration energy that is caused by intensive (over 90–95 %) reflection of laser radiation from the surface of welded blank as well as high values of alloy thermal conductivity. Energy input from 10^6 W/cm^2 is required in order to overcome the penetration threshold. Welding of the blank edges of up to 3.0 mm thickness shall be carried out using fiber laser radiation in argon shieldinged atmosphere with a rate over 120 m/h at radiation energy to 800–1000 W.

6. In beryllium welding the nature of growth of dendrites in solidification of weld pool results in decrease of weld strength, initiation of axial as well as transverse hot cracks is possible. The most dangerous zones for crack initiation are the crater being solidified as well as weld defects. Susceptibility of welds to crack formation can be reduced by means of application of preheating, decrease of welding heat input, usage of filler materials of specific composition, smooth reduction of power of highly-concentrated heat source at the end of welding process, removal of BeO oxide film before welding, minimizing the grain size of the initial material.

The work was carried out under the support of the following projects:

The National Key Research and Development Program of China — in the framework of the strategy «One Belt — One Road» (grant number 2020YFE0205300).

Strategic project of the Academy of Sciences of Guangdong Province, (GDAS'Proj-

ect of Science and Technology Development, 2020GDASYL-20200301001), China.

Project of the Guangzhou Economic and Technological Development Zone 2019GH19), China.

REFERENCES

1. Steen, W., Mazumder, J. (2010) *Laser material processing*. London, Springer. DOI: https://doi.org/10.1007/978-1-84996-062-5
2. Kuneš, J. (2012) *Dimensionless Physical Quantities in Science and Engineering.* Elsevier. DOI: https://doi.org/10.1016/C2011-0-06212-9
3. Doshi, S.J., Gohil, A.V., Mehta, N.D., Vaghasiya, S.R. (2018) Challenges in fusion welding of Al alloy for body in white. *Materials Today: Proceedings*, **5**, 2, 1, 6370–6375. DOI: https://doi.org/10.1016/j.matpr.2017.12.247
4. Khokhlatova, L.B., Blinkov, V.V., Kondratyuk, D.I. et al. (2015) Structure and properties of sheet welded joints from 1424 and v-1461 alloys produced by laser welding. *Aviats. Materialy i Tekhnologii*, **4**, 9–13. DOI: https://doi.org/10.18577/2071-9140-2015-0-4-9-13.
5. (2019) 6xxx Aluminium Alloy Datasheets, Properties and Selection of Aluminium Alloys. Eds by K. Anderson, J. Weritz. *ASM Handbook*. **2B**, 374–375. DOI: https://doi.org/10.31399/asm.hb.v02b.a0006708
6. (2019) 7xxx aluminium alloy datasheets, properties and selection of aluminium alloys. Eds by K., Anderson, J., Weritz et al. *ASM Handbook*, **2B**, 410–412. DOI: https://doi.org/10.31399/asm.hb.v02b.a0006726
7. Malikova, A.G., Ivanova, M.Yu. (2016) High-strength laser welding of aluminium-lithium scandium-doped alloys. *AIP Conf. Proc.*, **1783**, 020148. DOI: https://doi.org/10.1063/1.4966441
8. Fridlyander, I.N. (2008) *Beryllium alloys as a prospective direction of aerospace materials science*. VIAM/2008-205145 [in Russian].
9. Urminsky, J., Marônek, M., Bárta, J. et al. (2020) Electron beam welding of aluminium alloy AW2099. *Mater. Sci. Forum*, **994**, 28–35. DOI: https://doi.org/10.4028/www.scientific.net/MSF.994.28
10. Ma, J., Pierce, K. (2021) New shielding gas mixture for laser conduction welding of aluminium with a filler wire. *J. of Laser Applications*, **33**, 042018. DOI: https://doi.org/10.2351/7.0000471
11. Cao, X., Wallace, W., Poon, C., Immarigeon, J.-P. (2003) Research and progress in laser welding of wrought aluminium alloys. I. Laser Welding Processes. *Materials and Manufacturing Processes*, **18**, 1–22. DOI: https://doi.org/10.1081/AMP-120017586
12. Cai, C., He, S., Chen, H., Zhang, W. (2019) The influences of Ar–He shielding gas mixture on welding characteristics of fiber laser-MIG hybrid welding of aluminium alloy. *Optics & Laser Technology*, **113**, 37–45. DOI: https://doi.org/10.1016/j.optlastec.2018.12.011
13. Reisgen, U., Olschok, S., Mavany, M., Jakobs, S. (2011) Laser beam submerged arc hybrid welding. *Physics Procedia*, **12**, 179–187. DOI: https://doi.org/10.1016/j.phpro.2011.03.023
14. Reisgen, U., Olschok, S., Engels, O. (2020) Visualization of the molten pool of the laser beam submerged arc hybrid welding process. *Welding in the World*, **64**, 721–727. DOI: https://doi.org/10.1007/s40194-020-00873-8
15. Shiganov, I., Kholopov, A. (2020) Laser welding of aluminium alloys. *Fotonika*, **3**, 6–10.
16. Mathers, G. (2002) The welding aluminium and its alloys. *Woodhead Publishing Series in Welding and Other Joining Technologies*, 1st Ed., October 8, 978–1855735675
17. Zhu, G., Wang, S., Cheng, W. et al. (2019) Investigation on the surface properties of 5A12 aluminium alloy after Nd: YAG laser cleaning. *Coatings*, 9(**9**), 578–593. DOI: https://doi.org/10.3390/coatings9090578
18. Khaskin, V.Yu. (2013) Development of laser welding of aluminium alloys at the E.O. Paton electric Welding Institute (Review). *The Paton Welding J.*, **5**, 51–55.
19. Kah, P., Lu, J., Martikainen, J., Suoranta, R. (2013) Remote laser welding with high power fiber lasers. *Engineering*, **05**(09), 700–706. DOI: https://doi.org/10.4236/eng.2013.59083
20. Powel, J., Ilar, T., Frostevarg, J., Torkamany, M.J. (2015) Weld root instabilities in fiber laser welding. *J. of Laser Applications*, **27**, S29008-1–S29008-5. DOI: https://doi.org/10.2351/1.4906390
21. Skryabinskyi, V.V., Nesterenkov, V.M., Mykytchyk, A.V. (2022) Electron beam welding of aluminium 1570 alloy and mechanical properties of its joints at cryogenic temperatures. *The Paton Welding J.*, **1**, 22–25. DOI: https://doi.org/10.37434/tpwj2022.01.05
22. Zhan, X., Yu, H., Feng, X. et al. (2019) A comparative study on laser beam and electron beam welding of 5A06 aluminium alloy. *Materials Research Express*, 6(**5**), 056563. DOI: https://doi.org/10.1088/2053-1591/ab0562
23. Coelho, B.N., M.S.F. de Lima, S.M. de Carvalho, A.R. da Costa (2018) A comparative study of the heat input during laser welding of aeronautical aluminium alloy AA6013-T4. *J. Aerosp. Technol. Manag., São José dos Campos*, **10**, e2918. DOI: https://doi.org/10.5028/jatm.v10.925
24. Çam, G., Ventzke, V., J.F. dos Santos et al. (1999) Characterisation of electron beam welded aluminium alloys. *Sci. and Technol. of Welding & Joining*, 4(**5**), 317–323. DOI: https://doi.org/10.1179/136217199101537941
25. Mastanaiah, P., Sharma, A., Reddy, G.M. (2018) Process parameters-weld bead geometry interactions and their influence on mechanical properties: A case of dissimilar aluminium alloy electron beam welds. *Defence Technology*, 14**(2)**, 137–150. DOI: https://doi.org/10.1016/j.dt.2018.01.003
26. Mercana, E., Ayanb, Y., Kahrama, N. (2020) Investigation on joint properties of AA5754 and AA6013 dissimilar aluminium alloys welded using automatic GMAW Author links open overlay. *Engin. Sci. and Technol.,* 23**(4)**, 723–731. DOI: https://doi.org/10.1016/j.jestch.2019.11.004
27. El-Batahgy, A.M., Klimova-Korsmik, O., Akhmetov, A., Turichin G. (2021) High-power fiber laser welding of high-strength AA7075-T6 aluminium alloy welds for mechanical properties research. *Materials (Basel)*, 14(**24**), 7498. DOI: https://doi.org/10.3390/ma14247498
28. Han, X., Yang, Z., Ma, Y. et al. (2020) Comparative study of laser-arc hybrid welding for AA6082-T6 aluminium alloy with two different arc modes. *Metals*, **10**, 407. DOI: https://doi.org/10.3390/met10030407
29. Khaskin, V.Yu., Korzhik, V.N., Sydorets, V.N. et al. (2015) Improving the efficiency of hybrid welding of aluminium alloys. *The Paton Welding J.*, **12**, 14–18. DOI: https://doi.org/10.15407/tpwj2015.12.03
30. Lalvani, H., Mandal, P. (2021) Cold forming of Al-5251 and Al-6082 tailored welded blanks manufactured by laser and electron beam welding. *J. of Manufacturing Processes*, **68**, Pt A, 1615–1636. DOI: https://doi.org/10.1016/j.jmapro.2021.06.070
31. Shiganov, I.N., Shakhov, S.V., Kholopov, A.A. (2012) Laser welding of aluminium alloys for aircraft purpose. *Inzh. Zh.: Nauka i Innovatsii*, 6(**6**), 34–50. DOI: https://doi.org/10.18698/2308-6033-2012-6-224.
32. Khaskin, V., Korzhyk, V., Peleshenko, S., Wu, B. (2015) Study the impact of technological scheme of a hybrid laser-arc welding on welds formation. *Wschodnioeuropejskie Czasopismo Naukowe (East European Scient. J.)*, **2**, 141–150.

33. Malikov, A., Orishich, A., Karpov, E. Vitoshkin, I. (2019) Laser welding of aluminium alloys for the aircraft industry. *IOP Conf. Series: Materials Sci. and Engineering*, **681**, 012029, 1–6. DOI: https://doi.org/10.1088/1757-899X/681/1/012029
34. Zhao, H., White, D.R., DebRoy, T. (1999) Current issues and problems in laser welding of automotive aluminium alloys. *Inter. Materials Reviews, ASM Inter.*, 238–266. DOI: https://doi.org/10.1179/095066099101528298
35. Cao, X., Wallace, W., Immarigeon, J.-P., Poon, C. (2003) Research and progress in laser welding of wrought aluminium alloys. II. Metallurgical microstructures, defects, and mechanical properties. *Materials and Manufacturing Processes*, 18(**1**), 23–49. DOI: https://doi.org/10.1081/AMP-120017587
36. Xiao, R., Zhang, X. (2014) Problems and issues in laser beam welding of aluminium–lithium alloys. *J. of Manufacturing Processes*, **16**, 166–175. DOI: https://doi.org/10.1016/j.jmapro.2013.10.005
37. Loginova, I., Khalil, A., Pozniakov, A. et al. (2017) Effect of pulse laser welding parameters and filler metal on microstructure and mechanical properties of Al–4.7Mg–0.32Mn–0.21Sc–0.1Zr alloy. *Metals-Open Access Metallurgy J.*, 12(**7**), 564–572. DOI: https://doi.org/10.3390/met7120564
38. Stange, A.W., Hilmas, D.E., Furman, F.J. (1996) Possible health risks from low level exposure to beryllium. *Toxicology*, 111(**1–3**), 213–224. DOI: https://doi.org/10.1016/0300-483x(96)03378-1
39. Hill, M., Damkroger, B.K., Dixon, R.D., Robertson, E. (1990) Beryllium weldability. *Los Alamos National Laboratory, Materials Weldability Symposium, ASM Materials Week, Detroit, Michigan (USA)*. Permalink, https://www.researchgate.net/publication/236557474
40. Veness, R., Simmons, G., Dorn, C. (2011) Development of beryllium vacuum chamber technology for the LHC. In: *Proc. of IPAC2011, San Sebastián, Spain, TUPS024*, 1578–1580.
41. Gurevich, S.M. (1990) *Reference book on welding of non-ferrous metals*. Ed. by V.N. Zamkov. 2nd Ed. Kyiv, Naukova Dumka [in Russian].
42. Hanafee, J.E., Ramos, T.J. (1995) Laser fabrication of beryllium components. *2nd International Energy Agency International Workshop on Beryllium Technology for Fusion (Moran, Wyoming, USA, September 6–8)*.
43. Falkner, G.E., Ramos, T.J., Murchie, J.R. (1982) *Laser welding beryllium in a deuterium atmosphere*. Lawrence Livermore National Laboratory Report UCID-19602, Order Number DE83003312, Nov.
44. Manly, W.D., Dombrowski, D.E., Hanafee, J.E. et al. (1995) Report of a Technical Evaluation Panel on the Use of Beryllium for ITER Plasma Facing Material and Blanket Breeder Material. *Sandia National Laboratories* (USA), SAND95-1693 UC-420.
45. Campbell, R.P., Dixon, R.D., Liby, A.L. (1978) *Electron beam fusion welding of beryllium.* Rockwell International (USA), RFP-2621, January 1.
46. Criss, E.M. (2015) *Surrogacy of beryllium welds and heat transfer in metals:* Dis. for the degree Dr. of Philosophy (Mechanical Engineering), University of California, San Diego (USA). Permalink: http://escholarship.org/uc/item/8sx939v4
47. *Shao Rong* Yu, Yi Xia Yan, Zhi Ming Hao et al. (2009) Analysis of temperature distribution and its influencing factors in laser welding of beryllium cylindrical shells. *Key Engineering Materials*, **419–420**, 449–452. DOI: https://doi.org/10.4028/www.scientific.net/KEM.419-420.449
48. Komarov, M.A., Guitarsky, L.S. (2015) Welding of beryllium. *Welding Inter.*, 29(**7**), 561–566. DOI: https://doi.org/10.1080/09507116.2014.952497
49. Korzhyk, V., Khaskin, V., Grynyuk, A. et al. (2022) Comparison of the features of the formation of joints of aluminium alloy 7075 (Al–Zn–Mg–Cu) by laser, microplasma, and laser-microplasma welding. *Eastern-European J. of Enterprise Technologies*, **1**(12(115), 38–47. DOI: https://doi.org/10.15587/1729-4061.2022.253378
50. Bondarev, A.A., Nesterenkov, V.M. (2011) Electron beam welding of thin-sheet three-dimensional structures of aluminium alloys. *The Paton Welding J.*, **6**, 36–39.
51. Narsimhachary, D., Ravi N. Bathe, Padmanabham, G., Basu, A. (2014) Influence of temperature profile during laser welding of aluminium alloy 6061 T6 on microstructure and mechanical properties. *Materials and Manufacturing Processes*, **29**, 948–953. DOI: https://doi.org/10.1080/10426914.2013.872258
52. Kang, M., Lee, K. (2017) A review of joining processes for high-strength 7xxx series aluminium alloys. *J. of Welding and Joining*, 35(**6**), 79–88. DOI: https://doi.org/10.5781/JWJ.2017.35.6.12
53. Klochkov, I.N., Nesterenkov, V.M., Berdnikova, E.N., Motrunich, S.I. (2019) Strength and fatigue life of joints of high-strength alloy AA7056-T351, made by electron beam welding. *The Paton Welding J.*, **1**, 10–14. DOI: https://doi.org/10.15407/tpwj2019.01.03
54. Wang, J.T., Zhang, Y.K., Chen, J.F. et al. (2015) Effects of laser shock peening on stress corrosion behavior of 7075 aluminium alloy laser welded joints. *Materials Sci. and Eng. A. Structural Materials*: *Properties, Microstructure and Processing*, **647**, 7–14. DOI: http://dx.doi.org/10.1016/j.msea.2015.08.084

ORCID

S.I. Peleshenko: 0000-0001-6828-2110,
V.Yu. Khaskin: 0000-0003-3072-6761,
V.M. Korzhyk: 0000-0001-9106-8593,
V.V. Kvasnytskyi: 0000-0002-7756-5179,
A.A. Grynyuk: 0000-0002-6088-7980,
I.M. Klochkov: 0000-0001-6490-8905,
D. Chunling: 0000-0003-2672-5985,
A.O. Alyoshin: 0000-0001-9696-6800

CONFLICT OF INTEREST

The Authors declare no conflict of interest

CORRESPONDING AUTHOR

V.Yu. Khaskin
China-Ukraine Institute of Welding, Guangdong Academy of Sciences, Guangdong Provincial Key Laboratory of Advanced Welding Technology
510650, Guangzhou, China.
E-mail: khaskin1969@gmail.com

SUGGESTED CITATION

S.I. Peleshenko, V.Yu. Khaskin, V.M. Korzhyk, V.V. Kvasnytskyi, A.A. Grynyuk, I.M. Klochkov, D. Chunling, A.O. Alyoshin (2022)
Features of welding high-strength alloys based on aluminium and beryllium using highly-concentrated heat sources (Review). *The Paton Welding J.*, **12**, 9–18.

JOURNAL HOME PAGE

https://patonpublishinghouse.com/eng/journals/tpwj

Received: 02.10.2022
Accepted: 30.01.2023

DOI: https://doi.org/10.37434/tpwj2022.12.03

PRODUCING NITINOL BRAZED JOINTS (REVIEW)

S.V. Maksymova, B.V. Stefaniv

E.O. Paton Electric Welding Institute of the NASU
11 Kazymyr Malevych Str., 03150, Kyiv, Ukraine

ABSTRACT

Shape-memory alloys are becoming ever wider accepted in different industries, in particular in aerospace, medical, automotive sectors and in consumer electronics manufacturing. Application of these materials as hybrid structure elements is a promising direction when creating products with a unique set of properties: high mechanical values, superelasticity, damping ability, higher wear resistance and thermomechanical memory. Production of nitinol permanent joints by welding leads to formation of brittle phases of Ti_2Ni type, which degrade the product quality. This review discusses the possibility of producing high-strength permanent joints of nitinol with nitinol and with other alloys by brazing. The main advantage, compared to other methods, is the fact that the base metals do not melt, and some structural transformations can be avoided. At nitinol brazing in the atmosphere, brazing filler metals of Ag–Cu–Zn–Sn–Ni system have proven themselves well, when using 25AgCl–25KF–50LiCI flux. We should specially mention application of silver brazing filler metals and interlayers from pure metals, for instance, niobium, providing a strong metallurgical bond with the base metal. At brazing temperature of 1180 °C an alloy based on quasibinary NiTi–Nb eutectic system is formed, ensuring the reliability of brazed elements when creating prototypes of superelastic honeycomb shapes from titanium nickelide.

KEYWORDS: titanium nickelide (nitinol), shape-memory alloys (SMA), brazing filler metals, brazing, welding, wetting, intermetallic brittle compounds, strength, structure

INTRODUCTION

Nowadays alloys with a reverse martensite transformation, characterized by varying degrees of shape-memory properties, are of considerable interest. These are Ni–Ti; Ni–Ti–Cu, Ni–Ti–Pd; Ni–Ti–Fe; Ni–Ti–Nb, Ni–Fe–Ga, Ni–Ti–Co, Ni–Al, Ni–Co, Ti–Nb; Fe–Ni, Cu–Al, Cu–Al–Ni, Pt–Ti, Ag–Cd, Au–Cd, etc. [1, 2], and they are widely accepted in different engineering sectors. After plastic deformation, these alloys restore their original geometry as a result of heating (shape-memory effect) or directly after load removal (superelasticity). The mechanism determining the shape memory properties is the reverse crystallographic thermoelastic martensite transformation — Kurdyumov effect. This is a kind of polymorphous phase transition with a change of crystalline lattice that depends of temperature or loading level. Martensite transformation is accompanied by volume change, ensuring the shape memory [3]. The high-temperature phase is austenite, which transforms into martensite (low-temperature phase) at stress application. After stress relieving, martensite transforms into austenite and restores its original shape. Such processes can run several times at thermal cycling [4, 5].

A typical representative of shape-memory materials is nitinol (Figure 1), in which a transition from the cubic (B2 austenitic phase) into a monoclinal phase (B19 martensite) takes place at cooling or under the impact of applied stresses [6, 7]. Special corrosion resistance of titanium nickelide is due to its ability to form TiO_2 oxide on its surface, which acts as a protective barrier owing to its pronounced hydrophobic properties that prevents nickel dissolution in an aggressive environment of the human body and ensures its complete biocompabitility on the level of corrosion-resistant steels (316LVM (03Kh18N14M2) and Ti–6V–4Al alloy [8]. It belongs to the best studied shape-memory materials, is applied in different industries and is the most promising material for manufacturing superelastic medical implants (in biomedicine, owing to its biological compatibility and corrosion resistance in the human body), tool (Figure 2, *a–c*), as well as in automotive and microelectronic sectors and in manufacture of thermomechanical elements for aerospace and aviation engineering (aircraft, rockets, space structures with improved flight characteristics

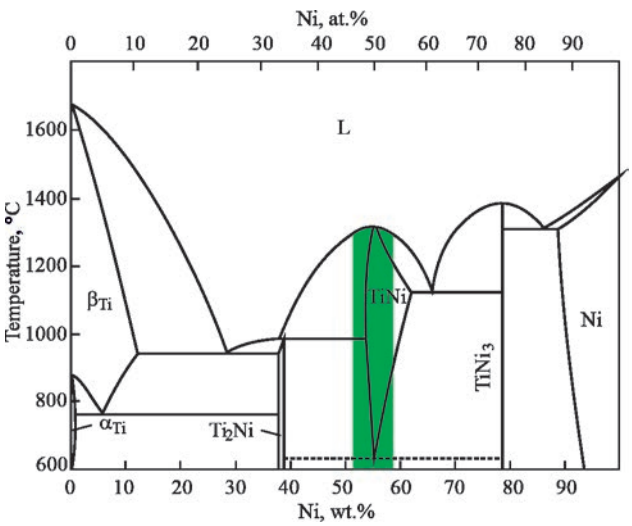

Figure 1. State diagram of Ni–Ti system [7]

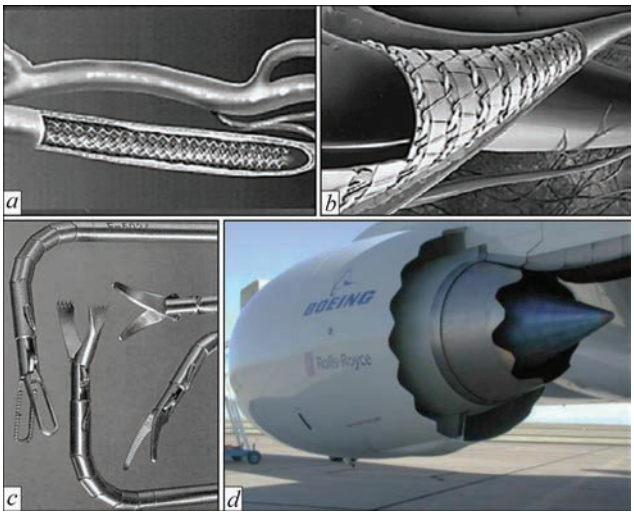

Figure 2. Medical stents (*a*, *b*), tool (*c*), serrated nozzle of aircraft (*d*) [9]

and lower level of noise and vibrations) (Figure 2, *d*) [9]. Application of this material when creating structures with certain service characteristics requires investigation and development of different joining processes that may lead to its wider application. Nowadays, the process of joining nitinol in similar and dissimilar combinations is insufficiently studied.

This review considers the possibilities of producing permanent joints of an intermetallic alloy — nitinol with application of different methods of high-temperature brazing and using pure metal interlayers, ensuring contact melting at the temperature that is much lower than their autonomous melting temperature.

PRODUCING PERMANENT JOINTS OF NITINOL (NiTi)

Nitinol is an alloy based on an equiatomic intermetallic compound, which contains titanium and nickel. The concentration of the latter is from 48 to 52 at.%.

Unique functional properties of nitinol are due to the temperature and rate of deformation, chemical composition, heat treatment parameters, etc. Even a slight change of nickel concentration within 2 % (from 50 to 52 at.%) leads to lowering of phase transition temperature by almost 27–127 °C that enables controlling the physico-mechanical properties in a certain temperature range [4].

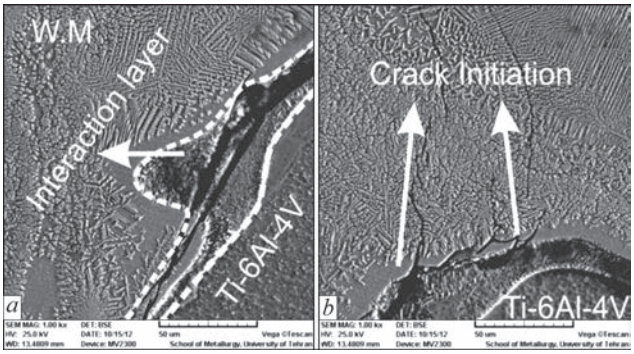

Figure 3. Reaction layer near the interface with Ti–6Al–4V titanium alloy (*a*) and cracks (*b*) at laser welding of dissimilar materials of nitinol with titanium alloy [11]

Various welding methods are widely used for the processes of material joining: arc, laser, beam, contact, explosion, friction, diffusion welding etc. [1, 4, 9]. Joining shape-memory alloys (SMA) by welding is possible, but it has a tendency to formation of intermetallic phases (Ti_2Ni), which are characterized by considerable brittleness [9, 10]. Moreover, deterioration of shape-memory effect is possible, which is the result of high-temperature, partial melting of base metal and presence of a cast dendritic structure in the seam zone. It is obvious that welding changes the phase transformation temperature that may reduce the area of its application. When welding the shape-memory alloys, it may be necessary to apply alloying elements preventing formation of intermetallic phases, but such data are very scarce at present [5].

Application of the method of shock capacitor-discharge welding [1] did not provide joints of sufficient strength. It should be noted that low strength values are found in the case of absence of intersolubility of dissimilar materials being welded [10]. At application of fusion welding, a transition cast HAZ always forms, which may have increased brittleness, compared to the base metal. It significantly lowers the welded joint strength, particularly in the case, when one of the materials being joined is an intermetallic alloy which already has low ductility.

Laser welding usually results in formation of narrow welds, and it can be better than the arc process, due to the possibility to produce finely dispersed microstructure and lower thermal stresses and strains, remaining after the welding cycle. The laser welding method allows producing joints of nitinol with titanium with tensile strength of 109 MPa and its joints with Ti–6Al–4V alloy with the strength of 28.4 MPa. In welded joints produced by electron beam and argon-arc welding (TIG), this value was 70, 85 and 108 MPa, respectively [10]. The cause for low mechanical properties is formation of Ti_2Ni brittle phase in the weld zone, in which microcracks initiate (Figure 3) [11].

Application of a copper interlayer during laser welding of nitinol with Ti–6Al–4V titanium alloy leads to lowering of weld microhardness that is due to lower microhardness of Ti_2Cu intermetallic phase rich in titanium, compared to a similar characteristic of Ti_2Ni phase. It allows reducing the amount of brittle Ti_2Ni intermetallic phase, avoid formation of transverse cracks in the weld and increasing the joint strength to 300 MPa [11].

Table 1. Chemical composition of brazing filler metals [12]

System	Chemical elements, wt.%					Melting range, °C
	Ag	Cu	Zn	Sn	Ti	
AgCu (eutectic)	71.9	28.1	–	–	–	779
AgCuZnSn I	52	22	18	8	–	590–635
AgCuZnSn II	50–68	10–30	12–20	0–10	–	640–730
AgCuTi I	70.5	26.5	–	–	3	780–805
AgCuTi II[1]	63	35.25	–	–	1.75	780–815
AgCuTi III[2]	68.8	26.7	–	–	4.5	830–850
AgTi	96	–	–	–	4	970

[1]Cusil ABA. [2]Ticusil®.

PRODUCING NITINOL JOINTS WITH APPLICATION OF BRAZING FILLER METALS

As regards brazing, there exists a multitude of processes, usually named by the heating methods: flame, induction, ultrasonic, dip brazing, etc.

During brazing, the base metals do not melt that may promote avoiding some high-temperature processes, which include high-temperature oxidation, element segregation, grain coarsening, that may impair the original properties of base metal — SMA. Brazing [10] provides wide possibilities of variation of the phase and chemical composition of the joint zone. At brazing, however, the base metal interacts with the brazing filler metal and diffusion processes take place. Shape-memory alloys on the whole and NiTi in particular are rather active to oxygen, carbon, nitrogen and hydrogen, making certain requirements to brazing atmosphere. Vacuum brazing conditions can be more attractive, compared to other methods. It is recommended to perform vacuum brazing using ductile brazing filler metals (Table 1), which contain active elements [12].

In the presented brazing filler metals (Table 1) the base is Ag–Cu system alloy, which is alloyed by an adhesion-active element — titanium. Other studies reported application of Au and Au- [13] and Nb-based alloys [14], as alloying elements.

Vacuum brazing (rarefaction of 10^{-3} Pa) with eutectic Ag–Cu brazing filler metal (72 wt.% Ag, melting temperature of 779 °C) can provide quite good strength and ductility, but it depends on the overlap length [12]. A significant increase of strength is achieved at increase of overlap length from 1 to 4 mm. The brazed specimen with overlap size within 1 and 2 mm fails at the load of 360 and 600 N, respectively, while a specimen with 4 mm overlap fails at 980 N (close to 820 MPa).

The produced microstructure (Figure 4) was used as an example to show formation of a typical classic eutectic structure of a brazed seam at application of brazing filler metals of Ag–Cu system, which is created by two solid solutions based on silver (white matrix) and on copper (dark rods).

Shear strength of the brazed joint is higher than 100 MPa, and rupture occurs in the reaction layer adjacent to the base metal and brazing filler metal. The brazed specimen demonstrates a good shape memory [15].

The reaction layer on the interface between the base metal and brazed seam metal [15] is identified as a phase of XTi_2 type, where X = Ni + Ag + Cu. According to a binary state diagram, Ni and Cu have complete mutual solubility at brazing temperature, while at low temperature (354 °C) the spinodal disintegration causes separation into α_1 and α_2 phases. As there is no thermodynamic barrier for the reaction in the spinodal region, disintegration is determined solely by diffusion. No intermetallics form in binary state diagrams of Ag–Cu and Ag–Ni metal systems. Moreover, limited solubility of nickel in silver is observed, however, all the elements (Ag, Cu, Ni) form numerous intermetallic compounds with titanium (Table 2). It may lead to formation of intermetallics on the interface of brazing filler metal — base metal [13].

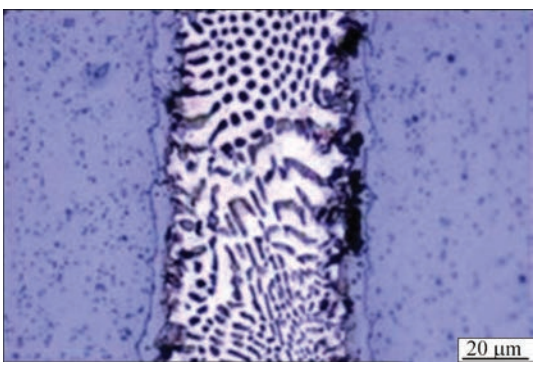

Figure 4. Microstructure of NiTi/NiTi brazed joint [15]

Table 2. Intermetallics in Ti_xX_y system (X = Ag, Cu, Ni) [16]

Element	Compounds					
Ag	AgTi	$AgTi_2$	–	–	–	–
Cu	Cu_4Ti	Cu_2Ti	Cu_3Ti_2	Cu_4Ti_3	CuTi	$CuTi_2$
Ni	Ni_3Ti	NiTi	$NiTi_2$	–	–	–

At application of commercially available brazing filler metals, mainly based on Ag–Cu system alloy [12], special attention is given to studying the nitinol brazing processes with application of infrared, laser and microwave heating. At brazing, similar to welding, a certain deterioration of the original base metal properties is to be anticipated due to formation of intermetallic phases. On the one hand, running of the diffusion processes on the joint boundary promotes achieving strong bonds between the component elements of the base metal and brazing filler metal with formation of common phases, but on the other hand, it can also adversely affect the joint strength, because of their brittle nature, for instance XTi_2 phases (where X = Cu, Ni, Ag).

Copper is known to have a high solubility in nitinol and up to 30 wt.% of nickel in NiTi can be replaced by copper atoms without lowering the SME [17]. Therefore, pure copper and copper-alloyed brazing filler metals (Ti70Cu15Ni15; Cusil: 63 at.% Ag, 35.25 at.% Cu and 1.75 at.% Ti; Ticusil® 68.8 Ag, 26.7 at.% Cu and 4.5 at.% Ti) [9] were used. Microstructural studies showed that three copper-containing phases were present in brazed seams, produced with application of pure copper foil, namely a copper-rich phase containing more than 90 at.% Cu, and CuNiTi (Δ) and Ti(Ni, Cu) phases. It is reported [9] that absence of CuNiTi phases impairs the SME of the alloy, while Ti(Ni, Cu) presence does not have any effect at all on the alloy shape-memory effect. It is noted that the quantity of CuNiTi phase decreases with increase of brazing time that has a positive impact on the shape-memory effect of brazed joints. In brazed joints produced with application of TiCuNi system alloy as brazing filler metal, Ti_2(Ni,Cu) brittle intermetallics forms on the interface of brazing filler metal — base metal, which makes determination of the shape-memory effect difficult. Titanium presence in Cusil-ABA brazing filler metal promotes improvement of base material wetting, but formation of CuNiTi phase impair the shape-memory effect of the produced brazed joint. At brazing by Ticusil® brazing filler metal (with a higher titanium content), $TiCu_2$ intermetallic phase forms in the brazed seam, which has a weaker influence on the shape-memory effect, but at the same time the brazed seams are characterized by a much weaker shape-memory effect, compared to base metal (nitinol) in the initial state [9]. However, brazing remains the most promising method of joining shape-memory materials.

The problem of passive oxide formation may arise both in welding, and in brazing of Ni–Ti alloys. Its formation can be avoided by application of active fluxes and low-temperature brazing filler metals of Sn–Ag or Au–Sn system (from 200 to 300 °C). As an alternative, a barrier coating from nickel or gold can be used before brazing, which may improve the brazed joint quality [12].

A high concentration of titanium, which readily forms resistant oxide films on the surface of the studied NiTi alloy under atmospheric conditions, requires application of flux, where the effective components are fluorides and AgCl, LiCl compounds. Proceeding from the obtained results, the authors [18] decided using a flux consisting of 25 AgCl–25KF–50LiCl (wt.%), which improves wetting by silver brazing filler metal BAg-7 (Table 3) of NiTi surface at high-temperature brazing in air atmosphere.

When making brazed joints, the authors [18] used nitinol “metallization”, which consists in application of flux and brazing filler metal (10 mg) on the surface, heating in an electric furnace up to the temperature of 1000 °C and subsequent cooling. Slag was removed from the specimen surface by a wire brush. After such a preparation, the flux was applied on the “metal-

Table 3. Brazing filler metals and melting temperature [18]

Brazing filler metal (grade)	Chemical elements, wt.%					Solidus, °C	Liquidus, °C
	Ag	Cu	Zn	Sn	Ni		
BAg-7	56.5	20.3	16.3	6.9	–	623	655
A-1	59	23	15	1	2	668	710
A-2	60	30	–	10	–	738	761
A-3	60	28	–	10	2	739	766
A-4	60	30	10	–	–	650	745
A-5	60	28	10	–	2	715	755
A-6	61	24	15	–	–	685	717
A-7	59.5	23.5	15	–	2	688	724
A-8	60.2	23.5	15.3	1	–	655	718

lized" specimens, they were mounted with an overlap of 2.5 mm, 100 g load was applied for fixing the specimens, and in such a position they were placed into an electric furnace. Brazing temperature is in the range of 700 to 900 °C.

In brazed nitinol specimens produced with application of BAg-7 brazing filler metal at the temperature of 900 °C and of A-1 at 930 °C, formation of a reaction layer was observed on brazing filler metal — base metal interface (Figure 5, shown by arrow 1).

Ti and Ni weight ratio (in at.%) in it is equal to 1:3, so that it is identified as $TiNi_3$ intermetallic. The authors [18] regard the following as the specific features of formation of nitinol brazed joints. First of all, a significant liquation of tin is found at application of BAg-7 brazing filler metal, leading to reaction layer enrichment in a large quantity of this element (from 25 to 35 wt.%) that is much higher than its concentration, compared to brazed specimens at application of A-1 brazing filler metal. Secondly, titanium and oxygen peaks are observed on the reaction layer-base metal interface. In other words, titanium oxide is present in these areas, that corresponds to inclusions, observed in the interphase zone (shown by arrow 2). Application of A-1 brazing filler metal, alloyed by tin up to 1 % and by nickel up to 2 % ensures maximum strength of brazed joints on the level of 300 MPa, while other brazing filler metals demonstrated maximum strength, which is lower than 200 MPa [18]. It is noted that Sn and Zn lower the melting temperature of brazing filler metals and improve base metal wetting. At Ni introduction into the brazing filler metal an increase of the amount of the melt and improvement of base metal wetting at brazing are observed. Therefore, it may be assumed that increase of liquid metal amount results in removal of titanium oxide from the interface and increase of brazed joint strength.

NITINOL BRAZING TO OTHER METALS

Earlier study of the potential of SMA application in engineering structures, such as adaptive serrated nozzle (ASN) shows that joining nitinol to titanium-based alloys is an extremely complicated process, which requires systemic studies and development of effective joining methods [9]. Vacuum brazing advantages are known and they consist in ensuring absence of oxygen in furnace atmosphere, and producing clean sound defectfree seams. However, application of vacuum furnaces is not rational for adaptive serrated nozzle manufacturing, so that local heating is to be used. Brazed joints, produced in this study, do not quite meet the requirements made, that is why optimization of the brazing process is required in order to improve the joint properties. It is shown that application of

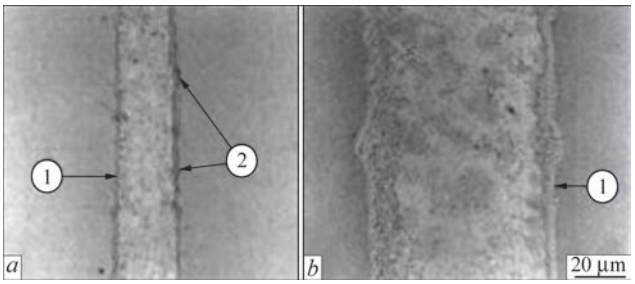

Figure 5. Brazed joint microstructure: *a* — with BAg-7 brazing filler metal; *b* – with A-1 brazing filler metal. Arrow (1) points to $TiNi_3$ intermetallic, arrow (2) — to titanium oxide [18]

interlayers at vacuum brazing improves the brazed joint properties. However, mechanical properties of brazed joints are much lower than those required for an adaptive serrated nozzle. Further optimization of the process and studying the influence of alloying elements and brazing systems will allow improvement of brazed joints [9]. A noticeable improvement of brazed joint quality is achieved at application of brazing filler metals, containing not more than 25 at.% nickel, and alloyed by titanium. Further research is required to study and more precisely determine the titanium impact in the brazing filler metals [9].

Examples of the produced joints of nitinol with Ti–6Al–4V alloy and corrosion-resistant steel are presented in works [9, 19, 20]. Application of silver brazing filler metal BAg-8 allowed producing a permanent joint of maximum shear strength that is equal to 219 MPa [19]. Vacuum brazing of nitinol to Ti–6Al–4V alloy was studied at application of brazing filler metals of Ti–Cu–Ni, Ti–Cu–Ni60 systems and Ti–Ni67 alloy. Maximum shear strength of brazed joints was achieved at application of TiCuNi60 brazing filler metal, and it was equal to approximately 30 MPa [9]. Thus, correct selection of the brazing filler metal chemical composition largely depends on the quality of a permanent joint of nitinol with titanium and its alloys. Note that intermetallic phase formation occurs irrespective of the joint type and joining method.

Studies of wetting, microstructure and strength of brazed dissimilar joints of Ti50Ni50 nitinol with Ti-15-3 alloy (β-Ti alloy type, which is readily deformed and contains in wt.%: 3Al, 3Cr, 3Sn, 15V, Ti) at application of BAg-8 (72Ag–28Cu) (wt.%) and Ticusil® (68.8Ag–26.7Cu–4.5Ti) (wt.%) brazing filler metals showed [21] that wetting of Ti50Ni50 base metal by 72Ag–28Cu eutectic brazing filler metal is greatly improved at addition of 4.5 wt.% Ti to the alloy. Only active Ticusil® brazing filler metal readily wets the substrates of both the base metals at infrared brazing. The structure of Ti-15-3/Bag-8/Ti50Ni50 brazed joint produced at T = 800 °C with soaking for 300 s, consists of Cu_2Ti intermetallics, which crystallize against the background of silver-based sol-

id solution. Now at increase of brazing temperature up to 850 °C (τ = 300 s), just a matrix forms which is enriched in Ag. Formation of Cu(Ti,V) reaction layer on the contact boundary with Ti-15-3 titanium alloy and of $(CuxNi_1–x)_2Ti$ phase is attributed by the authors to active wetting of both the substrates and diffusion processes [21]. The best results of brazed joint strength at application of BAg-8 and Ticusil® brazing filler metals are 197 and 230 MPa, respectively. The shortcomings of these joints include crack formation on the interphase of brazing filler metal–Cu(Ti, V) reaction layer and along the central zone of Ti_2Ni intermetallic compound.

Formation of $(Cu, Ni)_2Ti$ phase is also observed, when brazing dissimilar joints of nitinol with nickel-based superalloy of Hastelloy C-276 grade (containing in wt.%: 55 Ni, 14.5–16.5 Cr; 15–17 Mo; 4–7 Fe; 3–4.5 W). At nitinol brazing to austenitic corrosion-resistant steel a phase with a high content of Fe and Cr forms on the interphase of brazing filler metal-base metal [12]. As formation of the reaction layer is a process controlled by diffusion that is due to a gradient of concentrations, by temperature and time, these parameters in combination with the selected brazing filler metal are highly important at brazing.

During laser brazing of NiTi to corrosion-resistant steel using AgCuZnSn II brazing filler metal shown in Table 1, the low heat input promoted low values of ultimate strength of 190–210 MPa [22]. At application of greater heat input, strength was increased to 320–360 MPa. Considering that the ultimate strength of Ni–Ti base metal in the initial condition was higher than 1100 MPa, the considerable loss of the joint strength was caused by the brazing process. Similar results were obtained at application of AgCuZnSn I brazing filler metal (see Table 1) [12]. As stated by the authors, mutual diffusion of Ag, Cu, Zn and Sn chemical elements occurs. These elements diffuse from the filler metal both into the base metal — NiTi, and into stainless steel, while Ti and Ni from nitinol base metal, and Fe, Cr and Ni from the steel diffuse into the filler metal.

At infrared brazing of joints of nitinol with Ti–6Al–4V titanium alloy containing wt.%: 5.76 Al, 4.03 V, 0.28 Fe, 0.06 C, using copper-silver brazing filler metal BAg-8 (in the form of 50 μm thick foil), good wetting of Ti–6Al–4V titanium alloy and somewhat poorer wetting of nitinol is observed [19]. In keeping with AWS specifications, BAg-8 brazing filler metal contains 71–73 % silver, the balance being copper, and it is characterized by a eutectic structure (T_m = 780 °C) [23, 24]. Investigations showed that after infrared brazing at the temperature below 850 °C, a hypoeutectic structure forms in the seam, which is based on two solid solutions: silver-based and copper-based one. Silver does not react with either of the base metals, and forms no intermetallic compounds, but copper reacts with titanium with formation of $TiCu_4$, Ti_3Cu_4, TiCu and Ti_2Cu intermetallic phases on the interphase of brazing filler metal–titanium alloy (Ti–6Al–4V) and of CuNiTi phase on brazing filler metal – nitinol interface. Titanium partially dissolves in Ti–6Al–4V titanium alloy that improves wetting of both the metals. At increase of brazing temperature to 900 °C (for more than 60 s) and abrupt change of the microstructure occurs, which is due to formation of a large quantity of Ti_2Ni phase. The average strength of the specimens, brazed by infrared radiation at the temperature of 800 °C, is equal to approximately 200 MPa. Although the presence of CuNiTi intermetallic phase has a positive effect on wetting Ti50Ni50 base metal substrate by molten brazing filler metal, it has a negative influence on the strength of Ti50Ni50/BAg-8/Ti–6Al–4V brazed joint [19]. Maximum shear strength values on the level of 343 MPa were obtained at infrared brazing at the temperature of 950 °C (soaking for 60 s) [24].

PRODUCING JOINTS WITH INTERLAYER APPLICATION AND WITHOUT BRAZING FILLER METAL

Investigations in the field of nitinol brazing and welding have been performed for many years. These studies are still relevant and require development of an affordable and inexpensive joining method, which will ensure joint formation without brittle phases at development of specific functional elements of various structures.

The problem of producing strong and reliable structures can be solved by application of interlayers from pure metals on the material to be brazed. Selection of optimal interlayer compositions, which allow avoiding formation of brittle intermetallic phases between titanium and nitinol is an important task of today [10]. Application of the respective ductile interlayer can be a good choice for prevention of excess diffusion and compensation of thermal deformations which are due to mismatch of the coefficients of thermal expansion. Performed research showed that mutual diffusion takes place at niobium contact with the ordinary forged nitinol, leading for formation of the liquid phase, which actively wets both pure niobium and NiTi [5, 25–31].

Performed research was the base for development of a new reactive process of brazing titanium nickelide by application of pure niobium, which provides a strong metallurgical bond with the base metal (quasibinary Ni38Ti36Nb24 eutectic) and opens up possibil-

Table 4. Chemical heterogeneity of brazed joint of NiTi with pure niobium [5]

Studied zone	Element (wt.%)		
	Ni	Ti	Nb
1 (hypoeutectic dendrites)	45.1	47.9	7
2 (NiTi)	49.5	50.5	–
3 (eutectic)	37.3	39.4	23.3

ities for creation of prototypes of superelastic cellular honeycomb shapes from ordinary titanium nickelide. This method allows implementation of complex 3D truss structures, honeycomb panels, and built-in thermally activated multifunctional structures based on Ni–Ti alloy [14].

Pseudoelasticity of shape-memory NiTi alloys is a unique property of the material, which may be characterized by complete recovery of the preformed shape of the component by changing the conditions of thermal or mechanical loading after deformation. Unlike elastic deformation of such ordinary materials as steel, nitinol capabilities are 20 times higher than the elastic deformation rate which is due to increased temperature, or stress, and it promotes diffusion-free transformation of austenite crystalline lattice into martensite and vice versa. Such alloys are often used as components of implants or stents, so that extremely high requirements are made to their reliability and biocompatibility with the human body [5]. From the view point of producing the joints, vacuum brazing is a particularly acceptable method for making joints from components, which preserve maximum pseudoelasticity. In such a study [5], it was shown that the process of vacuum brazing at the temperature of 1180 °C (τ = 6 min) using pure niobium, is readily combined with heat treatment, and it is performed in one cycle of heating in the furnace. NiTiNb eutectic forms in the central zone of the brazed seam, which contains up to 23 % niobium (Figure 6, Table 4, zone 3).

Eutectic composition correlates with other studies, where it was determined that niobium concentration is within 20–26 % [5, 25]. Titanium-based hypoeutectic dendrites containing 7 % niobium are observed between the base material and eutectic (Figure 4, Table 4, zone 1), which corresponds to niobium solubility in NiTi at brazing temperature of 1180 °C [5]. Moreover,

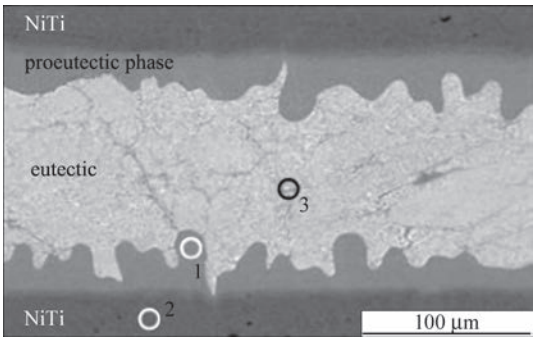

Figure 6. Seam structure with regions where local elemental composition was determined in NiTi brazed joint produced using pure niobium (50 μm) as brazing filler metal (T_m = 1180 °C, τ = 6 min) [5]

it was proved that the fraction of ductile hypoeutectic NiTiNb-phase increased significantly with longer soaking time (Figure 7), and the brazed seam is much wider (100–150 μm), compared to the width of the niobium foil in the initial condition (50 μm).

Maximum tensile strength (1022 MPa) of nitinol specimen was achieved at brazing temperature of 1180 °C with 6 min soaking. Fracture occurred through the eutectic phase and in the hypoeutectic dendrite zone (Figure 7, *d*, *e*). Of considerable interest is investigation of the influence of soaking time and heat treatment on NiTi structure and pseudoelasticity of brazed joints. The authors note that Nb, NbZr1, Cu and AuCu65 are promising for application as brazing filler metals. They provide partially pseudoelastic behaviour in NiTi/NiTi brazed joints [5].

Nititnol wires (300 μm diameter) can be brazed with application of NiTi and Nb powders as brazing filler metals [29], which are mixed with polyvinyl alcohol and water in a certain proportion (to obtain a suspension) and are applied on the contact surfaces of two parallel wires. A liquid phase forms between NiTi and Nb at the temperature of 1170 °C due to a eutectic reaction (in keeping with NiTi–Nb17 quasibinary diagram), which wets the base metal wires, filling the gaps between. Overheating by 10° (up to 1180 °C) and soaking for 4 min promote good wetting and formation of a tight brazed seam, containing a eutectic component (Figure 8).

The seam structure contains round grains of a phase enriched in Nb (N′), rod (R) and platelike (L) eutectic (Figure 8, *b*). Moreover, faceted phase parti-

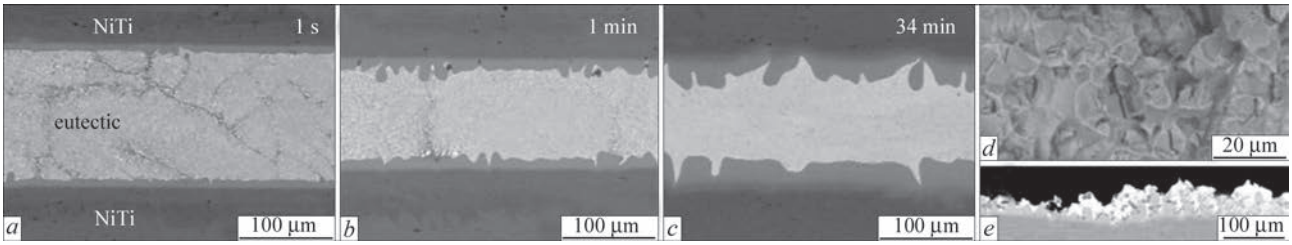

Figure 7. Microstructure of NiTi brazed joint produced under vacuum at brazing temperature of 1180 °C and at different soaking (*a–c*) and fracture surface (*d*) and cross-section of the specimen in the fracture zone (*e*) [5]

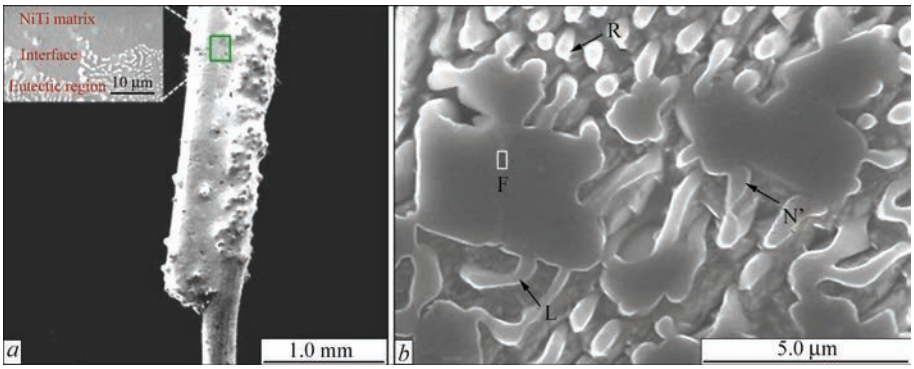

Figure 8. SEM micrographs: *a* — joined parallel NiTi wires; *b* — eutectic region in a polished brazed region. R and L — eutectic microstructure of the rod and platelike, respectively; N′ — Nb-rich rounded phase, F — Ti-rich faceted particle [29]

cles are present, which are enriched in titanium (F). It is reported that the rod-type eutectic forms, when the volume fraction of Nb phase in NiTi–Nb eutectic is below the critical volume (close to 30 %) for platelike eutectic [29]. The authors of [29] found that phase transformation of B2 into B19′ slows down after heat treatment at 520 °C for 30 min, both for NiTi wire, and for the eutectic region of the brazed seam. It confirms the presence of a greater transformation barrier for B19′ phase transformation. R phase transformation takes place predominantly on the interface of NiTi and eutectic region (brazed seam metal) during crystallization. A separate Nb-based phase largely promotes formation of an elastic deformation field. Thus, a high fraction of R-phase transformation is induced in this region.

The authors of [30] lay a metallurgical basis for a reliable method of joining NiTi shape-memory alloys and superelastic alloys. It is based on application of pure niobium as a depressant, which causes contact melting with NiTi at acceptable temperatures. Butt specimens were brazed by pure niobium at 1180 °C for 6 min, cooled in the furnace and annealed at 350 °C for 90 min before testing. Brazed specimens failed at a pressure of a little less than 800 MPa, created by the impact of loading. The stress-strain curve for the joined butt specimens of superelastic NiTi plates (3 mm) shows that the brazing filler metal strength is equal to approximately 800 MPa [30]. This fact can have far-reaching consequences for NiTi application in complex aerospace structures, and it will allow expansion of NiTi application with various materials, including ceramics. It is shown that the quasibinary eutectic nature of equilibrium of NiTi–Nb system is the base for a reliable brazing technique, when joining NiTi sections with pure niobium application.

Alloys based on NiTiNb system are well-known as those with a wide hysteresis and with shape memory. They have important applications as joining materials. Proceeding from the existence of a quasibinary NiTi–Nb eutectic region in this ternary system, a new brazing method was developed to form metallurgical bonds between functional regions of nitinol [31]. When NiTi and pure Nb come into contact at a temperature above 1170 °C, spontaneous melting occurs, which leads to formation of a liquid phase which is extremely active. It not only wets the NiTi surface, but, obviously, dissolves the oxide precipitates, eliminating the need for fluxes, while ensuring an effective capillary flow into the joint gaps. The melting process is regulated by diffusion, and it is limited by Nb diffusion coefficient in the liquid phase. The brazing filler metal in the liquid state crystallizes at cooling with formation of a microstructure which contains predominantly ordered NiTi and disordered solid solution of niobium (BCC lattice). Mechanical testing showed that the brazed joints are strong, ductile and biocompatible with the human body. At appropriate aging after brazing, the functional characteristics of NiTi base alloy can be recovered. Microalloying of niobium filler metal by zirconium or tungsten showed a high potential for brazed seam strengthening. For applications, where biocompatibility is not a problem, niobium can be replaced by pure vanadium as the brazing filler, which has sufficient rupture strength and can potentially be superior to the analogs with niobium [31].

Of particular importance are dissimilar joints designed for medical applications [32]. Successful joining of dissimilar metal tubes will allow selective application of unique biocompatible materials, such as stainless steel and shape-memory materials (NiTi) for locally providing certain properties of medical devices — implants. Application of a new process of autogenous laser brazing, which uses the heat accumulation mechanism to produce joints of dissimilar tubular specimens (without brazing filler metal) from nitinol and stainless steel (1 mm diameter) ensures the appropriate strength, composition and microstructure. The influence of laser parameters on the thermal profile and joining mechanism is studied experimentally and by numerical modeling. The joint strength obtained

using this process reaches 500 MPa [32] that is close to the stresses of phase transformation of NiTi base material, as well as to rupture strength of tempered stainless steel. It is shown that this process is promising for application, but it requires additional studies as regards the particular tubular parts.

CONCLUSIONS

Analysis of published sources shows the relevance and importance of studies, related to producing permanent joints of nitinol — a promising shape-memory material, which needs to be joined in structure fabrication in different industries, including aerospace, medical sectors, etc.

Features of different methods of joining this material were high-lighted, and temperature-time parameters of the process of brazing NiTi intermetallic alloy in a similar combination and in combination with other materials were revealed. It is shown that at brazing nitinol in the ambient atmosphere brazing filler metals based on Ag–Cu–Zn–Sn–Ni system and AgCl–KF–LiCl flux have proven themselves well, ensuring the maximum joint strength of ~ 300 MPa.

At vacuum brazing (10^{-3} Pa) by brazing filler metal of Ag–Cu system the strength is in the range of 360–600 MPa that is due to the overlap value. At the same time, note that the eutectic brazing filler metal based on Ag–Cu system is alloyed by titanium in order to improve base metal wetting.

When producing permanent dissimilar joints of nitinol with titanium alloys, the following brittle phases form in the brazed seam: Ti_2Ni, $(Cu_xNi_{1-x})_2Ti$, Cu_2Ti, Cu(Ti, V), which promote cracking on the interphase of brazing filler metal-reaction layer and along the central zone of Ti_2Ni intermetallic compound, impairing the joint quality. Their formation in the joint zone can be avoided using brazing filler metal of a certain composition or interlayers, which improve the nitinol brazed joint properties at vacuum brazing. It should be specially noted that vacuum brazing of NiTi using pure niobium leads to a high quality and strength of the joints (close to 800 MPa). More over, at brazing nitinol using brazing filler metals, the following materials are promising: Nb, NbZr1, Cu and AuCu65, which promote partially pseudoelastic behaviour of NiTi/NiTi brazed joint.

At the same time, it should be noted that the process of producing permanent joints by brazing requires performance of further systemic studies with application of up-to-date computational and experimental methods, which will allow preserving the main properties of shape-memory alloys and will ensure the appropriate service properties of brazed products.

REFERENCES

1. Paton, B.E., Kaleko, D.M., Shevchenko, V.P. et al. (2006) Weldability of shape-memory alloys of Ni–Ti system. *The Paton Welding J.*, **5**, 1–10.
2. Jani, J.M., Leary, M., Subic, A.R, Gibson, M.A. (2014) A review of shape memory alloy research, applications and opportunities. *Materials & Design*, **56**, 1078–1113.
3. Krasovsky, V.P. (2009) Study of capillary characteristics and melting of nickel-titanium alloy (NiTiNOL) with shape-memory effect. *Adgeziya Rozplaviv i Payanniya Materialiv*, **42**, 95–102 [in Ukrainian].
4. Akimov, O.V., Nuri, S.M. (2015) Alloys with shape-memory effect. History of emergence and development, physics of process of their unique properties. *Visnyk NTU KhPI, Series: New Solutions in Modern Technologies*, 1123(**14**), 42–49 [in Russian].
5. Tillmann, W., Eilers, A., Henning, T. (2021) Vacuum brazing and heat treatment of NiTi shape memory alloys. *IOP Conf. Series: Materials Sci. and Eng.*, 1147:012025. DOI: https://doi.org/10.1088/1757-899X/1147/1/012025
6. Razorenov,S.V., Garkushin, G.V., Kanel, G.I. et al. (2011) Behavior of nickel-titanium alloys with shape-memory effect under shock-wave loading conditions. *Fizika Tvyordogo Tela*, 53(**4**), 768–773 [in Russian].
7. Massalski, T.B. (1990) Binary alloy phase diagrams, American Society for Metals. (*Ohio: Metals Park: ASM International: CD*).
8. Blednova, Zh.M., Stepanenko, M.A. (2012) Role of alloys with shape-memory effect in modern mechanical engineering. Krasnodar, RF [in Russian].
9. Chau, E.T.F. (2007) *A comparative study of joining methods for a SMART aerospace application*: Eng. Dr. Thesis. Cranfield University, UK.
10. Senkevich, K.S. (2017) Prospects of producing and application of hybrid structures and composites of titanium alloys and nitinol: Review. *Izv. Vuzov. Poroshk. Metallurgiya i Funktsionalnye Pokrytiya*, **4**, 71–78 [in Russian].
11. Zoeram, A.S., Mousavi, A. (2014) Laser welding of Ti–6Al–4V to nitinol. *Mater. Design*, **61**, 185–190.
12. Akselsen, O.M. (2010) *Joining of shape memory alloys. Shape memory alloys.* SINTEF Materials and Chemistry, Ed. by C. Cismasin, InTech, Norway, 183–211.
13. Shiue, R.H., Wu, S.K. (2006) Infrared brazing of Ti50Ni50 shape memory alloy using gold-based braze alloys. *Gold Bull.*, **39**, 200–204.
14. Grummon, D.S., Shaw, J.A., Foltz, J. (2006) Fabrication of cellular shape memory alloy materials by reactive eutectic brazing using niobium. *Mater. Sci. Eng.*, **A 438–440**, 1113–1118.
15. Zhao, X.K., Tang, J.W., Lan, L. et al. (2009) Vacuum brazing of NiTi alloy by AgCu eutectic filler. *Mater. Sci. Technol.*, **25**, 1495–1497. DOI: https://doi.org/10.1179/174328409X405625
16. ASM Handbook: *Alloy Phase Diagrams*, **3**, 1992, ASM International, Metals Park, Ohio, USA.
17. Tang, W., Sandstrom, R., Miyazaki, S. (2000) Phase Equilibria in the Pseudobinary Ti0.5Ni0.5–Ti0.5Cu0.5 System. *J. of Phase Equilibria, Japan*, 21(**3**), 227–234.
18. Watanabe, T, Sonobe, H. (1992) Brazing of Ni–Ti type shape memory alloy. *Quarterly J. of the Japan Welding Society*, 10(**1**), 95–101.
19. Shiue, R.K., Wu, S.-K. (2005) Infrared brazing Ti50Ni50 and Ti–6Al–4V using the BAg-8 Braze alloy. *Mater. Transact.*, 46(**9**), 2057–2066.
20. Li, M.G., Sun, D.Q., Qiu, X.M. et al. (2006) Effects of laser brazing parameters on microstructure and properties of

TiNi shape memory alloy and stainless steel joint. *Mater. Sci. Eng. A*, 424(**1–2**), 17–22. DOI: https://doi.org/10.1016/j.msea.2006.01.054
21. Lin, C., Shiue, R.K., Wu, S.-K, Yang, T.-E. (2019) Infrared brazed joints of Ti50Ni50 shape memory alloy and Ti-15-3 alloy using two Ag-based fillers. *Materials*, **12**, 1603–1614. DOI: https://doi.org/10.3390/ma12101603
22. Qiu, X.M., Li, M.G., Sun, D.Q., Liu, W.H. (2006) Study on brazing of TiNi shape memory alloy with stainless steels. *J. Mater. Proc. Technol.*, **176**, 8–12.
23. Humpston, G., Jacobson, D.M. (2004) *Principles of Soldering*. ASM International® Materials Park, Ohio, USA.
24. Shiue, R.K., Wu, S.K., Chen, S.Y. (2003) Infrared brazing of TiAl intermetallic using BAg-8 braze alloy. *Acta Materialia*, **51**, 1991–2004.
25. Bewerse, C, Brinson, L.C., Dunand, D.C. (2015) Microstructure and mechanical properties of as-cast quasibinary NiTi–Nb eutectic alloy. *Mater. Sci. Eng. A*, **627**, 360–368.
26. Piao, M, Miyazaki, S, Otsuka, K., Nishida, N. (1992) Effects of Nb addition on the microstructure of Ti–Ni alloys. *Mater. Transact.*, **33**, 337–345.
27. Wang, Y., Cai, X.Q., Yang, Z.W. et al. (2017) Effects of Nb content in Ti–Ni–Nb brazing alloys on the microstructure and mechanical properties of Ti–22Al–25Nb alloy brazed joints. *J. Mater. Sci. Technol.*, **33**, 682–689.
28. Liu, S., Han, S., Wang, L. et al. (2019) Effects of Nb on the microstructure and compressive properties of an as-cast Ni-44Ti44Nb12 eutectic alloy, *Materials*, **12**, 4118.
29. Wang, L., Wang, C., Zhang, L.C. et al. (2016) *Phase transformation and deformation behavior of NiTi–Nb eutectic joined NiTi wires*. Scientific Reports. 6:23905. DOI: https://doi.org/10.1038/srep23905
30. Grummon, D.S., Low, K.-B. Foltz, J., Shaw, J. (2007) New method for brazing nitinol based on the quasibinary TiNi–Nb system. In: *Proc. of 48th Conf. on AIAA/ASME/ASCE/AHS/ASC Structures, Structural Dynamics, and Materials (Honolulu, Hawaii, 23–26 April 2007)*.
31. Low, K.B. (2009) *Reactive eutectic brazing of nitinol*: Ph.D. Thesis, Michigan State University, USA.
32. Satoh, G., Brandal, G., Naveed, S., Yao, Y.L. (2017) Laser autogenous brazing of biocompatible, dissimilar metals in tubular geometries *J. Manuf. Sci. Eng.*, 139(**4**), 041016, 1–16.

ORCID
S.V. Maksymova: 0000-0003-0158-5760,
B.V. Stefaniv: 0000-0002-7159-8762

CONFLICT OF INTEREST
The Authors declare no conflict of interest

CORRESPONDING AUTHOR
S.V. Maksymova
E.O. Paton Electric Welding Institute of the NASU
11 Kazymyr Malevych Str., 03150, Kyiv, Ukraine.
E-mail: maksymova.svitlana15@ukr.net

SUGGESTED CITATION
S.V. Maksymova, B.V. Stefaniv (2022) Producing nitinol brazed joints (Review). *The Paton Welding J.*, **12**, 19–28.

JOURNAL HOME PAGE
https://patonpublishinghouse.com/eng/journals/tpwj

Received: 27.10.2022
Accepted: 30.01.2023

DOI: https://doi.org/10.37434/tpwj2022.12.04

INFLUENCE OF HEAT TREATMENT ON IMPROVEMENT OF MECHANICAL PROPERTIES OF WELDED JOINTS OF SPARSELY-DOPED TITANIUM ALLOY Ti–2.8Al–5.1Mo–4.9Fe

S.V. Akhonin, V.Yu. Bilous, V.A. Kostin, S.G. Hrygorenko, O.L. Puzrin, E.L. Vrzhyzhevskyi

E.O. Paton Electric Welding Institute of the NASU
11 Kazymyr Malevych Str., 03150, Kyiv, Ukraine

ABSTRACT

The most important advantage of pseudo-β-titanium alloys is their high strength, and the disadvantages include the high cost of alloying elements. Sparsely-doped alloys, such as LCB, Timetal 125, etc. were developed to lower the cost of titanium alloys based on β-phase. This class of titanium alloys is promising for application in inexpensive structures. Development of welding technology and modes of heat treatment of such alloy joints is an important task. In this work investigations were performed of the surface of fractures in welded joints of titanium alloy of Ti–2.8Al–5.1Mo–4.9Fe system, obtained after impact toughness testing. It was found that local heat treatment in the vacuum chamber of specimens of welded joints of test titanium alloy Ti–2.8Al–5.1Mo–4.9Fe produced by EBW by mode 4 (LHT in a vacuum chamber at the temperature of 750 °C for 5 min) allows producing higher ductility properties of welded joints, and preventing post-weld cold cracking. Such heat treatment leads to a more uniform arrangement of tough fracture areas on fracture surfaces.

KEYWORDS: titanium, pseudo-β-titanium alloys, sparsely-doped titanium alloys, welded joints, welding, electron beam welding, local heat treatment, tungsten electrode, heat treatment, mechanical properties, fracture surfaces, quality criterion

INTRODUCTION

Owing to its unique properties, sparsely-doped Ti–2.8Al–5.1Mo–4.9Fe titanium alloy is promising for application in different industries. Sparsely-doped titanium alloys are those which do not contain any expensive or deficit elements, such as niobium, vanadium, etc., and their alloying systems are based on such relatively inexpensive components as aluminium, iron, silicon, oxygen, etc. [1–4]. PWI performed work on producing ingots of Ti–2.8Al–5.1Mo–4.9Fe pseudo-β-alloy, using UE-208M electron beam unit with a cold hearth and portioned feed of liquid metal. Note that the produced ingots of Ti–2.8Al–5.1Mo–4.9Fe pseudo-β-alloy are close by their chemical composition to an alloy developed by TIMET Company, USA, which was named LCB (low cost beta) [5, 6].

High-strength sparsely-doped titanium alloys have been widely accepted in the aerospace sector (critical and highly-loaded components and assemblies); defense industry (armour protection elements of combat vehicles and personnel); transport engineering (engine components, wheel disks, springs, load-carrying structures of sports cars); in manufacture of smart goods for sports, medicine and consumer goods [7].

Improvement of mechanical properties of welded joints of sparsely-doped titanium alloys requires application of different methods of heat treatment or thermomechanical treatment (HT, TMT) [8].

In connection with the fact that application of full heat treatment of the whole welded product is not economically viable, local heat treatment (LHT) is as a rule used in the region of the titanium alloy joint. The main LHT objective consists in creation of the conditions to prevent cracking and other defects in the welded joint region, and in improvement of the mechanical properties in welding through application of local preheating up to certain temperatures and subsequent annealing, leading to relaxation of thermal stresses in the welding zone, as a result of the change of the metal structural and phase composition and producing the specified properties [9].

Electron beam and argon-arc welding are traditionally used for joining high-strength titanium alloys.

ARGON-ARC WELDING (AAW)

Tungsten electrode inert gas argon-arc welding (AAW) has been the most widely accepted for joining titanium alloys due to the fact that this welding process is the most inexpensive and versatile. It allows making joints in different positions in space, under the conditions of limited space and does not require any complicated readjustment of the equipment at the change of the welded product thickness or joint type. Welding can be performed both with application of filler metal and without it. Titanium alloy wires or rods are used as filler metal. Inert gas argon practically does not enter into chemical interaction with molten metal and other gases in the arc burning zone. Argon is heavier than air, so that it drives air out of the welding zone and reliably protects the liquid weld pool and near-weld zone of the welded joint from contact with the atmosphere.

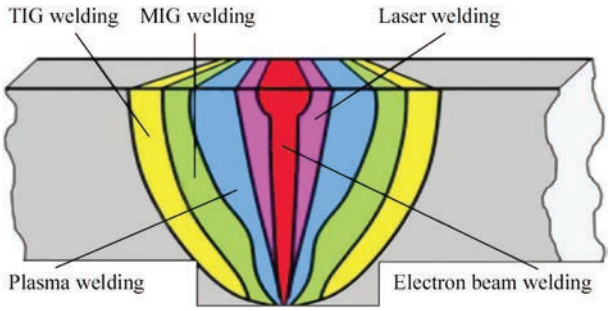

Figure 1. Comparison of weld dimensions for different kinds of welding

ELECTRON BEAM WELDING (EBW)

is welding, at which heating and melting of the contacting surfaces is performed by high-speed electron flows, moving in vacuum under the impact of the electric field. Welding is performed in the chamber in a vacuum, obtained by pumping down the air to a pressure of the order of 10^{-3} to 10^{-4} Pa. The electron beam is formed in a special assembly of the electron beam gun.

EBW features a high power density, being inferior only to laser welding as to this value, but it is greatly superior to electric arc welding. More over, EBW is characterized by minimal area of the heating spot. Figure 1 schematically shows the welding zone dimensions for different kinds of welding.

A significant advantage of EBW is complete degassing of the working area, which results in achievement of high-quality joining of chemically active metals. Absence of the influence of atmospheric oxygen and hydrogen on the weld metal allows achieving its more homogeneous and dense structure, as well as avoiding further corrosion.

The main disadvantage of EBW is the high cost of creating vacuum for welding highly active metals and alloys. That is why this welding method works in a narrowly specialized range of tasks for welding titanium alloys, high-technology expensive parts from these alloys, while meeting high requirements on tolerance and quality of the surface.

The objective of the work is determination of optimal modes of heat treatment of welded joints of sparsely-doped pseudo-β-titanium alloy of Ti–2.8Al–5.1Mo–4.9Fe system, made by electron beam and tungsten electrode argon-arc welding.

MATERIAL AND INVESTIGATION PROCEDURE

Welded joints of test sparsely-doped Ti–2.8Al–5.1Mo–4.9Fe titanium alloy were studied in the work. Multipurpose laboratory UE-208M electron beam unit was used for making the titanium alloy ingots [8]. Ingots of a round cross-section of 110 mm diameter were produced by the technology of cold-hearth electron beam melting (CHEBM) with portioned feed of liquid metal into a water-cooled crucible. Investigations of chemical composition of the produced ingots showed a uniform distribution of alloying elements along the ingot length. Plastic deformation of the billets was performed in a rolling mill of Skoda 355/500 model to the thickness of 10 and 6 mm by a standard procedure and they were annealed at the temperature of 750 °C. Table 1 shows the chemical composition of the studied titanium alloy.

Table 1. Chemical composition of sparsely-doped pseudo-β-titanium alloy [8]

Chemical composition, wt.%								
Al	Fe	Mo	Cr	Ni	Si	O	N	Ti (base)
2.78	4.87	5.13	0.03	0.02	≤0.003	0.08	0.02	89.48

Welding of this alloy was performed by two methods — EBW and AAW.

EBW of Ti–2.8Al–5.1Mo–4.9Fe alloy specimens 10 mm thick was performed in ELA 60/60 unit. Single-pass welding with through-thickness penetration was conducted in the following mode: accelerating voltage U_{ac} = 60 kV, beam current I_b = 80 mA, welding speed V_w = 7 mm/s. Temperature was controlled using thermocouples, fastened from the weld root side. To perform preheating before welding and local post-weld heat treatment directly in the chamber, the welded joints were heated by the electron beam, expanded into a rectangular scan. The width of the region heated at LHT, was determined so that it overlapped the weld and HAZ. In the work, the region width was 30 mm. Electron beam power during preheating and LHT was close to 3 kW that allowed ensuring the temperature on the level of 750 °C in the treated zone. The mode of welding with preheating and LHT is optimal from the viewpoint of cold cracking prevention and better weld formation.

Mode of AAW of Ti–2.8Al–5.1Mo–4.9Fe alloy specimens 6 mm thick was as follows: arc voltage U = 12 V, RPDC welding was performed by an automatic welding machine, welding current I = 350 A, welding speed v_w = 10 m/h, filler wire feed rate V_f = 30 m/h, arc voltage during welding was 12 V, shielding gas (argon) flow rate was 18 l/min in the nozzle and 22 l/min into the protective device for shielding the cooling weld metal. The weld reverse side was also shielded by argon from oxidation, using a copper forming backing. Figure 2 shows the general schematic of EBW (*a*) and AAW (*b*).

The filler metal used at AAW was 2 mm unalloyed titanium welding wire VT1-00zv. It allows varying the degree of weld metal alloying in a narrow range. The relative amount of filler metal in the weld metal was found by determining the penetration area of the joint metal in the transverse sections of the welds. During welding, the filler wire is fed into the pool head part. An oscillator device is connected in parallel to the power source for striking the arc. The os-

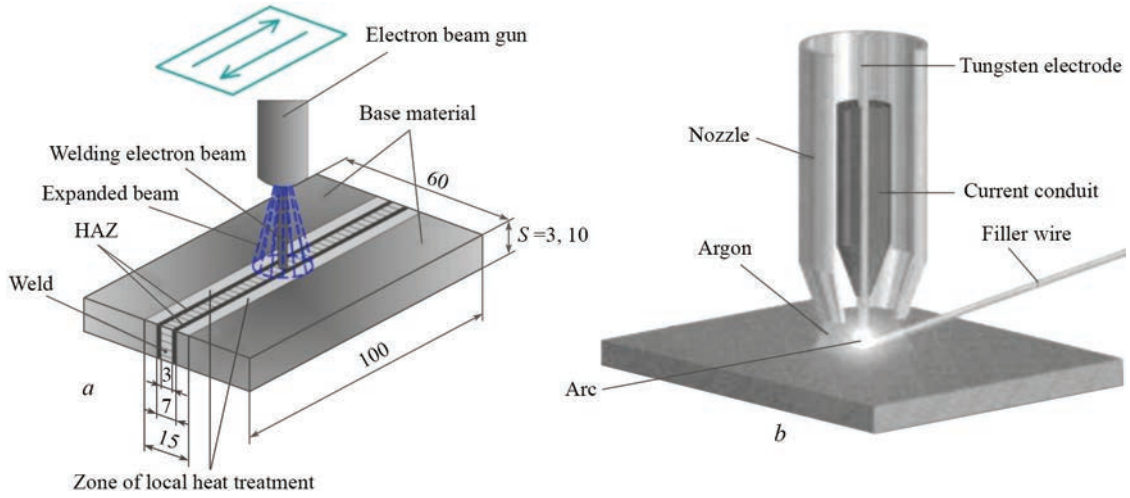

Figure 2. Schematic of welding sparsely-doped Ti–2.8Al–5.1Mo–4.9Fe titanium alloy: *a* — EBW; *b* — AAW

cillator applies high-frequency high-voltage pulses to the electrode, which ionize the arc gap and ensure arc striking after switching on the power source.

Application of the above welding methods is due to the features of the structures being welded and production capabilities.

In this work the fracture mechanism of welded joints of test sparsely-doped Ti–2.8Al–5.1Mo–4.9Fe pseudo-β-titanium alloy, produced by EBW and AAW was studied, also after the impact of different heat treatment modes (Table 2).

Mechanical properties of the studied specimens of base metal and welded joints are given in Table 3 [10].

INVESTIGATION RESULTS

In this work the fracture surfaces of welded joints of a titanium alloy of Ti–2.8Al–5.1Mo–4.9Fe system after impact toughness testing were investigated.

Figure 3 shows the test specimen fracture surfaces. Specimen analysis showed that for all the studied specimens fracture takes place by a mixed mechanism. The fracture surface is clearly defined and has a coarse-crystalline structure. The main crack propagated from the introduced stress raiser strictly in the direction of the applied load. Macroscopic analysis of the specimens showed the absence of shrinkage or "lips" of the cut that is indicative of small macroscopic plastic deformation at all the destruction stages [11]. At the same time, macroscopic analysis of the fracture mode showed that the plastic deformation fraction on the fracture surface essentially depends both on the welding type and on the heat treatment mode (Figure 3, *a*, *f*, *g*).

Microscopic study of fracture surface of specimens Nos 1–3 showed that it is heterogeneous and is characterized by a mixed pattern (Figure 4, *a*, *b*, *d*) [12]. Studies showed that the fracture surface is light-coloured,

Table 2. Modes of heat treatment of sparsely-doped titanium alloy of Ti–2.8Al–5.1Mo–4.9Fe system

Specimen number	Specimen type	Heat treatment
1	Base metal	–
2	EB welded joint (non-heat-treated)	–
3	EB welded joint with preheating up to 400 °C	–
4	EB welded joint with preheating up to 400 °C	LHT at 750 °C for 5 min
5	EB welded joint	Heating up to 760 °C, slow cooling at the rate of 1 °C/min
6	EB welded joint	Heating up to 760 °C, quenching into water, aging at 400 °C for 10 h
7	AAW joint made with VT1-00zv filler wire	Heating up to 760 °C, slow cooling at the rate of 1 °C/min

Table 3. Mechanical properties of welded joints of sparsely-doped titanium alloy of Ti–2.8Al–5.1Mo–4.9Fe system

Specimen number	Ultimate strength σ_t, MPa	Yield limit σ_y	Relative elongation δ, %	Reduction in area ψ, %	Impact toughness *KCV*, J/cm^2
1	1015	939	1.9	–	3.6
2	960	921	3.8	–	6.4
3	992	959	5.1	–	3.6
4	997	964	6.5	–	5.4
5	964	905	4.7	12.6	7.1
6	1204	1199	8.6	1.7	4.2
7	958	958	1.3	2.4	6.5

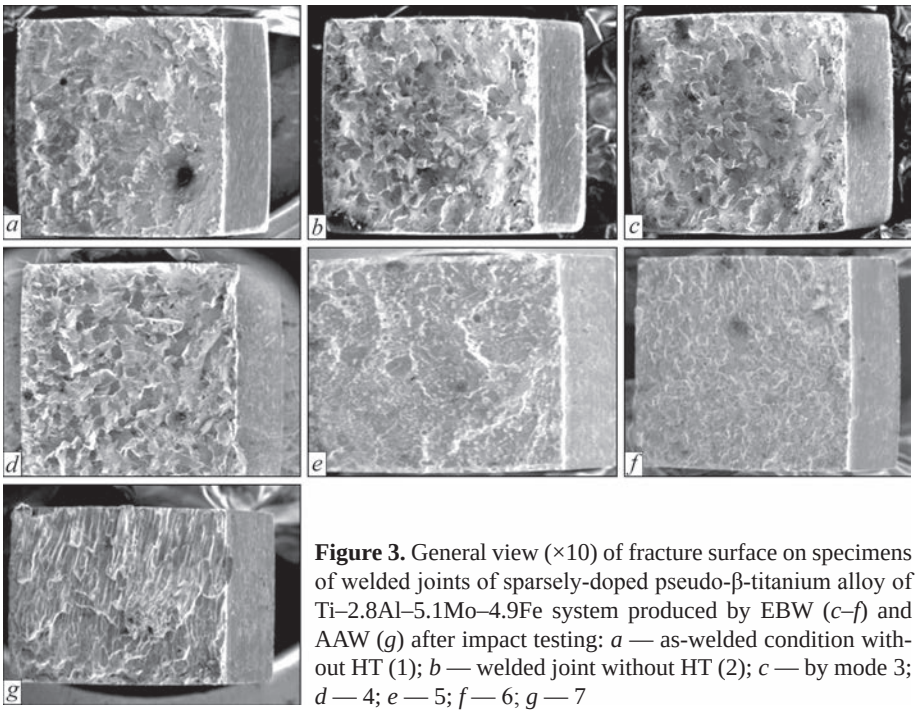

Figure 3. General view (×10) of fracture surface on specimens of welded joints of sparsely-doped pseudo-β-titanium alloy of Ti–2.8Al–5.1Mo–4.9Fe system produced by EBW (*c–f*) and AAW (*g*) after impact testing: *a* — as-welded condition without HT (1); *b* — welded joint without HT (2); *c* — by mode 3; *d* — 4; *e* — 5; *f* — 6; *g* — 7

coarse-crystalline, and developed. The fracture surface contains cleavage facets, which alternate with regions of intergranular and tough fracture. Cleavage facets separated by tearing regions, are observed. Specimens differ by the size of destruction facets (from 50 to 200 μm) and fraction of the tough component in the fracture (from 5 to 30 %). In specimens Nos 4–6 (Figure 3, *b, d, e, f*) the fracture surface is flat, and weakly-pronounced, that is indicative of a low rate of crack propagation which forms under the conditions of plane strain state. The fracture mode is predominantly brittle, tough component fracture is not higher than 20–25 %. The fracture surface of specimens Nos 6, 7 contains a series of parallel crystallographic surfaces in the form of steps (Figure 4, *f, g*).

A detailed analysis of fracture surface on specimens of welded joints of sparsely-doped Ti–2.8Al–5.1Mo–4.9Fe pseudo-β-titanium alloy showed that the details of fracture surface relief simultaneously contain both the cleavage facets and pits, which formed by the micropore coagulation mechanism (Figure 4, *b, f, g*). Tear ridges and river patterns are visible on the cleavage facets. Tough fracture elements were also found on fracture surfaces of specimens produced by modes 4, 5, and 6. This is indicative of the fact that after the appropriate heat treatment the material becomes more ductile (Figure 4, *d, f*).

Comparison of fracture mode of specimens after application of the appropriate heat treatment modes, performed by EBW and AAW showed (Figure 4, *f, g*) that

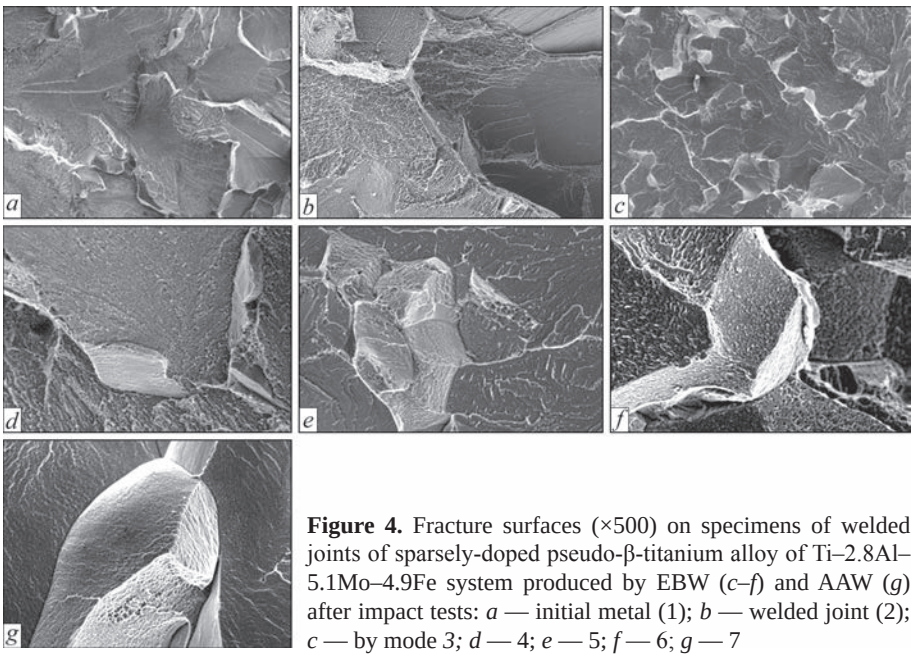

Figure 4. Fracture surfaces (×500) on specimens of welded joints of sparsely-doped pseudo-β-titanium alloy of Ti–2.8Al–5.1Mo–4.9Fe system produced by EBW (*c–f*) and AAW (*g*) after impact tests: *a* — initial metal (1); *b* — welded joint (2); *c* — by mode *3; d* — 4; *e* — 5; *f* — 6; *g* — 7

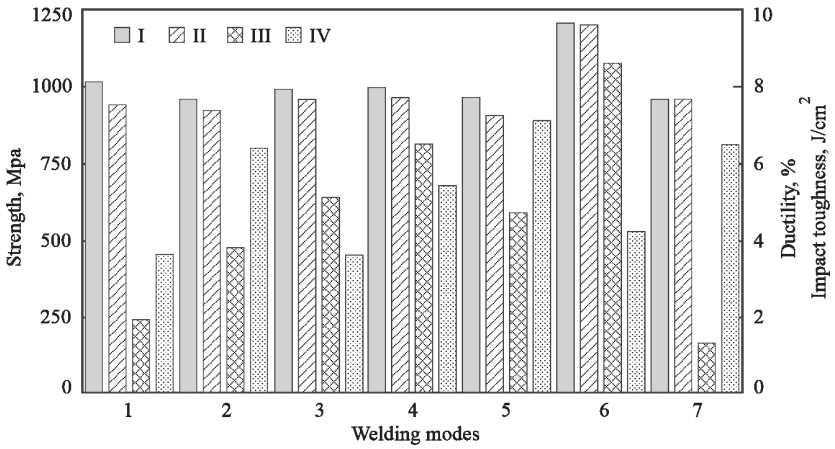

Figure 5. Influence of heat treatment modes on strength and ductility values of Ti–2.8Al–5.1Mo–4.9Fe titanium alloy (I — ultimate strength; II — yield point; III — reduction in area; IV — impact toughness)

specimens after EBW are more ductile and have a greater fraction of the tough component in the fracture.

Analysis of the results of mechanical testing of the studied sparsely-doped Ti–2.8Al–5.1Mo–4.9Fe titanium alloy after heat treatment by different modes (Table 3) showed that heat treatment of this alloy allows changing its mechanical properties in a rather broad parameter range. So, for EB welded joints in the heat-treated condition the highest ultimate strength of test Ti–2.8Al–5.1Mo–4.9Fe titanium alloy was achieved in mode 6 (quenching at the temperature of 760 °C + cooling into water + aging at 400 °C) — 1204 MPa, and the lowest value of 964 MPa was produced in mode 5 (slow cooling from the temperature of 760 °C at the rate of 1 °C/min). That is, appropriate heat treatment allows achieving properties both higher (mode 6) and lower (mode 5) that those of a non-heat-treated welded joint (mode 2, 960 MPa). Respective results were obtained also for the yield limit: the highest values were produced in mode 6 — 1199 MPa, and the lowest values were obtained in mode 5 — 905 MPa.

The ductility values (relative elongation and reduction in area) in the test Ti–2.8Al–5.1Mo–4.9Fe titanium alloy remains low after heat treatment. Maximum relative elongation was achieved in specimens after heat treatment by mode 6 — 8.6 % (126 % higher), and the lowest value was obtained in mode 7 — just 1.3 % (66 % lower). The specimen heat treated by mode 5, had the greatest reduction in area of 12.6 % (92 % greater) at respective elongation (4.7 %) (Figure 5).

Impact toughness of the studied specimens was not high, varying from 4.2 (mode 6) to 7.1 J/cm^2 (mode 5), the studied heat treatment modes changing it only slightly. The cause for the low values of impact toughness and ductility can be iron content in the test alloy — almost 5 % (see Table 1) that leads to formation of particles of titanium-iron intermetallic during production, which have a negative impact on the level of impact toughness of the test Ti–2.8Al–5.1Mo–4.9Fe titanium alloy [11].

In order to select the optimal mode of heat treatment of test Ti–2.8Al–5.1Mo–4.9Fe titanium alloy, a criterion of heat treatment "quality" in conditional units was proposed. It consists of the contribution of heat treatment modes into the comprehensive increase (or lowering) of total values of strength, ductility and impact toughness of the new titanium alloy relative to a non-heat-treated specimen (specimen 2) (Figure 6). That is, increase of some mechanical properties, for instance, strength, usually causes the respective lowering of ductility. In certain cases, however, it is disproportionate. In this connection, the "quality" criterion was proposed:

$$K_{ht} = \Sigma \frac{(P_{in} - P_{ht})}{P_{in}},$$

where K_{ht} is the "quality" criterion; P_{in} is the initial parameter (ultimate strength, yield limit, relative elongation, impact toughness) of a non-heat-treated specimen; P_{ht} is the heat-treated specimen parameter.

Positive values of K_{ht} parameter determine a comprehensive increase of the properties, and negative ones determine their lowering.

Analysis of the produced results shows that a comprehensive increase of welded joint properties at EBW can be achieved using mode 5. At application of heat treatment at AAW (mode 7) it is impossible to

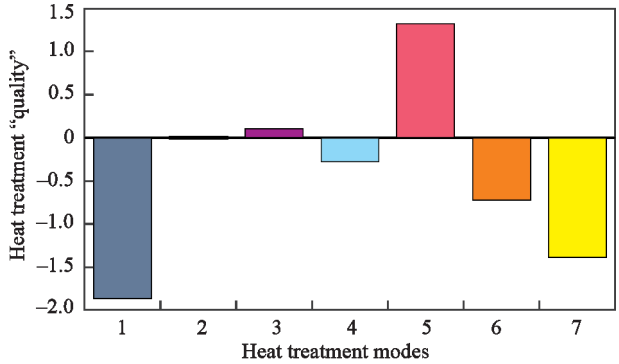

Figure 6. Influence of heat treatment modes on heat treatment "quality"

achieve an optimal combination of strength, ductility and impact toughness.

Use of the same heat treatment modes: heating up to 760 °C and subsequent slow cooling at the rate of 1 °C/min (modes 5 and 7) for welded joints made by two different kinds of welding, namely EBW and AAW, showed that the mechanical properties differ slightly: ultimate strength was 964 MPa (EBW) against 958 MPa (AAW), respectively.

Impact toughness values of specimens with a sharp notch for the two heat-treated specimens also changes only slightly from 7.1 J/cm^2 (EBW) against 6.5 J/cm^2 (AAW). The main difference after heat treatment is found in the ductility properties (relative elongation and reduction in area). Heat treatment of EBW specimens results in much better ductility properties (Table 3). This is attributable to the fact that the ductility properties in the heat-treated EBW specimens are higher due to increase of the tough component on the fracture surface (Figure 3, *f*, *g*). In EBW specimens the fracture contains 28 % of the tough component, and in AAW specimens it contains less than 15 %.

CONCLUSIONS

1. It is found that local heat treatment in a vacuum chamber of specimens of EB welded joints of test Ti–2.8Al–5.1Mo–4.9Fe titanium alloy by mode 4 (LHT in the vacuum chamber at the temperature of 750 °C for 5 min) allows producing higher ductility properties of welded joints and preventing cold cracking after welding. Such heat treatment leads to a more uniform arrangement of tough fracture regions on the fracture surface.

2. It is shown that application of heat treatment of specimens of Ti–2.8Al–5.1Mo–4.9Fe titanium alloy by mode 5 (heating up to 760 °C, slow cooling at the rate of 1 °C/min) allows producing an optimal complex of ductility (δ = 4.7 %, ψ = 12.6%) and impact (*KCV* = 7.1 J/cm^2) properties.

3. It is found that slow cooling after AAW also ensures an increase of ductility properties of welded joints of Ti–2.8Al–5.1Mo–4.9Fe titanium alloy, but they are lower than those at EBW with slow cooling, that is related to a higher cooling rate at AAW.

REFERENCES

1. Lütjering, G., Williams, J.C. (2003) *Titanium (engineering materials and processes)*. Berlin, Springer-Verlag, 3.
2. (2002) EHKTechnologies: *Opportunities for low cost titanium in reduced fuel consumption, improved emissions, and enhanced durability heavy-duty vehicles.* Subcontract 4000013062, EHKTechnologies, Vancouver, WA, USA.
3. Lavender, C.A. (2004) *Low-cost titanium evaluation*. Pacific Northwest National Laboratory, Richland, WA, USA.
4. (2004) EHKTechnologies: *Summary of emerging titanium cost reduction technologies. A study performed for US Department of Energy and Oak Ridge National Laboratory*. Subcontract 4000023694, EHKTechnologies, Vancouver, WA, USA.
5. Nochovnaya, N.A., Antashev, V.G. (2007) Titanium alloys of "LOW-COST" series and possibilities of their application. In: *Proc. of Int. Conf. on Ti-2007 in CIS (Kyiv, IMP)*, 191–192.
6. Bania, P.J. (1993) Beta titanium alloys and their role in the titanium industry. In: *Beta titanium alloys in the 90's*. TMS Publ., Warrendale, PA, 3–14.
7. Weiss, I., Semiatin, S.L. (1998) Thermomechanical processing of beta titanium alloys on overview. *Mat. Sci. Eng. A*, **243**, 46–65. DOI: https://doi.org/10.1016/S0921-5093(97)00783-1
8. Akhonin, S.V., Bilous, V.Yu., Berezos, V.O. et al. (2020) Structure and properties of structural sparcely-doped titanium-based alloys produced by EBM. *Suchasna Elektrometal.,* **4**, 7–15 [in Ukrainian]. DOI: https://doi.org/10.37434/sem2020.04.02
9. Akhonin, S.V., Belous, V.Yu., Selin, R.V. et al. (2018) Electron beam welding and heat treatment of welded joints of high-strength pseudo-β titanium alloy VT19. *The Paton Welding J.*, **7**, 10–14. DOI: http://dx.doi.org/10.15407/tpwj2018.07.02
10. Akhonin, S.V., Belous, V.Yu., Selin, R.V. et al. (2021) Influence of heat treatment on the structure and properties of welded joints of high-strength titanium alloys based on β-phase. *Suchasna Elektrometal.,* **4**, 51–58 [in Ukrainian]. DOI: https://doi.org/10.37434/sem202.04.11
11. Grigorenko, S.G., Taranova, T.G., Kostin, V.A. et al. (2021) Influence of heat treatment on the structure and fracture mode of welded joints of sparsely-alloyed titanium alloy. *Suchasna Elektrometal.,* **3**, 42–48 [in Ukrainian]. DOI: https://doi.org/10.37434/sem2021.03.07
12. Fellows, J. (1982) Fractography and atlas of fractograms. Ed. by M.L. Bernshtejn. Moscow, Metallurgiya [in Russian].

ORCID

S.V. Akhonin: 0000-0002-7746-2946,
V.Yu. Bilous: 0000-0002-0082-8030,
V.A. Kostin: 0000-0002-2677-4667,
S.G. Hrygorenko: 0000-0003-0625-7010,
E.L. Vrzhyzhevskyi: 0000-0001-8651-851

CONFLICT OF INTEREST

The Authors declare no conflict of interest

CORRESPONDING AUTHOR

S.V. Akhonin
E.O. Paton Electric Welding Institute of the NASU
11 Kazymyr Malevych Str., 03150, Kyiv, Ukraine.
E-mail: akhonin.sv@gmail.com

SUGGESTED CITATION

S.V. Akhonin, V.Yu. Bilous, V.A. Kostin, S.G. Hrygorenko, O.L. Puzrin, E.L. Vrzhyzhevskyi (2022) Influence of heat treatment on improvement of mechanical properties of welded joints of sparsely-doped titanium alloy Ti–2.8Al–5.1Mo–4.9Fe. *The Paton Welding J.*, **12**, 29–34.

JOURNAL HOME PAGE

https://patonpublishinghouse.com/eng/journals/tpwj

Received: 08.12.2022
Accepted: 30.01.2023

DOI: https://doi.org/10.37434/tpwj2022.12.05

CORROSION RESISTANCE OF PLASMA COATINGS BASED ON COMPOSITE POWDERS WITH FeAl INTERMETALLIC

N.V. Vihilianska[1], O.P. Gryshchenko[1], K.V. Iantsevych[1], Z.G. Ipatov[1], C. Senderowski[2]

[1]E.O. Paton Electric Welding Institute of the NASU
11 Kazymyr Malevych Str., 03150, Kyiv, Ukraine
[2]Warsaw University of Technology. Warsaw Polytechnic University.
Plac Politechniki 1, 00-661, Warsaw, Poland. E-mail: cezary.senderowski@uwm.edu.pl

ABSTRACT

The corrosion resistance of plasma coatings made of composite powders based on FeAl intermetallics in different corrosive environments was investigated. For deposition of coatings, powders based on FeAl intermetallics were used, which were produced by mechanochemical synthesis with the introduction of additional alloying elements of titanium and magnesium into their composition. Electrochemical tests of plasma coatings were performed by a potentiostatic method in a 3 % NaCl solution and in a 10 %` H_2SO_4 solution. It was revealed that the rate of the corrosion process of plasma coatings of the FeAl system depends on the nature of electrolyte and the mechanism of electrochemical process. Electrochemical studies of plasma coatings of the FeAl system showed that corrosion resistance in a 3 % NaCl solution is by an order higher than in a 10 % H_2SO_4 solution. It was found that introduction of alloying element of titanium to the composite coating based on FeAl intermetallics results in a 2–5 times increase in corrosion resistance of the coatings in a 10 % H_2SO_4 solution. It was shown that the plasma coatings based on FeAl intermetallics on a scale of corrosion resistance in a 3 % NaCl solution are in the "resistant" group. Electrochemical studies showed the ability of these protective coatings to operate in salty neutral solutions.

KEYWORDS: intermetallics, iron, aluminium, composite powder, plasma coatings, corrosion resistance

INTRODUCTION

Iron aluminides belong to the intermetallics that are the most studied and used in industry due to their properties, such as low specific weight, high wear and corrosion resistance, etc. [1]. In recent years, iron FeAl intermetallics have been widely used as materials of protective coatings due to high heat resistance (up to 600–700 °C) and corrosion resistance in different aggressive environments. The main advantage of these coatings is, first of all, the possibility of replacing expensive heat-strength and heat-resistant coatings based on nickel aluminide [2].

Studies in the field of thermal spraying of intermetallic FeAl-coatings have been considered in [3–8]. Most of the works are aimed at studying processes occurring in composite powders produced by the method of mechanical alloying or mechanochemical synthesis (MChS).

In [9–11] it was noted that FeAl-based coatings significantly increase the corrosion resistance of steel products during long tests in the solutions of a sulfuric acid and seawater. An additional increase in corrosion resistance of FeAl-based intermetallics is possible by introducing alloying elements, such as chromium, copper, etc. into their composition [12, 13]. Thus, the additional introduction of chromium into FeAl intermetallics reduces the corrosion current, accelerates the beginning of passivation in a 3.5 % NaCl solution. The introduction of 3–5 wt.% of copper to the composition of FeAl-coatings causes the formation of a dense passive film on the surface of the electrode, which allows 2–3 times increase in the corrosion resistance during long-term tests in a solution of sulfuric acid.

At the PWI for thermal spraying of protective coatings based on FeAl intermetallics, composite powders (CP) were developed and plasma spraying technology of protective coatings was mastered [14, 15].

The aim of this work was to study the corrosion resistance of plasma coatings based on FeAl intermetallics, the effect of alloying elements on corrosion resistance of coatings in different aggressive environments.

RESEARCH OBJECTS AND EXPERIMENT PROCEDURE

As starting materials for plasma spraying, composite powders based on FeAl intermetallics were used, produced by the method of mechanochemical synthesis [14] (Table 1).

The coatings with a thickness of 500 ± 50 μm were deposited on the specimens of St3 steel in the UPU-8M installation using the following modes: I = 600 A, U = 40 V, Q_{Ar+N_2} = 50 l/min, spraying distance is 80 mm.

The studies of electrochemical properties of plasma coatings were carried out by the potentiostatic method in the potentiostat P-5827M at a scanning rate of 2 mV/s at a temperature of 18–20 °C with the use of a clamping cell. The stationary potentials were

Table 1. Characteristics of MChS powders based on FeAl intermetallics

System	Composition, wt.%	Phase composition	Size of particles		
			D_{10}, μm	D_{50}, μm	D_{90}, μm
Fe_3Al	86Fe + 14Al	Fe_3Al	3.6	11.2	32.9
Fe–AlMg	86Fe + 14(Al5Mg)	Solid solution of Mg in Fe_3Al	2.8	14.5	29.8
Fe–TiAl	60.8Fe + 39.2(Ti37.5Al)	Solid solution of Al in FeTi ($Fe_{1-x}TiAl_x$)	2.6	8.7	29.7

measured relative to the chlorine silver electrode, platinum served as an auxiliary electrode. As an electrolyte for corrosion studies, a 3 % NaCl solution and a 10 % H_2SO_4 solution were selected. The selection of the mentioned acid was predetermined by its wide use in the chemical industry, the selection of salty solution — by its use in natural conditions. It is known that the presence of chlorine ions in the electrolyte (a strong depassivator) is very harmful to metals, the corrosion resistance of which is predetermined by the passive condition of its surface. Chlorine ions lead to local destructions of passive film that in turn can lead to pitting corrosion [16–18].

According to the experimental data, cathode and anode polarization curves were built in the coordinates $E_c = f(\lg i_c)$, where the E_c is the potential, V; i_c is the corrosion current, A/cm^2. From the polarization curves, using the graphic method, the corrosion current (i_c) and corrosion potential (E_c) were determined on the extrapolation of tafel tilts at cathode and anode curves until their mutual intersection. Using the values of corrosion currents determined from the polarization curves, the mass and deep corrosion indices of the coatings was calculated by the following formulas:

$$K_w \frac{iA \cdot 1000}{nF}, \quad (1)$$

where K_w is the weight corrosion index (g/m^2·h); A is the atomic weight of metal (iron); n is the valence of the metal ion, which has passed into the solution (Fe^{2+}, $n = 2$); i is the current density (A/cm^2); F is the Faraday constant, 26.8 A·h/mol.

$$K_i \frac{8.76}{\rho}, \quad (2)$$

where K_i is a deep corrosion index, (mm/year); K_m is the mass corrosion index (g/m^{2}h); ρ is the metal density, g/cm^3; 8.76 is the coefficient for the transition from mass corrosion index K_m to deep corrosion index K_i up to one year, calculated from the number of hours per year (24 h·365 = 8760 h) and divided into 1000.

For comparative characteristics of corrosion resistance, a ten-point scale evaluation was used based on the deep corrosion index (K_i) [16, 18].

RESULTS OF THE EXPERIMENT AND THEIR DISCUSSION

Examinations of microstructure (Figure 1) of the sprayed plasma coatings indicate that in the coatings based on FeAl intermetallics, a dense lamellar structure is formed; the porosity of the coatings does not exceed 7 %.

According to X-ray structural phase analysis [15], the plasma coating of the Fe_3A1 system consists of intermetallic Fe_3A1 and FeAl phases and contains traces of $A1_2O_3$ oxide; the coating of the Fe–AlMg system consists of a solid Al solution in α-Fe and complex $MgA1_2O_4$ and $MgFeAlO_4$ oxides; the coating of the Fe–TiA1 system in addition to the main Fe_3Al phase contains iron Fe_2O_3, Fe_3O_4 and FeO oxides, iron and FeTi phase.

The studies of the kinetics of electrode potentials of plasma FeAl-coatings allowed establishing that the value of the electrode potential will stabilize within 40–60 min during immersion of specimens with coatings in it. The measurements of stationary potentials

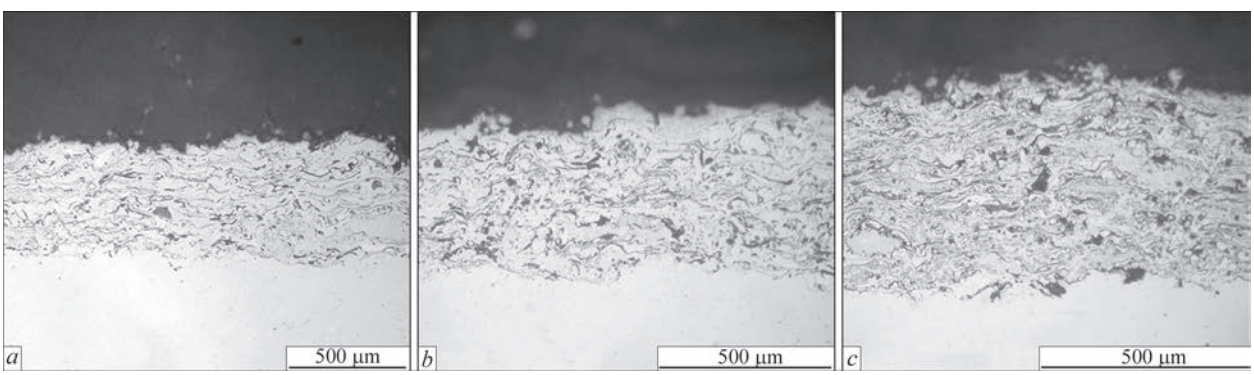

Figure 1. Microstructure of plasma coatings of the FeAl system: *a* — Fe_3Al; *b* — Fe–AlMg; *c* — Fe–TiAl

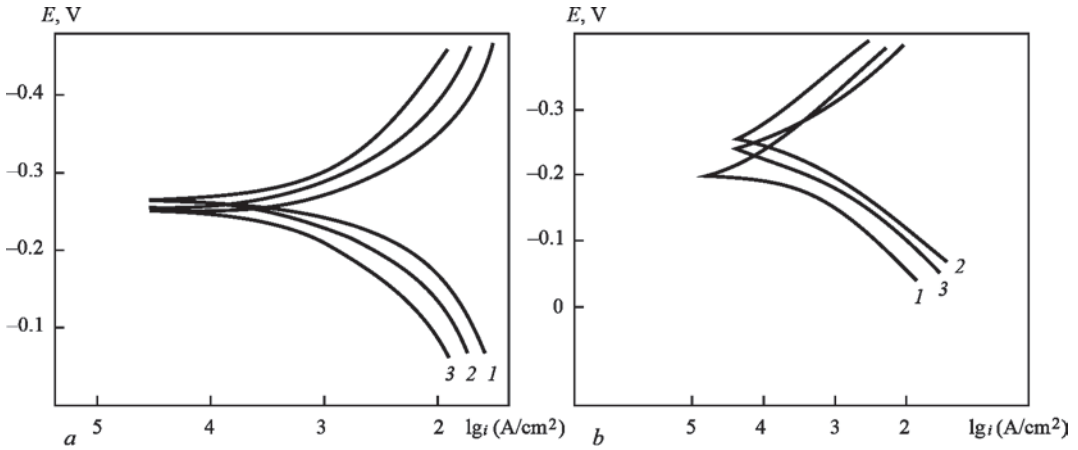

Figure 2. Polarization curves of plasma coatings of the FeAl system: *a* — in a 3 % NaCl solution; b - in a 10 % H_2SO_4 solution (*1* — Fe_3Al; *2* — Fe–AlMg; *3* — Fe–TiAl)

E_{st} of the specimens with plasma FeAl-coatings in the absence of current in an electrochemical system showed that regardless of the coatings composition in a 10 % H_2SO_4 solution and in a 3 % NaCl solution, the values of E_{st} amount to 0.34 and 0.32 V, accordingly.

The studies of electrochemical behaviour of the plasma FeAl-coatings have shown that at anode polarization on the polarization curves in a 3 % NaCl solution in the active region, the current depends linearly on the potential on the areas from –0.32 to –0.22 V and in a 10 % H_2SO_4 solution — from –0.34 to –0.2 V, and at the further increase in the potential, the saturation current is achieved and the current remains almost constant with an increase in potential, the areas of the passive state on the polarization curves are absent (Figure 2).

Deposition of plasma coatings of the FeAl system on St3 inhibits the corrosion process in a 3 % NaCl solution by a one order and in a 10 % H_2SO_4 solution — by two orders (see Figure 2). A different rate of the corrosion process is associated with different nature of anions (SO_4^{2-}, Cl^-) and pH value.

It is known that the nature of anions (SO_4^{2-}, Cl^-), which are present in the solution, significantly affects the anode dissolution and the rate of corrosion process [16, 17]. In the solution of a sulfuric acid, the corrosion process proceeds on electrochemical mechanism with hydrogen depolarization, according to which in the cathode areas $2H^+ + 2e \rightarrow H_2$ reaction occurs. The rate of the corrosion process of the plasma coatings of the FeAl system in the solution of a sulfuric acid (pH 1–2) is associated with a high activity of iron as the main component of the coating, which transfers into the solution in the form of Fe^{2+}. In the neutral medium, to which a 3 % NaCl solution (pH 7.0–7.5) corresponds, the corrosion process for the coatings proceeds on electrochemical mechanism with oxygen depolarization. In a 3 % NaCl solution, the rate corrosion process for coatings is inhibited due to the formation of a dense oxide Al^{3+} film, which inhibits the transition of iron to the solution [17].

The comparison of corrosion currents in the plasma coatings of the FeAl system (Table 2) determined by the method of extrapolation of tafel areas of polarization curves also showed that a corrosion current in a 3 % NaCl solution is by an order of value higher ($i_c = 10^{-6}$ A/cm^2) than in a 10 % H_2SO_4 solution ($i_c = 10^{-5}$ A/cm^2).

The carried out electrochemical tests indicated that introduction of alloying elements (Mg, Ti) into the FeAl system affects the corrosion resistance in the selected electrolytes in a different way. Electrochemical tests in a 3 % NaCl solution showed that when magnesium is introduced into the FeAl system, a slight shift in the corrosion potential into a negative value, inhibition of cathode reaction and acceleration of

Table 2. Results of electrochemical studies of plasma coatings based on FeAl

Number	Composition of coatings	Electrolyte					
		3 % NaCl			10 % H_2SO_4		
		E_{st}, V	E_c, V	i_c, A/cm^2	E_{st}, V	E_c, V	i_c, A/cm^2
1	Fe_3Al	–0.32	–0.28	$2.5 \cdot 10^{-6}$	–0.34	–0.26	$1.5 \cdot 10^{-5}$
2	Fe–AlMg	–0.34	–0.3	$3.5 \cdot 10^{-6}$	–0.28	–0.24	$3.3 \cdot 10^{-5}$
3	Fe–TiAl	–0.3	–0.28	$1.1 \cdot 10^{-6}$	–0.22	–0.18	$8.9 \cdot 10^{-6}$
4	Ст3	–0.54	–0.56	$6.5 \cdot 10^{-5}$	–0.28	–0.3	$2.5 \cdot 10^{-4}$

Table 3. Indices of corrosion resistance of plasma coatings based on FeAl

Number	Composition of coatings	Electrolyte			
		3 % NaCl		10 % H_2SO_4	
		K_m, g/m²·year	K_i, mm/year	K_m, g/m²·year	K_i, mm/year
1	Fe_3Al	0.05	0.056	0.13	0.14
2	Fe–AlMg	0.06	0.073	0.27	0.31
3	Fe–TiAl	0.042	0.046	0.061	0.06
4	St3	–	0.5935	–	0.3222

anode dissolution occur; corrosion current increases slightly (from $2.5 \cdot 10^{-6}$ to $3.5 \cdot 10^{-6}$ A/cm²) occurs. In a 10 % H_2SO_4 solution, the introduction of magnesium into the coatings increases the corrosion current (from $1.5 \cdot 10^{-5}$ to $3.3 \cdot 10^{-5}$ A/cm²), accelerates both cathode and anode reaction. A decrease in the protective properties of plasma FeAlMg coatings by 1.5–2.0 times (Table 3) is probably associated with the occurrence of a galvanic Fe–Mg couple and intensive dissolution of magnesium on the surface of the electrode in the process of corrosion studies.

Electrochemical studies of coatings in a 3 % NaCl solution and in a 10 % H_2SO_4 solution showed that alloying of FeAl intermetallics with titanium shifts the corrosion potential towards more positive values, inhibits the cathode process, reduces the corrosion current to $1.1 \cdot 10^{-6}$ A/cm² and $8.9 \cdot 10^{-6}$ A/cm², respectively. The corrosion resistance in a NaCl solution increases by 1.2–1.6 times and in a H_2SO_4 solution — by 2–5 times (Table 3). An increase in the corrosion resistance is probably related to the formation of FeTi phase in the coatings and a possible formation of the oxide film with TiO_2 composition on the surface of the electrode.

The values of corrosion currents found from the polarization curves allowed calculating the weight and deep corrosion index of the coatings (Table 3).

Corrosion tests have shown, that plasma coatings based on FeAl intermetallics, deposited on St3 in a 3 % NaCl solution and in a 10 % H_2SO_4 solution inhibit the corrosion process by 8–13 times and by 2–5 times, accordingly.

According to the used ten-point scale evaluation of corrosion resistance, the plasma coatings of the Fe_3Al, Fe–Al and Fe–TiA1 systems in a 3 % NaCl solution and the Fe–TiA1 system in a 10 % H_2SO_4 solution can be attributed to the "resistant" group and in a 10 % H_2SO_4 solution — the coatings Fe_3A1 and Fe–AlMg belong to the group of a "decreased resistance".

CONCLUSIONS

1. The conducted electrochemical studies have shown that the corrosion resistance of the plasma FeAl-based coatings depends on the composition of the electrolyte and pH value. In a neutral environment (3 % NaCl solution, pH 7.0–7,5), the corrosion resistance is by an order higher than in an acidic environment (10 % H_2SO_4 solution, pH 1–2), which is predetermined by different effects of SO_4^{2-} i Cl^- anions on the anode dissolution of coatings.

2. The introduction of alloying elements into the plasma coatings based on FeAl intermetallics showed that introduction of magnesium slightly reduces the protective properties of the plasma coatings in the studied electrolytes by 1.2–1.6 times, which is associated with the occurrence of a galvanic Fe–Mg couple on the surface of the electrode. The introduction of the alloying element of titanium to the composition of FeAl increases the corrosion resistance of the coatings in a 10 % H_2SO_4 solution by 2–5 times.

3. Plasma coatings based on FeAl intermetallics increase the corrosion resistance of carbon St3 steel by 8–13 times in a 3 % NaCl solution and by 2–5 times in a 10 % H_2SO_4 solution.

REFERENCES

1. Zamanzade, M., Barnoush, A., Motz, C. (2016) A Review on the properties of iron aluminide intermetallics. *Crystals*, 6(**1**), 10.
2. Palm, M., Stein, F., Dehm, G. (2019) Iron aluminides. *Annual Review of Mater. Research*, **49**, 297–326.
3. Yang, D.,Tian, B., Cao, Y. (2011) Microstructures and properties of FeAl coatings prepared by LPPS, APS and HVOF. In: *Proc. of ITSC'2011*, 1229–1234.
4. Oliker, V.E., Yakovleva, M.S. (2013) Intermetallics of Fe–Al system: Methods of producing, properties, coatings. *Materialovedenie,* **3**, 46–53 [in Russian].
5. Grosdidier, T., Ji Gang, Bernard F. et al. (2006) Synthesis of FeAl nanostructured materials by HVOF spray forming and spark plasma sintering, *Intermetallics*, **14**, 1208–1213.
6. Totemeier, T.C., Swank, W.D. (2002) Microstructure and stresses in HVOF sprayed iron aluminide coatings. *J. of Thermal Spray Technol.*, 11(**3**), 2–9.
7. Gang, Ji, Grosdidier, T., Liao, H. et al. (2005) Spray forming thick nanostructured and microstructured FeAl deposits. *Intermetallics*, **13**, 596–607.
8. Senderowski, C., Bojar, Z. (2008) Cas detonation spray forming of Fe–Al coatings in the presence of interlayer. *Surf. & Coat. Technol.*, **202**, 3538–3548.
9. Ning-Ning, Li, Min-Zhi, Wang, Yong-Sheng, Li, Guang Chen, Pei Li. (2016) Corrosion behavior of Fe–Al coatings fabricated by pack aluminizing method. *Acta Metallurgica Sinica*, 29(**9**), 813–819.
10. Xiao-Lin, Z., Zheng-Jun, Y., Xue-Dong, G. et al. (2009) Microstructure and corrosion resistance of Fe–Al intermetallic coating on 45 steel synthesized by double glow plasma sur-

face alloying technology. *Transact. of Nonferrous Metals Society of China*, 9(**1**), 143–148.
11. *Maricruz* Hernandez, H.B., Liu, J., Alvarez-Ramirez, M., Espinosa-Medina, A. (2017) Corrosion behavior of Fe–40 at.% Al–based intermetallic in 0.25 M H_2SO_4 solution. *J. of Materials Eng. and Performance*, 26(**16**), 1–14.
12. *Vijaya* Lakshmi, D., Suresh Babu, P., Rama Krishna, L., Vijay, R. (2021) Corrosion and erosion behavior of iron aluminide (FeAl(Cr)) coating deposited by detonation spray technique. *Advanced Powder Technology*, 32(**7**), 2192–2201.
13. Tomaru, M., Yakou, T. (2011) Influence of additional element Ni and Cu on corrosion resistance of FeAl in HCl solution. *J. of the Surface Finishing Society of Japan*, 62(**9**), 457–462.
14. Borisov, Yu.S., Borisova, A.L., Burlachenko, A.N. et al. (2017) Structure and properties of alloyed powders based on Fe_3Al intermetallic for thermal spraying produced using mechanochemical synthesis method. *The Paton Welding J.*, **9**, 33–39. DOI: https://doi.org/10.15407/tpwj2017.09.06
15. Borisov, Yu.S., Borisova, A.L., Vigilianska, N.V. et al. (2020) Coatings based on Fe–Al intermetallics produced by the methods of plasma and supersonic plasma gas-air spraying. *The Paton Welding J.,* **7**, 29–37. DOI: https://doi.org/10.37434/tpwj2020.07.04
16. Alimov, V.I., Duryagina, Z.A. (2012) *Corrosion and corrosion protection of metals*. Donetsk-Lviv, TOV Skhidnyi Vydavnychyi Dim [in Ukrainian].
17. Myronyuk, I.F., Mykytyn, I.M. (2016) *Electrochemistry and their practical aspects: Manual*. Ivano-Frankivsk, Prykarp. NU [in Ukrainian].
18. Pokhmurskyi, V.I., Homa, M.S. (2008) *Corrosion fatigue of metals and alloys*. Lviv, SPOLOM [in Ukrainian].

ORCID
N.V. Vihilianska: 0000-0001-8576-2095,
O.P. Gryshchenko: 0000-0003-2640-8656,
K.V. Iantsevych: 0000-0002-3975-7727,
Z.G. Ipatov: 0000-0003-2209-408X,
C. Senderowski: 0000-0002-0331-3702

CONFLICT OF INTEREST
The Authors declare no conflict of interest

CORRESPONDING AUTHOR
N.V. Vihilianska
E.O. Paton Electric Welding Institute of the NASU
11 Kazymyr Malevych Str., 03150, Kyiv, Ukraine.
E-mail: pewinataliya@gmail.com

SUGGESTED CITATION
N.V. Vihilianska, O.P. Gryshchenko, K.V. Iantsevych, Z.G. Ipatov, C. Senderowski (2022) Corrosion resistance of plasma coatings based on composite powders with FeAl intermetallics. *The Paton Welding J.*, **12**, 35–39.

JOURNAL HOME PAGE
https://patonpublishinghouse.com/eng/journals/tpwj

Received: 13.09.2022
Accepted: 30.01.2023

DOI: https://doi.org/10.37434/tpwj2022.12.06

STUDYING THE PROCESS OF PRODUCING FLUORPHLOGOPITE MELT IN ELECTRIC ARC FURNACE FOR THE PRODUCTION OF MASSIVE CORROSION-RESISTANT PRODUCTS FOR NONFERROUS METALLURGY

V.M. Korzhyk[1,2], **V.O. Shcheretskyi**[2,3], **A.G. Maliavin**[3], **Yi Jianglong**[1], **A.O. Alyoshyn**[4], **A.A. Alyoshyn**[4]

[1]China-Ukraine Institute of Welding, Guangdong Academy of Sciences, Guangdong Provincial Key Laboratory of Advanced Welding Technology Guangzhou, 510650, China
[2]E.O. Paton Electric Welding Institute of the NASU
11 Kazymyr Malevych Str., 03150, Kyiv, Ukraine
[3]Physico-Technological Institute of Metals and Alloys of the NASU
34/1 Vernadskyi Blvd., 03142, Kyiv, Ukraine
[4]"Foreign Trade office of the Chinese-Ukrainian E.O. Paton Institute of Welding" Ltd.
11 Kazymyr Malevych Str., 03150, Kyiv, Ukraine

ABSTRACT

The work reveals the issues of electric arc melting of nonmetallic systems, such as oxide melts, for synthesis and casting of fluorphlogopite products, which are used as corrosion-resistant hydro- and gas-tight products for conditions of elevated temperatures and aggressive effects of chlorine, ammonia, metal melts, etc. The advantages and disadvantages of arc melting furnaces with a water-cooled crucible and graphite lining in the preparation of fluorosilicate melts are revealed. The relation between melting parameters and furnace design and their effect on the structure and phase composition of fluorphlogopite casting was investigated. The rational temperature modes for producing fluorphlogopite melt were developed to minimize energy consumption and loss of volatile components from the melt. The effectiveness of using technological samples for express analysis of the fluorphlogopite casting quality is shown, which allows quickly correcting the charge composition by analyzing the technological sample fracture. Therefore, it is possible to control the melt quality and use a recycled material as charge materials in the amount of up to 50–60 % directly during melting. The proposed technological and design solutions allow producing fluorphlogopite melt in the amount sufficient for the production of massive castings over 150 kg.

KEYWORDS: electric arc melting; fluorphlogopite; stone casting; express analysis; technological samples

INTRODUCTION

Fluorphlogopite, which is produced by solidification of the melt, has the composition of natural phlogopite with the introduction of fluorine (corresponds to the formula $KMg_3(Si_3A1O_{10})F_2$), is characterized by a unique combination of physicochemical properties, which is not inherent in refractory and corrosion resistant materials used in the nonferrous metallurgy and chemical industry in chlorination and recovery processes. Fluorphlogopite material is characterized by the absence of polymorphic transformations and can be treated on metalworking equipment, the true density of cast fluorphlogopite is 2750 kg/m^3, its compressive strength is 69.90 MPa and bending strength is 10.25 MPa, thermal expansion coefficient (0–950 °C) is 7.6–8.2·10^{-6} deg^{-1}, specific volumetric electrical resistance (20 °C) is 2·10^{10}–4·10^{11} Ohm·m. Moreover, its dialectical properties are preserved both at elevated as well as at low temperatures to the level of cryogenic ones [1]. A significant advantage of cast products from conventional (sintered) refractory ones, which are produced by sintering of oxide components, is their dense cast structure without open porosity. In this case, fluorphlogopite casting as refractory compounds can operate at temperatures of 1000–1200 °C in the conditions of aggressive media for a long time and is resistant to thermal impacts. This is especially important for metallurgical and chemical furnaces operating in a constant contact with aggressive elements, such as chlorine in liquid, vapour or gaseous states. In the process of long-term operation of metallurgical chlorators and electrolyzers, the aggressive environment impregnates sintered refractory compounds, destroying a binding component, which eventually leads to the destruction of their integrity. Therefore, when using stone fluorphlogopite products in industry, it is necessary to create new furnaces, increase the service life and reduce material

and operational costs for maintenance and repair of equipment, which provides a significant economic effect [2]. However, the development of casting technology for massive products from such complex nonmetallic oxide systems requires taking into account the features resulted from the composition of mineral charge components and the properties of oxide melts. During melting of fluorphlogophite melt made of mineral charge materials, the formation of melt of the base mineral (fluorphlogopite) occurs directly in the furnace. Mineral components contain volatile components (fluorine), which can be produced from the melt in the form of gaseous compounds. In addition, the viscosity of aluminosilicate melt during the formation of fluorsilicate compounds changes greatly, which can lead to significant local overheating of the melt [1]. Therefore, melting of mineral charge components and production of fluorphlogopite melt is a more complex process as to heating conditions and melting modes as compared to melting of metal alloys.

According to gas analysis, the most volatile component of the melt is hydrogen fluoride (HF). The less volatile ones include alkalis (K, Na), whose increased evaporation in the form of fluorides is associated with their relatively high mobility in the melt [2]. The volatility of individual melt components (F, K) leads to deterioration of chemical uniformity of the melt, delamination and release of high-temperature crystalline minerals (phases).

A rational approach to the synthesis of fluorphlogopite material, which should possess a certain complex of properties, can only be carried out on the basis of studies of composition-structure-properties ratios, as well as studying the impact of melting parameters on the process of producing fluorphlogopite melt.

Technological properties of fluorphlogopite melt during the melting period before its pouring into casting moulds and in the process of transition from a liquid state to a solid one are important for producing high quality castings, as the process of structure formation, formation of shrinkage and gas cavities in the castings begins in the liquid state and ends in the period of crystallisation and solidification of the melt.

RESEARCH PROCEDURE AND RESULTS

To study the features of electric arc melting of fluorphlogopite material from mineral charge components, experimental and industrial-research melts in the conditions of recovery atmosphere in flux-melting electroslag furnaces were conducted [3]. As to the design, electric arc furnaces in which the melts were carried out, are composed of a water-cooled metal or crucibles lined with graphite, electrical holder and a column with an electromechanical drive for movement of the electrode. A moving graphite electrode is switched in the electrical circuit of the power transformer in series according to the electrode-bottom plate circuit.

The choice of a melting furnace (electric arc furnace) was determined by the features of the developed technology of manufacturing fluorphlogophite casts, which involves a periodic production of a certain amount of fluorphlogopite melt with a set chemical composition, temperature and viscosity.

The basic parameters of operating mode in melting furnaces — temperature and time are closely dependent on each other. The higher the melting temperature, the less time it takes to prepare fluorphlogopite melt. On the other hand, an increase in temperature is limited by the volatility of charge components, which requires the development of the optimum temperature mode for the melt preparation. This factor is significantly reflected in the rational choice of the required temperature mode of melting, in which the production of a high quality melt is combined with the possibility of preparing it in a set time.

The experimental melts were carried out on the research and production facilities of the PTIMA of the NASU in the flux melting furnace with a single-phase transformer of type TShS-3000-1 as a power source created at the PWI. The performance of the furnace (furnace No. 1) are given below, and its scheme is in Figure 1.

Performance of the flux-melting furnace (furnace No. 1)

Rated power, kW	138
Operating voltage, V	45
Diameter of moving electrode, mm	150
Volume of water-cooled crucible, m^3:	
complete	0.07
operating	0.06

The furnace No. 2 was created on the base of the furnace No. 1 under the design of the LLC “ZTMK” on the base of the furnace EAF-0.5 with graphite lining of the furnace (Figure 2). An improved design of the melting furnace is intended for industrial melting and represents an electric arc single-phase furnace with graphite current-conducting bottom plate and a graphite lining. The performance of the electric arc furnace for industrial production of fluorphlogopite melt is the following:

Rated power, kW:	
minimum	160
maximum	3000
operating voltage, V	100
diameter of moving electrode, mm	150
Volume of graphite crucible, m^3:	
complete	0.2
operating	0.17

In producing fluorphlogopite melt, both physical processes (heating of charge, melting of its compo-

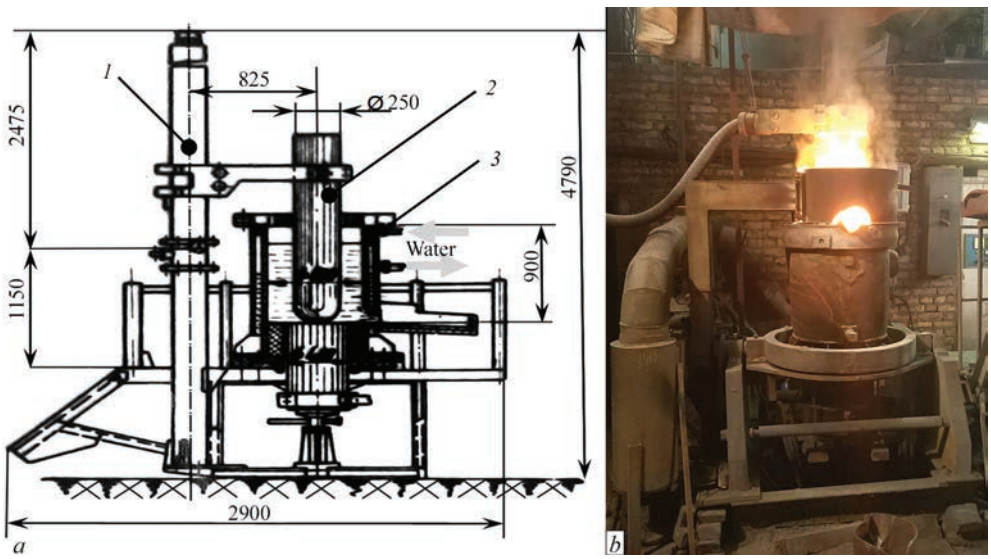

Figure 1. Scheme (*a*) and appearance (*b*) of flux-melting furnace No. 1: *1* — column; *2* — electrode; *3* — water-cooled crucible

nents, dissolution of periclase and other components in the formed liquid, evaporation of fluorides), as well as chemical reactions of decay of silicofluoride potassium, the interaction of different components and the formation of silicates. In the renewable conditions of melting (in the presence of graphite electrode and bottom plate),

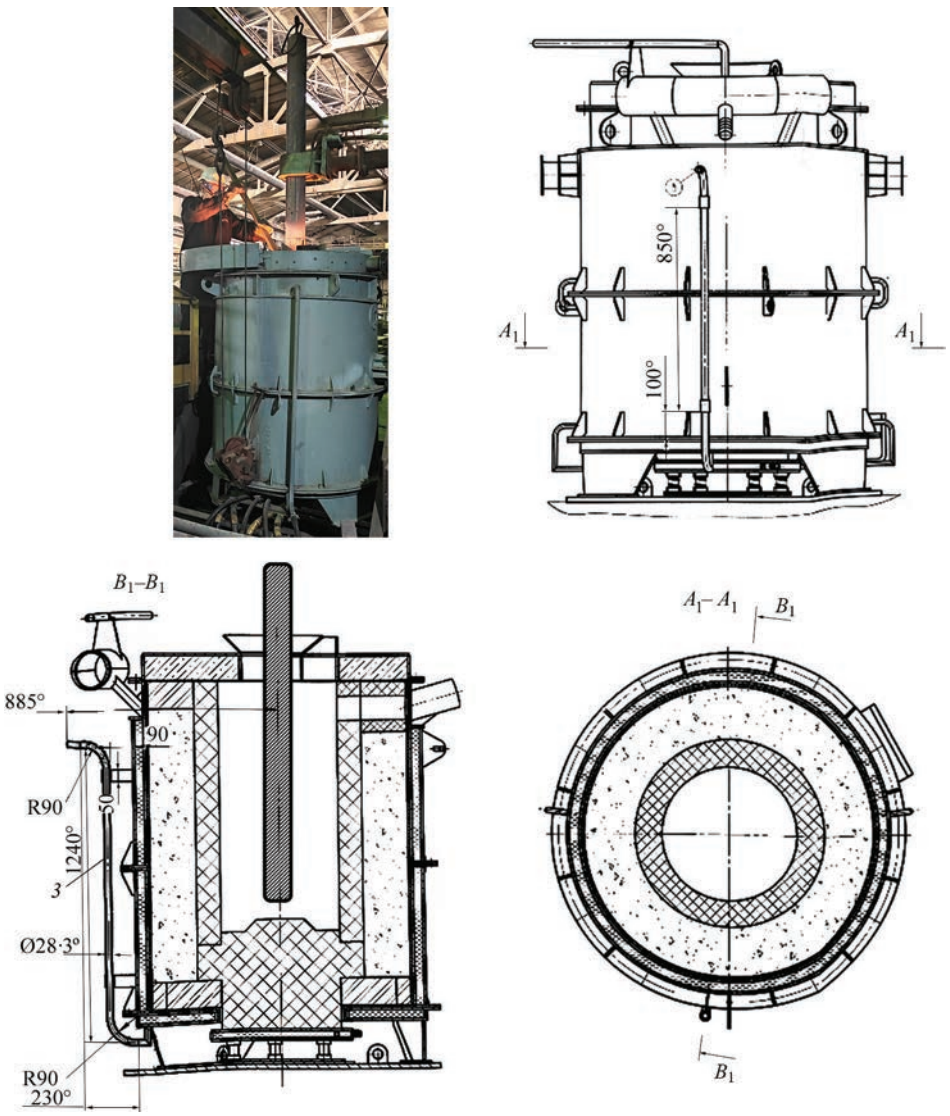

Figure 2. Appearance and scheme of electric arc furnace No. 2 for producing fluorphlogopite melt

a restoration of impurity substances (iron and manganese oxides) contained in charge materials occurs.

The process of producing fluorphlogopite melt was studied during a series of melts (mass of the melt was approximately 70 kg for each one). Analysis of the results of melts in the facilities of the PTIMA in a metal crucible showed that their temperature mode was not always satisfactory, as far as in the process of melting, a part of the melt was hardened, solidifiying on the bottom plate and on a side surface of the crucible. Being a dielectric, a solidified layer of fluorphlogopite material (whose thickness at different melts ranged from 10–15 to 100–120 mm) violated electric and, accordingly, thermal modes of the furnace. The instability of the melts (furnace No. 1) is also evidenced by a relatively wide range of their duration. During melts in the metal crucible, the current values were in the range from 800 to 1400 A, and their duration was from 180 to 400 min. The analysis of power consumption during initial melts shows that in their first half the electric mode of the furnace is unstable, the power changes within a wide range (from 106 to 170 kW). Loading a cold charge at this time leads to a sharp drop of current and, accordingly, power. Thus, loading of charge and scrap at a level of melt in the furnace from 100 to 150 mm lowers the power by 30–35 kW. In the second half of melting, when the mass fraction of the melt is more than a half of the pool (from 50 to 60 % of the total weight of the melting), the thermal mode is stabilized and the loading of charge and scrap does not disturb the electrical mode of melting.

In the process of producing fluorphlogopite melt in the furnace No. 2, the duration of initial melts ranged from 60 to 63 min and the further ones lasted from 26 to 32 min. The analysis of power consumption of the following melts showed that their power mode at the beginning is comparably more stable before the first melting. The power during melts changed from 110 to 215 kW, the next melts proceeded more intensively than the initial one.

The use of graphite lining leads to a change in the nature of the melting process and shortens its duration. The use of graphite lining fostered an increase in the current of the first melt from 1100 to 1900 A, and its duration was shortened to 120–150 min. The stabilization of the melting mode is indicated by the absence of a skull on a side surface of the crucible.

Stabilization and intensification of the process during melting in the furnace No. 2 can be explained by the fact that the use of graphite lining changes the electrical and thermal modes of the melting furnace. In a metal crucible, on water-cooled walls a non-conductive skull is formed from the melt, and the electric current mainly passes between the electrode and graphite bottom plate. In the furnace with graphite lining, no skull is formed on a side surface, and lining is heated both by heating the melt and by current. A relatively large, as compared to the area of the bottom plate, the current-conducting surface of the furnace walls and the absence of a skull on it leads to the fact that the main part of the current flows between the electrode and a side surface of the crucible [4]. This is also confirmed by the fact that an increase in the level of the melt during a constant immersion of the electrode leads to an increase in the current load, and this, in turn, provides the necessary temperature level of the melting process and contributes to its intensification.

Stabilizing and shortening the duration of melts made it possible to organize the melting process in a cyclic mode. At the same amount of produced melt, the duration of further melts ranged from 60 to 70 min. This is explained by the fact that in the initial period of further melts, the electric arc mode of operation is switched off due to the use of the initial amount of the melt of the previous melting, as well as the accumulation of heat by lining and furnace bottom plate. As a result, the consumption of electric power in the further melts is reduced and it is spent directly on the process of melting the charge, which in this case takes place at increased current loads (from 1600 to 2000 A).

However, the complexity of controlling the technological mode of melting in existing melting furnaces leads to repeated overheating and cooling of the melt in the process of its preparation (for example, when loading the next portion of the charge), as a result of which from the charge of the same composition, materials can be produced, differing by its structure and phase composition. The temperature of the melt, measured in the furnace before tapping during melting in a metal crucible ranged from 1350 to 1550 °C and with the use of graphite lining, it varied from 1550 to 1620 °C.

An increase in the temperature of the melting process leads, on the one hand, to a decrease in the duration of the melt preparation process, and on the other hand, to an increase in the number of impurity phases. When studying the process of producing fluorphlogopite melt, the influence of the temperature mode and duration of melting on the structure of the cast material was studied (Table). The optimal temperature range for the preparation of fluorphlogopite melt is 1400–1500 °C, the phase composition of the material is represented by fluorphlogopite (80–90 vol.%) and impurities: norbergite (5–10 vol.%) and glass phase (5–10 vol.%).

An increase in the melting temperature from 1500 to 1600 °C significantly reduces its duration (from 120 to 180 min), while the process of fluorphlogopite

Melt parameters and phase composition of synthesized materials, vol.%

Melt temperature, °C	Melting time, min	Fluorphlogopite	Norbergite	Enstatite	Spinel	α-cristabolite	Glass phase
1400–1450	360	80–90	5–10	–	–	–	5–10
	420	– »–	– »–	–	–	–	– »–
1450–1500	240	– »–	– »–	–	–	–	– »–
	300	– »–	– »–	3–5	–	–	– »–
1500–1600	120	75–85	– »–	5	–	–	– »–
	180	– »–	3–5	5–10	–	–	– »–
>1600	120	70–80	5	5	3–5	–	10–15
	150	60–75	–	5–10	5	5–10	– »–

formation is not significantly disturbed, although its amount slightly decreases (from 75 to 85 vol.%) and enstatite in the amount from 5 to 10 vol.% appears. A further increase in the melting temperature (above 1600 °C) slightly reduces its duration (to 150 min), but leads to a noticeable violation of the synthesis process: the amount of fluorphlogopite decreases (from 60 to 80 vol.%), the amount of glass phase (from 10 to 15 vol.%) and impurity minerals (15–25 vol.%) increases, among which alumomagnesian spinel and α-cristabolite are observed. This indicates a significant change in the chemical composition of the melt, predetermined by significant losses of fluorine — the most volatile component of fluorphlogopite melt. The losses of fluorine, as well as the formation of such impurity minerals as spinel and α-cristobalite lead to the formation of a very fine crystalline material, the macrostructure of which resembles porcelain and the size of fluorphlogopite crystals amounts to 0.3–0.5 mm.

In order to stably produce a melt with the required structure and phase composition, it is necessary to have an optimal fluorine content in the melt. Controlling the melting process by adjusting the fluorine content in the melt in a non-sealed electric arc melting furnace is problematic. At present there are no express methods to control the fluorine content in the melt [5]. The only method that allows making a quick conclusion about the content of fluorine in the melt during the melting process is the visual testing method, which is based on determining the structure of the material in the fracture of a technological sample (Figures 3, 4). The criteria for evaluating the sample are the following characteristics of the material fracture: color, luster, zoning, average size of fluorphlogopite crystals in the central zone of the sample. In the process of studies, it was determined that the characteristics of the structure of the castings and a technological sample are identical and do not differ from each other.

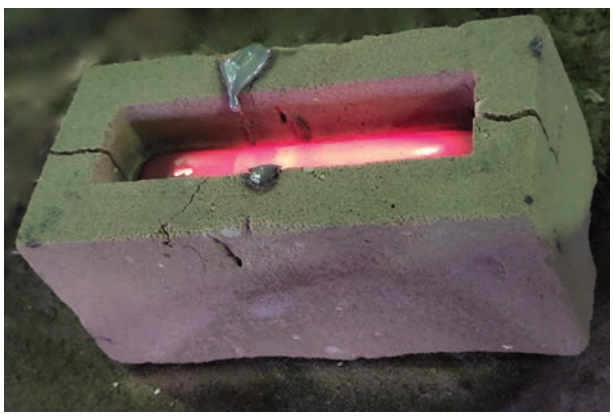

Figure 3. Appearance of a cast technological sample in a sand-clay cast mould

With an optimal ratio of the main components in the melt, the fracture of the sample material has the following characteristics: a uniform crystalline structure with the size of fluorphlogopite crystals of 0.5–3.0 mm, color — from light to dark gray, luster — glassy and on cleavage planes — silver (Figure 4).

Based on the studied features of preparing fluorphlogopite melt, the melting process can be conditionally divided into 2 periods: melting of the charge and formation of a set volume of melt; finishing and adjusting of the composition and temperature of the melt.

Thus, the study of the process of producing fluorphlogopite melt in electric arc furnaces showed that the intensity of meltings can be regulated by using graphite lining. The efficiency and economy of the melt preparation process increases when cyclic meltings are carried out, as well as with an increase in the power of the used transformer and capacity of the melting furnace, as far as the specific efficiency of the furnace increases.

During the first period of melting, 70–80 % of the required melt volume was deposited, then a technological sample was taken. According to the nature of the material fracture, the quality of the melt was determined and, if necessary, its composition was adjusted. The adjusting check was carried out on control samples, taken after penetration of the charge additive.

Thus, regulation of the composition of the melt during the melting period made it possible to transfer from the method of preparation based on the calculated composition of the charge to a controlled method with a periodic sampling of technological samples during the melting process and adjustment of the

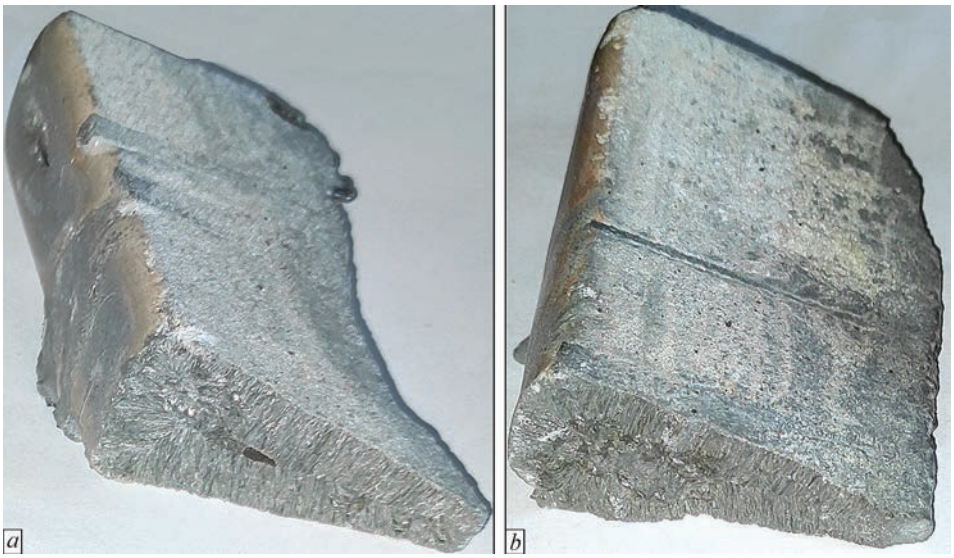

Figure 4. Appearance of the fracture of a technological sample before (*a*) and after (*b*) adjusting the composition of the fluorosilicate melt

Figure 5. Production of massive shaped fluorphlogopite castings: *a* — sand-clay mould; *b* — fluorphlogopite casting of "tap-hole stone" for chlorinator with a total weight of 150 kg

composition of the melt in order to produce a material with a stable structure and properties.

The use of an improved melting furnace and optimization of melting modes made it possible to manufacture massive (more than 150 kg) corrosion-resistant products for metallurgical furnaces of LLC "ZTMK" (Figure 5). At the same time, the cost of producing 1 ton of melt for such a casting was (based on cost, UAH: materials — 46800, electric power — 9072, salaries — 4914 for October 2021) 66686.00 UAH.

CONCLUSIONS

1. As a result of the conducted investigations, the process of producing fluorphlogopite melt in electric arc melting furnaces was studied, a method of express analysis of the quality of fluorphlogopite melt based on the fracture of technological samples, as well as a method of adjusting the composition of the melt with the charge and wastes of fluorphlogopite casting were created.

2. The process of melting fluorphlogopite melt requires a gradual dissolution of batches of mineral charge in the deposited melt of the furnace, which leads to an increased consumption of electric power as compared to melting of metal melts in arc furnaces. Due to the use of a new melting furnace with graphite lining, as well as optimization of melting modes, the cost of producing fluorphlogopite melt was UAH 66686.00 per ton. At the same time, it was possible to reduce the share of electricity in the cost from 28 to 13%, and in absolute terms it amounted to 2700 kW·h/t.

3. It is shown that the optimal temperature for producing fluorphlogopite melt ranges within 1400–1500 °C, while the equipment and the melting mode should prevent local overheating of the melt, which leads to the loss of volatile fluorine compounds. An increase in the temperature of the process leads to a decrease in the melting time, and on the other hand, to an increase in the amount of undesired impurity minerals and a glass phase. A significant loss of fluorine by the melt results in the formation of undesirable spinel and α-cristobalite phases, which lead to the formation of a porcelain-like macrostructure of the material, which negatively affects its mechanical and functional properties.

4. The developed technology of the method of operational control of the quality of fluorphlogopite casting according to fractures of a technological sample allows using up to 50–60 % of secondary fluorphlogopite material from casting wastes and used products, which increases the environmental friendliness of production and allows saving charge materials.

5. In general, the established features of producing fluorphlogopite melt together with rational melting modes and design of melting furnaces in combination with the proposed method of express-analysis of the macrostructure of cast stone casting allow depositing the necessary amount of melt for industrial casting of massive (more than 150 kg), corrosion-resistant products for metallurgical furnaces in the conditions of electric arc melting.

The work was carried out under the support of the following projects:

The National Key Research and Development Program of China — in the framework of the strategy "One Belt — One Road" (grant number 2020YFE0205300);

International Science and Technology Cooperation Project of Guangzhou Economic and Technological Development Zone(2019GH15);

GDAS' Project of Science and Technology Development （2021GDASYL-20210302006;

Project of the Guangzhou Economic and Technological Development Zone (2019GH19).

REFERENCES

1. Lejzerzon, M.S. (1962) *Synthetic mica*. Moscow, Gosenergoizdat [in Russian].
2. Belyakova, Yu.A., Golenko, V.P., Gorbunov, L.V. et al. (1987) *Synthesis of minerals.* Vol. 2. Moscow, Nedra [in Russian].
3. Paton, B.E., Zabarilo, O.S., Ubel, V.G. (1956) Application of water-cooled metal molds for flux melting in electric furnaces. *Avtomatich. Svarka*, **1**, 65–69 [in Russian].
4. Platonov, G.F. (1965) *Parameters and electric modes of metallurgical electrode furnaces*. Moscow, Energiya [in Russian].
5. Nikolaev, N.S., Suvorova, S.N., Gurovich, E.I. et al. (1970) *Analytical chemistry of fluorine*. Moscow, Nauka [in Russian].

ORCID

V.M. Korzhyk: 0000-0001-9106-8593,
V.O. Shcheretskyi: 0000-0002-8561-4444,
A.G. Maliavin: 0000-0003-0004-2393,
Yi Jianglong: 0000-0002-2018-7138,
A.O. Alyoshyn: 0000-0001-9696-6800,
A.A. Alyoshyn: 0000-0001-9222-1078

CONFLICT OF INTEREST

The Authors declare no conflict of interest

CORRESPONDING AUTHOR

V.M. Korzhyk
China-Ukraine Institute of Welding, Guangdong Academy of Sciences, Guangdong Provincial Key Laboratory of Advanced Welding Technology
Guangzhou, 510650, China.
E-mail: vnkorzhyk@gmail.com

SUGGESTED CITATION

V.M. Korzhyk, V.O. Shcheretskyi, A.G. Maliavin, Yi Jianglong, A.O. Alyoshyn, A.A. Alyoshyn (2022) Studying the process of producing fluorphlogopite melt in electric arc furnace for the production of massive corrosion-resistant products for nonferrous metallurgy. *The Paton Welding J.*, **12**, 40–46.

JOURNAL HOME PAGE

https://patonpublishinghouse.com/eng/journals/tpwj

Received: 28.02.2022
Accepted: 30.01.2023

DOI: https://doi.org/10.37434/tpwj2022.12.07

REDUCING THE LEVEL OF INTERFERENCES IN THERMAL NON-DESTRUCTIVE TESTING CONSIDERING THE SPECIFIC THERMOPHYSICAL AND MORPHOLOGICAL CHARACTERISTICS OF THE OBJECTS

V.O. Storozhenko, O.V. Miahkyi, R.P. Orel, S.M. Meshkov

RTC «Thermocontrol» of Kharkiv National University of Radio Electronics
14 Nauky Prosp., 61166, Kharkiv, Ukraine

ABSTRACT

Interferences, characteristic for non-destructive thermal testing which reduce the reliability of the obtained results are described. A technique for their reduction is suggested which consists of two interrelated stages. The first stage consists in calculating and analyzing the nature and level of the expected signal according to the developed thermophysical model against the background of the experimentally obtained interference level. According to the results of analysis of calculations using the thermophysical model for the selected samples, the most influential interference was the inhomogeneity of the emissivity of the sample surface. The second stage of processing the received data is devoted to reducing this interference. This stage consists in processing thermograms of temperature fields and includes morphological analysis of the surface condition, filtering and reducing characteristic interferences and interferences. It consists of four practical procedures: analysis of a visual image and obtaining a map of zones with a different emissivity of the sample surface, analysis of the thermogram with an assessment of the level of discreteness of the thermogram and the position of fiducial points on the image, smoothing the thermographic image and highlighting zones on the thermogram with different emissivity of the controlled object surface, after which the interference is filtered. Since the results of thermal testing are strongly influenced by the shape of an object, the possibilities and effectiveness of the suggested technique are illustrated on a cylindrical object. It has been experimentally confirmed that for the selected sample, it was possible to reduce the interference level to that of confident separation of a useful signal against the interference background.

KEYWORDS: thermal non-destructive testing, useful signal level, structural interference, thermophysical model, image processing, morphological analysis

INTRODUCTION

The active development of pipeline transport in the world began in the late 1960s, and now the length of main pipelines is hundreds of thousands of kilometers, including: gas pipelines, oil pipelines, water pipelines, heating and cooling systems. This gigantic infrastructure has been under load for tens of years, due to which it is prone to corrosion and wear. Monitoring the state of such systems by contact methods is a complex and expensive procedure. Therefore, for the mentioned objects, non-contact methods are more effective, which in most cases have no alternative. One of the promising methods of non-contact non-destructive testing is the thermal method (for objects that have their own thermal field). At present, there are a large number of algorithms for image quality enhancement, but they are ineffective for processing thermograms during non-destructive thermal testing. This is associated with the features of infrared radiation and the specifics of its registration. Therefore, it is not always possible to realize the potential of this method in practice due to the presence of significant interferences. The indicated drawback can be eliminated both at the stage of measurements as well as when processing the obtained results by taking into account the thermophysical characteristics and structural features of tested objects [1, 2].

INTERFERENCES IN THERMAL NON-DESTRUCTIVE TESTING

When realizing thermal testing (TT), the source of interferences and interferences is a testing object (TO), registration equipment, and the influence of the environment. Interferences can be added to the useful temperature signal T (additive interference $\tilde{A}$) or multiplied with it (multiplicative interference A) [1]:

$$u(x, y, \tau) = \tilde{M}T(x, y, \tau) + \tilde{A}. \quad (1)$$

From (1) it is seen that the signal $u \equiv T$ is registered only when $\tilde{M} \equiv 1$ and $\tilde{A} \equiv 0$. The best testing procedure is one in which the sensitivity of the method is limited by the radiation detector, i.e. $\tilde{M} \equiv 1$ and $\tilde{A} \rightarrow$ min. Interferences and interferences are also subject to this law, but the difference between them lies in the nature of their dependence: interference is a signal that has a random nature, and interference is a signal, whose magnitude is subject to the cause of its occurrence [3].

During active TT, the main source of external interference is the heater. During passive TT, external sources of thermal radiation can generate false signals

that operator can interpret as signs of a defect. This problem is complicated by the fact that the radiation reflected from a testing object depends on the state of its surface and the registration angle.

To reduce interferences and increase the efficiency of thermal testing, a method based on the analysis of defect detection (TT procedure) and improved procedures of processing the obtained images of TO temperature fields was used. In addition to the surface condition, the shape of TO also plays an important role in thermal testing.

The specified aim is achieved using a theoretical-experimental approach, which combines the construction and analysis of a thermophysical model and the procedure of a computer processing of the results of testing an object of a complex shape. As an experimental sample, a fragment of the pressure pipeline, provided by specialists of the South Ukraine NPP, was used.

SELECTION OF A THERMOPHYSICAL MODEL

The proposed technique consists of two interrelated stages. The first stage consists in the calculation and analysis of the nature and level of the expected signal according to the developed thermophysical model against the background of the experimentally obtained level of interferences. According to the results of the analysis of calculations based on the thermophysical model for the selected samples, the procedure of the further computer processing of the obtained data is selected [4, 5]. The second stage consists in the processing of thermograms of temperature fields and includes a morphological analysis of the state of the surface, filtering and reduction of characteristic interferences and interferences. The main condition for an adequate description of the testing process is the selection of both physical and mathematical models, which most fully reflect the features of heat transfer in a defect and a product, and also allow analyzing the model of a tested object, features of the process and calculating quantitative parameters with the required accuracy.

As a model of TO, a thermophysical model of a cylindrical shape with a local defect of a type of wall thinning, shown in Figure 1, was selected. The testing object is represented as a cylinder with inhomogeneity (defect). The defect in the form of the wall thinning is modeled by a groove inside TO with the depth h_d and the size l_d.

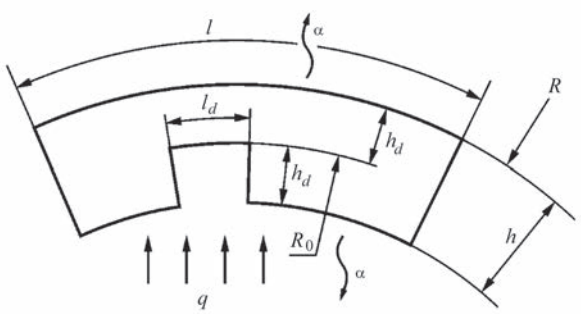

Figure 1. Testing object with a defect of the type of thinning of the pipeline wall

The following equation corresponds to the selected model:

$$\operatorname{div}(\lambda(T)\nabla T(\vec{r},t)) + Q(\vec{r},t) = c\rho\frac{\partial T(\vec{r},t)}{\partial t}, \qquad (2)$$

where $T(\vec{r} < t)$ is the temperature of the testing object, which depends on the coordinates of point M and time t; $\lambda(T)$ is the coefficient of thermal conductivity, W/(m·K) (in general case, it may depend on the temperature T); $Q(\vec{r}\ , t)$ is the function of inner heat sources, W/m^2; c is a specific heat capacity, J/(kg·K); ρ is the density of the substance, kg/m^3. If R_1 is the inner radius of TO; R is the outer radius of TO, then $\lambda(T)$ for $r < R_1$ equals to $\lambda_1(T)$, for $R_1 < r < R - \lambda_2(T)$, for $r > R - \lambda_3(T)$.

For a real process of thermal testing (thermal flaw detection), the equation (2) can be simplified taking into account the following factors: inner sources are absent and the coefficient of thermal conductivity does not depend on the temperature, because heating of TO does not exceed 100 °C. Taking this into account, we obtain [3]:

$$\left(\lambda(T)\frac{\partial^2 T}{\partial x^2} + \frac{\partial\lambda(\vec{r})}{\partial x}\frac{\partial T}{\partial x}\right) + \left(\lambda(T)\frac{\partial^2 T}{\partial y^2} + \frac{\partial\lambda(\vec{r})}{\partial y}\frac{\partial T}{\partial y}\right) + \left(\lambda(T)\frac{\partial^2 T}{\partial z^2} + \frac{\partial\lambda(\vec{r})}{\partial z}\frac{\partial T}{\partial z}\right) = c\rho\frac{\partial T(\vec{r},t)}{\partial t}. \qquad (3)$$

The equation (3) is a homogeneous linear differential equation of the second order of the parabolic type as far as $\lambda \geq 0$. Namely this equation adequately describes the selected thermophysical model (Figure 1) provided that it is solved under correctly selected boundary conditions corresponding to the real procedure of thermal testing, i.e. at the boundary conditions of the 2nd and 3rd kind on the outer surfaces of TO [6]:

$$\begin{cases} r = R_0 \\ \lambda(\vec{r},T)\dfrac{\partial T(\vec{r},t)}{\partial n}\Big|_S = \alpha\left(T(\vec{r},t)\Big|_S - T_{\text{inviron}}\right) - q(\vec{r},t); \end{cases} \qquad (4)$$

$$\begin{cases} r = R \\ -\lambda(\vec{r},T)\dfrac{\partial T(\vec{r},t)}{\partial n}\Big|_S = -\alpha\left(T(\vec{r},t)\Big|_S - T_{\text{inviron}}\right), \end{cases} \qquad (5)$$

where $q(\vec{r}\ , t)$ is the heat flow density, W/m^2; α is the heat transfer coefficient, W/(m^2·K); R_0 is the radius of the surface on which defect is located, m; h is the thickness of TO, m.

The ratios (4) and (5) reflect the real conditions of conducting an active TT, i.e. heating of TO by an external heating source and the presence of heat exchange with the environment. The mathematical model of the process is based on the solution of the differential equation of nonstationary thermal conductivity (2) recorded for the cylindrical coordinate system [7, 8].

The thermogram of the experimental sample with an interference caused by the inhomogeneity of the emissivity of the sample surface is shown in Figure 2. Based on the analysis of the results of calculations carried out according to the thermophysical model and data obtained from the thermograms of visual images of the testing object, the following results were obtained:

- the level of the expected signal is ~2–3 °C;
- the largest contribution to the level of interference is made by a multiplicative interference caused by the inhomogeneity of the emissivity of the sample;
- the level of a dominant interference is about ~4.3 °C.

The level of the useful signal and interference are close by an order of magnitude (according to Figure 2). Therefore, the thermogram needs further computer processing to reduce the dominant interference.

PROCESSING OF THERMAL TESTING RESULTS

The actual levels of interferences and interferences on experimental samples, for which thermophysical models were developed, are shown in Figure 3. As is seen, the level of the interference signal does not allow a reliable detection of defects. It is also clear that these interferences cannot be removed by the methods of graphical image processing, but additional information can be applied, obtained earlier during modeling.

The thermogram analysis (Figure 2) showed that the greatest contribution to the level of interferences is caused by the inhomogeneity of the emissivity and is associated with the state of the surface and the change in the registration angle of radiation, which is typical of cylindrical objects with a small radius.

The essence of the proposed method of processing thermogram of TO with a complex geometry consists in compensating for interferences in the areas of their presence. The proposed method makes it possible to highlight such zones by using the obtained a priori information from a visible image in the form of a map of zones with a different emissivity and comparing it with the thermogram.

To automate the process of comparing the map of zones with a different emissivity and the thermogram, an algorithm was proposed, which consists of the following procedures:

- visual image analysis (receiving a map of zones with different emissivity of the sample surface);

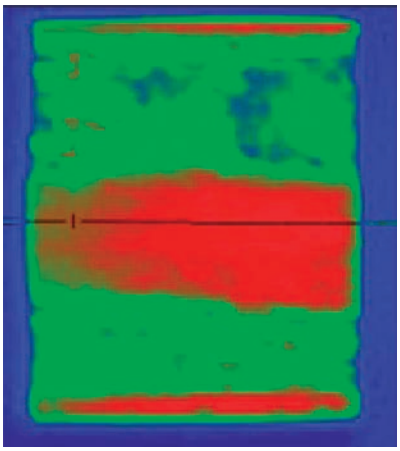

Figure 2. Thermogram of the pipeline fragment with a defect and probable interferences

- thermogram analysis (assessment of the level of discreteness of the thermogram and the position of fiducial points);
- preliminary image processing (smoothing of a thermographic image, because, as a rule, it is more discrete than visible);
- allocation of zones with different emissivity of TO surface on the thermogram (takes place during overlay of the map of zones on the thermogram by combining fiducial points).

In image processing and recognition of the zones of interest, a limited set of methods for preliminary image processing is used [9]. This is associated with the fact that modern systems for TO registration are designed for operator control, which allows maintaining the characteristics of obtained images in a narrow range, corresponding to the optimal testing mode [4].

Then, to highlight the zone of interest on the thermogram, a visible image is normalized using two fiducial points selected on the thermogram and on a visible image. The normalization is necessary to obtain a more accurate contour of the zone of interest on the thermogram. After the stage of image preparation, fiducial points are allocated on a visible image inside the contour of an object. This stage is also carried out on the thermogram. After that, the contour is transferred from a visible image to the thermogram. To do that, it is necessary to perform the following steps:

- preparation of a visible image, which includes filtering, allocation of contours, normalization (scaling and rotation) and segmentation (allocation of an object by fiducial points). The described stages at a correct selection of methods allow obtaining a contour in a visible image for its further overlay on the thermogram;
- carrying out analysis of the thermogram, which includes normalization and allocation of fiducial points and the zone of interest on the thermogram and a visible image. Highlighting the zone of inter-

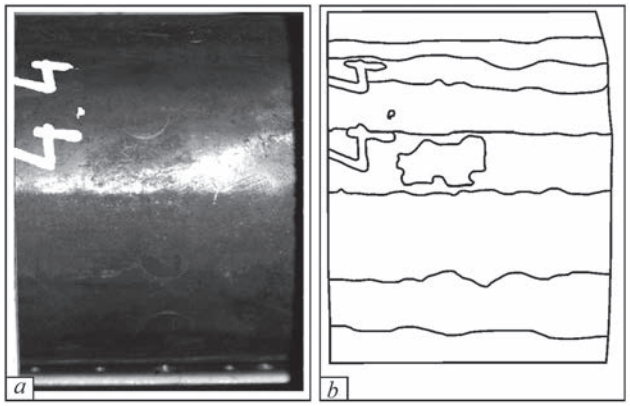

Figure 3. Visible image of the pipe fragment (*a*) and the result of processing image by the Roberts operator after filtering (*b*)

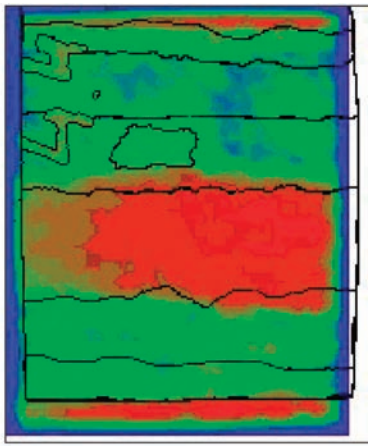

Figure 4. Overlay of a filtered visible image on a thermographic one

est consists of two stages: transfer of the contours of an allocated object obtained in a visible image to the thermogram and detection of zones with the average emissivity on the studied surface of the samples [10].

With a help of the obtained contour of the zone it is possible to analyze it by temperature values [1, 4].

There are many methods of a visible image filtering: convolution, combined filtering with a differentiated smoothing of areas with different information value, median method, linear and nonlinear filtering, SUSAN method [4], from which in the carried out experimental studies the methods of median filtering and SUSAN were used.

Due to such a procedure, texture interferences were suppressed, which simplified the further processing. Visual analysis did not reveal significant changes, but the need in such a filtering is a very important stage for the further processing.

The next stage in preparing a visible image is the contours allocation. In order to do that, on a visible image, the method of active contours, Roberts operator, Laplace operator and the difference method were selected. In the developed software product, the Roberts method and the difference method are presented. Before processing of an image by the mentioned methods, it is necessary to carry out a preliminary filtering by the SUSAN method, because for the correct operation of the Roberts operator, a continuous function of intensity is required, and the basic image has a discrete function [4]. The result of using the Roberts operator is shown in Figure 3.

Over the two-dimensional function, obtained as a result of processing, a smoothing filtering was carried out to reduce the discretization of zones and to obtain a continuous contour of the zone regardless of what method was used to allocate the contour. At this stage of the algorithm, the overlay function was realized. It allows combining a filtered image with the thermogram of an object. The result of this function is presented in Figure 4.

For each zone, the correction factor [1] was set, which compensated for the inhomogeneity of the emissivity and the registration angle in the specified area. Thus, interferences mentioned earlier were filtered and the initial temperature field was restored (Figure 5).

The obtained results show that the temperature field (Figure 5, *b*) increases from left to right, which corresponds to the reduction in the thickness of the sample wall (Figure 5, *c*). As is seen from the abovementioned thermograms, the level of a structural interference, caused by the inhomogeneity of the

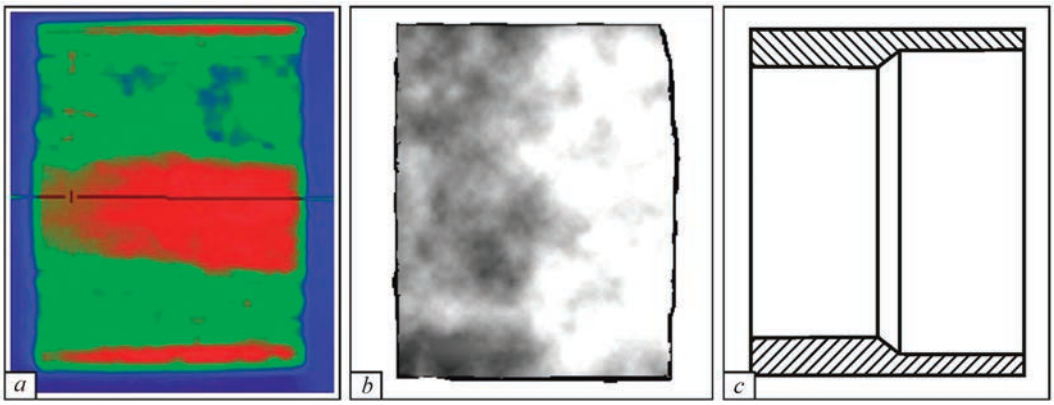

Figure 5. Results of the experiment: thermogram of the steam line fragment (*a*), restored temperature field of TO (*b*), cross-section of the sample (*c*)

emissivity of the surface and the angle of registration of the sample, decreased from 4.3 to 0.7 °C, i.e. by 3.6 °C. The level of non-dominant interferences and interferences amounts to 1.1 °C, which does not interfere with the separation of a useful signal on their background. Thus, the proposed technique allowed revealing the inner structure of the sample — an area with a different wall thickness and the boundary between them.

CONCLUSIONS

The method of processing the results of a thermal testing is proposed, which allows taking into account the features of infrared radiation and specifics of its registration. The method allows reducing the level of structural interferences, which is based on the analysis of a thermophysical model and morphological features of visible and temperature images.

The carried out theoretical and experimental studies showed the effectiveness of a new approach to the analysis of thermal images in a thermal non-destructive testing.

The thermophysical model of testing an object of a cylindrical shape was developed, which takes into account the peculiarities of heat transfer in a defect and on the basis of which it is possible to calculate and analyze the nature and level of the expected signal on the background of experimentally obtained level of interference.

Using the system of correction factors for different zones on the surface of a testing object allows getting closer to solving a complex problem for the thermal method — testing objects of a complex shape and objects that have regular structural heterogeneities.

The described algorithm allows processing image and compensating interference when it cannot be minimized by optimizing the active testing mode [8].

The carried out experiment confirmed the validity and correctness of the theoretical provisions and allowed determining the inner structure of a studied object (different wall thickness) and reducing the level of structural interferences by 3.6 °C (from 4.3 to 0.7 °C).

The studies show that processing of experimental data, carried out taking into account the peculiarities of thermophysical and structural characteristics of testing objects provides a significant positive result and is an important step to automation of procedures of a thermal non-destructive testing on its path of introduction into the mass production.

REFERENCES

1. Vavilov, V.P. (2009) *Infrared thermography and thermal control.* Moscow, Spektr [in Russian].
2. Storozhenko, V.A., Maslova, V.A. (2004) *Thermography in diagnostics and nondestructive testing*. Kharkov, Smit [in Russian].
3. Xavier, P.V. Maldague (2001) *Theory and practice of infrared technology for nondestructive testing*. John Wiley & Sons, Inc.
4. Pragnan Chakravorty (2018) What is a Signal? *IEEE Signal Processing Magazine*, 35(**5**), 175–177. DOI: https://doi.org/10.1109/MSP.2018.2832195
5. Storozhenko, V.A., Malik, S.B., Myagky, A.V. (2008) Optimization of modes of thermal flaw detection based on thermophysical modeling. *Visnyk NTU KhPI, Seriya: Elektroenergetyka ta Peretvoryuvalna Tekhnika*, **48**, 84–91 [in Russian].
6. Storozhenko, V.A., Myagky, A.V., Malik, S.B., Tikhy, V.G. (2013) Optimization of the procedure of thermal flaw detection of honeycomb structures. *Tekh. Diagnost. i Nerazrush. Kontrol*, **3**, 31–35 [in Russian].
7. Myagky, A.V., Lazorenko, O.V., Storozhenko, V.A. (2013) Processing the results of thermal flaw detection of honeycomb structures to reduce the level of interferences. *Visnyk NTU KhPI, Seriya: Elektroenergetyka ta Peretvoryuvalna Tekhnika*, **34**, 108–122 [in Russian].
8. Storozhenko, V., Myagkiy, A., Orel, R. (2016) Optimization of the procedure of thermal flaw detection of the honeycomb constructions by improving the accuracy of interference function. *Eastern-European J. of Enterprise Technologies*, **5**, 12–18. DOI: https://doi.org/10.15587/1729-4061.2016.79563
9. Basim Alhadidi, Mohammad H. Zu'bi, Hussam N. Suleiman (2007) Mammogram breast cancer image detection using image processing functions. *Information Technology J.,* 6(**2**), 217–221. DOI: https://doi.org/10.3923/itj.2007.217.221
10. Solomon, C.J., Breckon, T.P. (2010) *Fundamentals of digital image processing: A practical approach with examples in matlab*. Wiley-Blackwell.

ORCID

V.O. Storozhenko: 0000-0002-7609-2955;
O.V. Miahkyi: 0000-0002-0442-5570;
R.P. Orel: 0000-0002-3592-2393;
S.M. Meshkov: 0000-0003-3464-8318

CONFLICT OF INTEREST

The Authors declare no conflict of interest

CORRESPONDING AUTHOR

V.O. Storozhenko
RTC «Thermocontrol» of Kharkiv National University of Radio Electronics
14 Nauky Prosp., 61166, Kharkiv, Ukraine.
E-mail: volodymyr.storozhenko@nure.ua

SUGGESTED CITATION

V.O. Storozhenko, O.V. Miahkyi, R.P. Orel, S.M. Meshkov (2022) Reducing the level of interferences in thermal non-destructive testing considering the specific thermophysical and morphological characteristics of the objects. *The Paton Welding J.*, **12**, 47–51.

JOURNAL HOME PAGE

https://patonpublishinghouse.com/eng/journals/tpwj

Received: 29.08.2022
Accepted: 30.01.2023

SUBSCRIPTION–2023

«The Paton Welding Journal» is Published Monthly Since 2000 in English, ISSN 0957-798X, doi.org/10.37434/tpwj.

«The Paton Welding Journal» can be also subscribed worldwide from catalogues subscription agency EBSCO.

If You are interested in making subscription directly via Editorial Board, fill, please, the coupon and send application by Fax or E-mail.

12 issues per year, back issues available.

$384, subscriptions for the printed (hard copy) version, air postage and packaging included.

$312, subscriptions for the electronic version (sending issues of Journal in pdf format or providing access to IP addresses).

Institutions with current subscriptions on printed version can purchase online access to the electronic versions of any back issues that they have not subscribed to. Issues of the Journal (more than two years old) are available at a substantially reduced price.

Subscription Coupon **Address for Journal Delivery**			
Term of Subscription Since	**20**	**Till**	**20**
Name, Initials			
Affiliation			
Position			
Tel., Fax, E-mail			

The archives for 2009–2020 are free of charge on www://patonpublishinghouse.com/eng/journals/tpwj

ADVERTISING
in «The Paton Welding Journal»

External cover, fully-colored:
First page of cover
(200×200 mm) — $700
Second page of cover
(200×290 mm) — $550
Third page of cover
(200×290 mm) — $500
Fourth page of cover
(200×290 mm) — $600

Internal cover, fully-colored:
First/second/third/fourth page
(200×290 mm) — $400

Internal insert:
(200×290 mm) — $340
(400×290 mm) — $500

- Article in the form of advertising is 50 % of the cost of advertising area
- When the sum of advertising contracts exceeds $1001, a flexible system of discounts is envisaged
- Size of Journal after cutting is 200Í290 mm

Address
11 Kazymyr Malevych Str., 03150, Kyiv, Ukraine
Tel./Fax: (38044) 205 23 90
E-mail: journal@paton.kiev.ua
www://patonpublishinghouse.com/eng/journals/tpwj